ABSTRACT

Title of dissertation: Optimality, Synthesis and a Continuum Model for Collective Motion

Udit Halder, Doctor of Philosophy, 2019

Dissertation directed by: Professor P. S. Krishnaprasad
Dept. of Electrical & Computer Engineering

It is of importance to study biological collectives and apply the wisdom so accrued to modern day engineering problems. In this dissertation we attempt to gain insight into collective behavior where the main contribution is twofold. First, a 'bottom-up' approach is employed to study individual level control law synthesis and emergence thereby of collective behavior. Three different problems, involving single and multiple agents, are studied by both analytical and experimental means. These problems arise from either a practical viewpoint or from attempts at describing biologically plausible feedback mechanisms. One result obtained in this context for a double agent scenario is that under a particular constant bearing pursuit strategy, the problem exhibits certain features common with the Kepler two body problem. Laboratory demonstrations of the solutions to these problems are presented. It is to be noted that these types of individual level control problems can help understand and construct building blocks for group level behaviors.

The second approach is 'top-down' in nature. It treats a collective as a whole

and asks if its movement minimizes some kind of energy functional. A key goal of this work is to develop wave equations and their solutions for a natural class of optimal control problems with which one can analyze information transfer in flocks. Controllability arguments in infinite dimensional spaces give strong support to construct solutions for such optimal control problems. Since the optimal control problems are infinite dimensional in the state space and one cannot simply expect Pontryagin's Maximum Principle (PMP) to apply in such a setting, the work has required care and attention to functional analytic considerations. In this work, it is shown that under a certain assumption on finite co-dimensionality of a reachable set, PMP remains valid. This assumption is then shown to hold true for the case of a specific ensemble of agents, each with state space as the Heisenberg group H(3). Moreover, analysis of optimal controls demonstrates the existence of traveling wave solutions in that setting. Synchronization results are obtained in a high coupling limit where deviation from neighbors is too costly for every agent. The combination of approaches based on PMP and calculus of variations have been fruitful in developing a solid new understanding of wave phenomena in collectives. We provide partial results along these lines for the case of a continuum of planar agents (SE(2) case).

Finally, a different top-down and data-driven approach to analyze collective behavior is also put forward in this thesis. It is known that the total kinetic energy of a flock can be divided into several modes attributed to rigid-body translations, rotations, volume changes, etc. Flight recordings of multiple events of European

starling flocks yield time-signals of these different energy modes. This approach then seeks an explanation of kinetic energy mode distributions (viewed as flock-scale decisions) by appealing to techniques from evolutionary game theory and optimal control theory. We propose the notion of cognitive cost that calculates a suitably defined action functional and measures the cost to an event, resulting from temporal variations of energy mode distributions.

Optimality, Synthesis and a Continuum Model for Collective Motion

by

Udit Halder

Dissertation submitted to the Faculty of the Graduate School of the
University of Maryland, College Park in partial fulfillment
of the requirements for the degree of
Doctor of Philosophy
2019

Advisory Committee:
Professor P. S. Krishnaprasad, Chair/Advisor
Professor Steve Marcus
Professor Nuno Martins
Professor André Tits
Professor Nikhil Chopra, Dean's Representative

Dedicated to my parents

Acknowledgments

I would like to take this opportunity to thank my advisor Prof. P. S. Krishnaprasad for all the help and support he has generously provided over the past five years. He has given me the freedom to think deeply about challenging and fundamental problems. It is his constant encouragement and enthusiasm for science over countless hours of enlightening discussions that positively propelled the work presented in this thesis. His persistent emphasis on attention to detail in every aspect of research has helped me grow as a researcher. It has been an absolute pleasure having him as my thesis advisor. I would also like to thank Prof. Steve Marcus, Prof. Nuno Martins, Prof. André Tits and Prof. Nikhil Chopra for being in my dissertation committee and reviewing this document. The insightful comments from the members of the dissertation committee have helped improve the quality of this thesis. Collaboration with Dr. Uroš Kalabić at the Mitsubishi Electric Research Laboratory has been very helpful. I also collaborated with Dr. Eric Justh on a central problem of my thesis and I thank him for all his feedback and wise opinions.

Over the past five years, I have been fortunate to interact with my colleagues in the Intelligent Servosystems Laboratory. I thank Ms. Vidya Raju, Dr. Biswadip Dey, Dr. Yunlong Huang, Prof. Kevin Galloway, Mr. Brent Schlotfeldt, and Mr. Kenneth Miltenberger for all the stimulating discussions we have had. I enjoyed a lot while collaborating with Dr. Biswadip Dey, Mr. Brent Schlotfeldt, and Ms. Vidya Raju at several stages of my PhD. Special thanks to Vidya who has been

on a same boat as me from the start of my graduate study. I would also like to thank my friends outside the lab without whose company and support my life as a graduate student would have been incomplete. Biswadip, Vidya, Dipankar, Siddharth, Soham, Debdipta, Abhishek, Rajdeep, Ankit, Proloy, Soumyadip, Agniv, Jiaul, Kushal and others – thank you all for making this journey a memorable one.

Finally, I would like to thank my parents who have been a source of constant inspiration and encouragement. I may not have accomplished this without their support.

This research was supported by the Air Force Office of Scientific Research under AFOSR Grant FA9550-10-1-0250, an AFOSR FY2012 DURIP Grant No. FA2386-12-1-3002, the ARL/ARO MURI Program Grant No. W911NF-13-1-0390, through the University of California Davis (as prime), the ARL/ARO Grant No. W911NF-17-1-0156, through the Virginia Polytechnic Institute and State University (as prime), and by Northrop Grumman Corporation.

Table of Contents

List of Tables ..... **vii**

List of Figures ..... **viii**

List of Abbreviations and Notations ..... **ix**

1 Introduction **1**
- 1.1 Mathematical Background 5
  - 1.1.1 Self Steering Particle Model 5
- 1.2 Experimental Setup 7

I Synthesis of Collective Motion: Bottom-up Approaches **9**

2 Feedback Laws for Collective Motion **10**
- 2.1 Introduction 10
- 2.2 Steering for Beacon Pursuit under Limited Sensing 11
  - 2.2.1 Tracking a Moving Beacon 13
  - 2.2.2 Dynamics Restricted to the Invariant Manifold 15
  - 2.2.3 Special Case: $\alpha = \frac{\pi}{2}$ 17
  - 2.2.4 The Limited Field of View (FOV) Problem 23
  - 2.2.5 Implementation 26
  - 2.2.6 Associated Lagrangian 30
- 2.3 Biomimetic Algorithms for Coordinated Motion 33
  - 2.3.1 Mutual Motion Camouflage (MMC) 34
  - 2.3.2 Topological Velocity Alignment (TVA) 36
  - 2.3.3 Implementation Results 38

3 Optimal Steering of Agents on a Plane **45**
- 3.1 Introduction 45
- 3.2 Optimal Steering of a Unicycle 47
  - 3.2.1 Optimal Control Solution 49
  - 3.2.2 Characterizing the Types of Motion 51
  - 3.2.3 On Time-optimality 59
- 3.3 Optimal Control of a Collective of Agents 60
- 3.4 Concluding Remarks 64

II Analysis of Collective Motion: Top-down Approaches **65**

4 Continuum Flocking and Control **66**
4.1 Motivation 66
4.2 A Control System on a Loop Group 69
4.3 Controllability 71
4.4 Optimal Control Problems 76
4.4.1 Calculus of Variations Approach 76
4.4.2 Maximum Principle Approach 79
4.5 Special Case : $G = \mathrm{H}(3)$ 84
4.5.1 Controllability 85
4.5.2 Equations of Optimal Control 87
4.5.3 Behavior of Optimal Control 92
4.5.4 Strong Coupling Limit, $\chi \to \infty$ 98
4.5.5 Simulation Results 101
4.6 A Continuum of Agents on the Plane 105
4.6.1 Equations of Optimal Control 106
4.6.2 Strong Coupling Limit, $\chi \to \infty$ 110
4.6.3 Simulation Results 111
4.7 Discussion and Scope of Future Research 118

5 Cognitive Cost of Flocking: A Geometric and Hamiltonian Perspective **120**
5.1 Introduction 120
5.2 Flocking Data 122
5.3 Data Smoothing 123
5.3.1 A linear generative model 124
5.3.2 Data smoothing in the Euclidean setting 125
5.4 Energy Modes 127
5.5 Generative model on the 1-simplex and the data-smoothing problem 131
5.6 Data Fitting Results 136
5.7 Discussion 138

6 Conclusions and Directions for Future Research **148**

A An Optimal Control Problem in an Infinite Dimensional Setting **152**
A.1 Introduction 152
A.2 Maximum Principle 156

Bibliography **167**

List of Tables

5.1 Details of captured flocking events 123
5.2 Hamiltonian Signature 138

List of Figures

1.1 Mobile robot based experimental platform (Pioneer 3 DX) with two-wheel differential and caster. 7

2.1 Illustration of scalar shape variables 13
2.2 Phase portrait 18
2.3 Nullclines of (2.5) with $u = 1, \nu_1 = 0.5, \nu_2 = 1$. 20
2.4 Robot (Pioneer 3 DX) with Kinect mounted, and the orange cone used as the beacon. 27
2.5 Implementation results for the limited FOV problem 29
2.6 Implementation results for MMC control law 40
2.7 Implementation results for TVA control law 41

3.1 Intersection of Hamiltonian and Casimir surfaces 51
3.2 Sample trajectories for different values of c, η and s_1, s_2 53

4.1 Numerical solution of (4.61) for experiment 1 99
4.2 Evolution of x_3 for experiment 1 100
4.3 Numerical solution of (4.61) for experiment 2 101
4.4 Evolution of x_3 for experiment 2 102
4.5 Numerical solutions of (4.61) for experiment 3 103
4.6 Numerical solution of (4.99) and state evolution for experiment 1 112
4.7 State evolution for experiment 2 114
4.8 State evolution for experiment 3 115
4.9 Numerical solution of (4.99) and state evolution for experiment 4 116
4.10 Numerical solution of (4.99) and state evolution for experiment 5 117

5.1 Hamiltonian signatures 136
5.2 Optimal energy allocation for event 1 140
5.3 Optimal energy allocation for event 2 141
5.4 Optimal energy allocation for event 3 142
5.5 Optimal energy allocation for event 4 143
5.6 Optimal energy allocation for event 5 144
5.7 Optimal energy allocation for event 6 145
5.8 Optimal energy allocation for event 7 146
5.9 Optimal energy allocation for event 8 147

List of Abbreviations and Notations

ROS	Robot Operating System
CB	Constant Bearing pursuit
FOV	Field-of-View
MMC	Mutual Motion Camouflage
TVA	Topological Velocity Alignment
PMP	Pontryagin's Maximum Principle
$\mathbf{r}_i$	Position of agent i
$\{\mathbf{x}_i, \mathbf{y}_i\}$	(planar) Natural Frenet Frame for agent i
tr	Trace (of a matrix)
$\mathbb{1}_n$	$n \times n$ identity matrix
$\operatorname{am} z$	Amplitude z
$\operatorname{sn} z$	Elliptic sine z, Jacobian elliptic function
$\operatorname{cn} z$	Elliptic cosine z, Jacobian elliptic function
$\operatorname{dn} z$	Delta amplitude z, Jacobian elliptic function
$T_m\mathcal{M}$	Tangent space at m to manifold $\mathcal{M}$
G	A matrix Lie group
$\mathfrak{g}$	Lie algebra of G
S^1	Circle group
$\mathscr{G}$	Loop group $C^\infty(S^1; G)$
$\mathscr{L}$	Loop algebra $C^\infty(S^1; \mathfrak{g})$
H(3)	Heisenberg group
SE(2)	Special Euclidean group
$\mathfrak{h}(3)$	Lie algebra of H(3)
$\mathfrak{se}(2)$	Lie algebra of SE(2)
χ	Coupling constant

Chapter 1

Introduction

The last few decades have witnessed an increase in research efforts towards uncovering mechanisms behind collective motion [Nagy et al., 2010; Ballerini et al., 2008a; Cavagna et al., 2010; Inada and Kawachi, 2002] and pursuit behavior [Olberg et al., 2000; Mizutani et al., 2003; Ghose et al., 2006; Chiu et al., 2010] in nature. Ranging from fish schools to bird flocks, collective behavior is seen abundantly in nature. The concept of *safety in numbers* is used in accomplishing variety of goals, from foraging food to evading predators. Recent improvements in data collection and processing technology has enabled researchers to study these natural flocks in more detail than ever before [Ballerini et al., 2008a,b]. The driving question then becomes to answer how local interactions between individual agents in the collective give rise to group level cohesion and synchrony. Although several attempts have been made to understand these behaviors [Cucker and Smale, 2007; Mora and Bialek, 2011; Bialek et al., 2012; Young et al., 2013; Attanasi et al., 2014], the individual level mechanisms responsible for emergence

of collective behavior remain mostly elusive to researchers. It is therefore a significant goal of this thesis to pursue such questions.

This thesis is distinctively divided into two parts, where we take two different approaches to understand collective behavior. The first approach is called a 'bottom-up' approach, i.e. instead of studying the flock as a whole, we concentrate on dynamics of individual agents and analyze simple interaction laws among small number of agents. Studying these interactions are important since they can be used as a building block for group level motion. In a 1995 paper [Vicsek et al., 1995], a novel discrete time self-driven particle model was first introduced to address self-ordered motion in a system of particles. The concept of self-steering particles was developed in the following decades [Justh and Krishnaprasad, 2004, 2006; Reddy et al., 2006; Mischiati and Krishnaprasad, 2010, 2012; Galloway et al., 2013]. We undertake the self-steering particle model under gyroscopic control [Justh and Krishnaprasad, 2003, 2004] as the basic model for individuals in the flock. This model describes a trajectory of an individual as a curve, described by the natural Frenet frame equations [Bishop, 1975] in the Euclidean space; and the driving controls are given by speed and curvature of the curve. We show in Chapter 2, 3 that even in the single agent or double agent case, interesting motion patterns can be synthesized from carefully selecting these control inputs. The control inputs can be generated from an underlying optimal control problem or by applying some biologically plausible feedback strategies. Parallel to the quest of

mathemetical modeling, some groups in the robotics community have performed successful implementation of various control strategies [Thurrowgood et al., 2014; Vásárhelyi et al., 2014], and thereby demonstrated the power of a bio-inspired approach towards synthesizing collective motion. Our work is similar in spirit, and provides indoor demonstrations of problems raised in Chapter 2. Some of these problems were conceptualized from a practical perspective and carry engineering value.

The other approach to study collective behavior is what can be called as 'top-down' view. Instead of specifying agent level control laws, the idea is to infer those laws from solving a bigger problem that investigates the flock as a whole. Existing literature employs several methods such as optimal control [Justh and Krishnaprasad, 2015b,a], statistical physics [Mora and Bialek, 2011; Bialek et al., 2012] etc. It is the framework of optimal control [Justh and Krishnaprasad, 2015b] that we undertake and extend in this thesis. It has been observed from empirical data [Ballerini et al., 2008a] that interaction among starlings in the flock is local, i.e. each bird interact with six/seven neighbors during flight. Taking inspiration from this idea, the central concept of [Justh and Krishnaprasad, 2015b] is to set up an optimal control problem which penalizes controls of individual agents coupled with mismatch in control with its 'neighbors'. The neighbors are determined by a previously defined interaction graph. We then let the number of agents in the flock to go to infinity in order to propose a continuum model for

flocking. Various continuum models have been studied for collectives [Kudrolli et al., 2008; Topaz et al., 2006; Zhang et al., 2010]. These models study a set of partial differential equations that describe spatio-temporal evolution of the flock density. Our approach is different in the sense that the system dynamics can be seen as an ordinary differential equation in an appropriate infinite dimensional Lie group setting. The coupling between birds are introduced through the mismatch term in the cost functional. A natural question of controllability of such a system is addressed by using a generalized Chow-Rashevsky theorem for infinite dimensional systems. This enables us to formulate the underlying optimal control problem in an infinite dimensional setting in which the usual Pontryagin's maximum principle fails in general without further assumptions. In Chapter 4, we invoke a maximum principle catered for this specific setting. A specific example of continuum of nonholonomic integrators is also studied in detail. This can be viewed as a continuum version of single agent Heisenberg case [Justh and Krishnaprasad, 2016]. It has been found that optimal control solutions possess a traveling wave character, which might enable information transfer in the flock. In addition to the Heisenberg case, we provide optimal control equations in the case of a continuum flock of planar agents. Synchronization results and numerical simulations are presented for both the cases.

In Chapter 5, we present another 'top-down' approach to the flocking problem. This approach is data-driven in nature. Kinematic energy modes of European

starling flocks are represented on a simplex which is then subjected to description as trajectory of some evolutionary game dynamics. Solution of this data-fitting problem on the simplex results in control inputs that are interpreted as modulation of fitness associated with the energy modes. We note that in contrast to Chapter 4, where the control inputs were individual agent-level (or 'low-level') controls, the controls obtained by this data-driven approach are flock-level (or 'high-level') controls. The flock is conceptualized to apply these controls to optimally allocate its kinetic energy among different modes.

1.1 Mathematical Background

1.1.1 Self Steering Particle Model

We describe the particle model that is the underlying generative model in all our subsequent analysis throughout this thesis. The trajectory of a single agent can be described by a function $\mathbf{r} : [0, T] \to \mathbb{R}^3$, for some $T > 0$. We assume $r(t)$ to be a regular curve, i.e. $\dot{\mathbf{r}}(t) \neq 0, \forall t \in [0, T]$. Let s be the arc length parameter, i.e. $s(t) = \int_0^t \|\dot{\mathbf{r}}(\sigma)\| \, d\sigma$. Under the regularity assumption, $s(t)$ is monotonically increasing and invertible function of time. We can then reparametrize the curve $\mathbf{r}(t)$ by the arc length parameter s and the evolution equations can be expressed in terms of well known Fernet-Serret frames. However, this way of representation requires thrice differentiability of the curve and need the curvature of the curve to be strictly positive. To overcome these difficulties, we take an alternate approach

for framing the curve, known as the *Natural Frenet frame* [Bishop, 1975]. This approach requires only twice differentiability and is well defined even when the second derivative vanishes.

In 3D, to any point on the curve $\mathbf{r}(t)$, we attach an orthonormal moving frame $\{\mathbf{x}(t), \mathbf{y}(t), \mathbf{z}(t)\}$. The unit vector $\mathbf{x}(t)$ is tangent to the curve and points toward the heading of an individual. The unit vectors $\{\mathbf{y}(t), \mathbf{z}(t)\}$ are chosen in the plane normal to $\mathbf{x}(t)$. The evolution of these vectors are given by the frame equations,

$$\begin{aligned}
\dot{\mathbf{r}}(t) &= \nu(t)\mathbf{x}(t) \\
\dot{\mathbf{x}}(t) &= \nu(t)(u(t)\mathbf{y}(t) + v(t)\mathbf{z}(t)) \\
\dot{\mathbf{y}}(t) &= -\nu(t)u(t)\mathbf{x}(t) \\
\dot{\mathbf{r}}(t) &= -\nu(t)v(t)\mathbf{x}(t),
\end{aligned} \tag{1.1}$$

where $\nu(t)$ is the speed ($\|\dot{\mathbf{r}}(t)\|$) and $(u(t), v(t))$ are called *natural curvatures* of the trajectory [Justh and Krishnaprasad, 2005]. In a planar setting, we have the frame $\{\mathbf{x}(t), \mathbf{y}(t)\}$ and the evolution equations are written as,

$$\begin{aligned}
\dot{\mathbf{r}}(t) &= \nu(t)\mathbf{x}(t) \\
\dot{\mathbf{x}}(t) &= \nu(t)u(t)\mathbf{y}(t) \\
\dot{\mathbf{y}}(t) &= -\nu(t)u(t)\mathbf{x}(t).
\end{aligned} \tag{1.2}$$

We can therefore treat ν and u variables as control inputs to steer the individual on the plane, ν as the velocity input and u as the curvature control input.

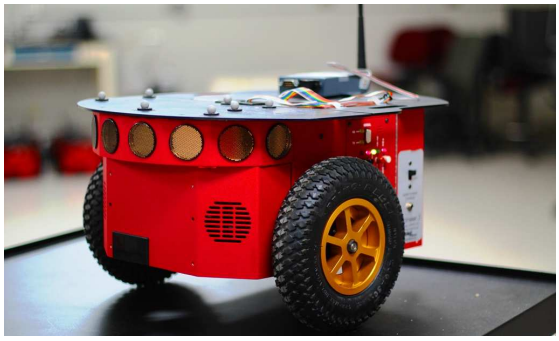

Figure 1.1: Mobile robot based experimental platform (Pioneer 3 DX) with two-wheel differential and caster.

1.2 Experimental Setup

We provide a comprehensive description of the laboratory set up in the Intelligent Servosystems Lab, University of Maryland. All the laboratory experiments presented in this thesis are done under this setup. Our experimental test-bed is comprised of Pioneer 3 DX wheeled robots from Adept MobileRobots [Pioneer]. These compact, differential-drive mobile robots are equipped with reversible DC motors, high-resolution motion encoders and 19cm wheels, and the onboard computation is done via a 32-bit Renesas SH2-7144 RISC microprocessor, including the P3-SH microcontroller with ARCOS. The sensors on the robot include eight forward-facing ultrasonic (sonar) sensors. ARIA [ROS-ARIA] provides an interface for controlling and receiving data from the robot, and communication with the robot for sending control commands (*forward velocity* and *turning rate*) is done via 802.11-b/g/n networking. The width of the robot is 380 mm and it has a swing radius of 260 mm.

Algorithm implementation (i.e, feedback law computation) has been done in C++ using ROS [ROS], along with ROS-ARIA [ROS-ARIA], as the interfacing robotics middleware. The experiments have been carried out in a laboratory environment equipped with a sub-millimeter accurate Vicon motion capture system [Vicon]. We use a Dell workstation to run ROS, and this computer is connected to the Vicon server via a dedicated Ethernet connection.

The Vicon system captures the motion of the robots and sends out the position and heading data to the computer running ROS. The control law program listens to this data, and transmits the individual *velocities* and *turning rates*. Both of these operations are carried out at a frequency of 25 Hz. The control law program computes the controls according to the strategy that is specific to the problem considered. The computed velocity and curvature control variables $\nu(t), u(t)$ can be translated to the *turning rate* $\omega(t)$ (in degrees/sec) as:

$$\omega(t) = \left(\frac{180}{\pi}\right) \nu(t)u(t). \tag{1.3}$$

Part I

Synthesis of Collective Motion:

Bottom-up Approaches

Chapter 2

Feedback Laws for Collective Motion

2.1 Introduction

Collective motion plays a crucial role in modern day robotics and engineering. It is becoming commonplace for a group of unmanned, remote controlled vehicles to be deployed to accomplish goals ranging from search and rescue to surveillance. For the swarm of robots to function in a harmonious manner, it is very important to control them carefully. Natural collectives are indeed an inspiration in this endeavor. On the other hand, a thorough study of those collectives remain incomplete without understanding agent level interaction laws. In this chapter therefore, we will build models for collective motion from 'bottom-up', i.e. from individual level control strategy to flock level synchrony through interaction among agents. This chapter presents a range of theoretical results as well as laboratory demonstrations of control laws that we propose or has been proposed before. This chapter has two main contributory sections, most of which

are taken verbatim from their respective publications. We start with a problem that studies a particular dyadic interaction under the setting of a pursuit strategy called constant bearing pursuit [Halder et al., 2016]. We gain interesting insight from this problem that connects to the Kepler two body problem. The obtained result of this problem is then used to solve a problem arising from a practical robot maneuvering scenario. The last problem is purely experimental [Halder and Dey, 2015] which demonstrate another dyadic interaction strategy potentially useful for surveillance, and a flocking strategy involving many agents.

2.2 Steering for Beacon Pursuit under Limited Sensing

In this section, we will try to understand simple dyadic pursuit strategies (i.e. strategies based on pairwise interactions), and exploit them as building blocks for synthesis of complex motion patterns for collectives. In [Galloway et al., 2009, 2013], using symmetry principles and nonlinear dynamics, a specific strategy, known as *constant bearing cyclic pursuit*, is shown to produce a rich variety of behaviors for appropriate choices of parameters (bearing angles). In [Justh and Krishnaprasad, 2006] a biologically plausible feedback control law is investigated that executes *motion camouflage*, a type of stealthy pursuit associated with visually-guided flight in insects (e.g. hoverflies and dragonflies). Stealth arises from nulling optic flow in the visual field of the target of pursuit, thereby

increasing the chance of success in prey capture or territorial battle against a conspecific. This type of dyadic interaction is also exploitable in coordinated motion, for instance see [Mischiati and Krishnaprasad, 2010].

The present work is similar to [Justh and Krishnaprasad, 2004] in motivation. We consider a problem of two agents moving in a plane with constant (not necessarily identical) speeds and, one of them is free i.e. it assumes any open loop steering (curvature) control, while the other pursues it. The free agent may be construed as a beacon and the pursuer's task is to reach a safe vicinity of the beacon and circulate around it. In the interesting case when the beacon is stationary, but the pursuer has a sensor with limited field of view (FOV) to detect the beacon, the circling law proposed in [Justh and Krishnaprasad, 2004] may be foiled. One goal of this work is to devise a principled approach (control algorithm) for this problem that copes with sensor limitation. We do this via a two-step process. We first analyze a slightly different problem of tracking a (slowly) moving beacon assuming that: (a) the beacon track is of constant curvature (i.e. on a straight line or on a circle); and (b) the sensor on-board the pursuer has no FOV limitation. For the choice of a constant bearing pursuit feedback control law, one obtains a rich dynamics. The phase portrait in turn suggests the second step – a feedback law modification that is applicable to the setting of stationary beacon, and limited FOV. In this case, one needs an additional ingredient – an estimator using odometry to track the beacon when it has fallen out of the FOV. The idea here is to use the odometry-based estimate in the feedback law as if it is exact

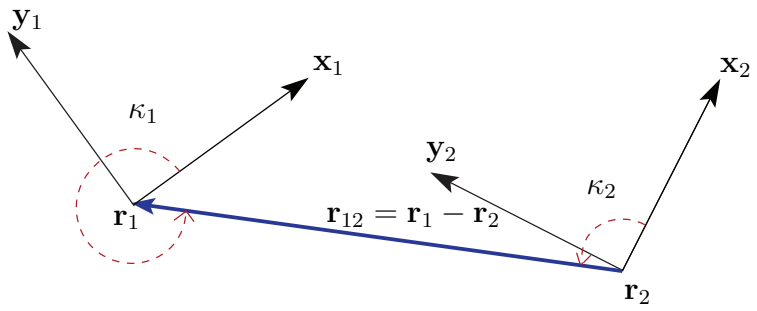

Figure 2.1: Illustration of scalar shape variables $(\rho, \kappa_1, \kappa_2)$ used to parametrize the shape space.

(a type of certainty equivalence) and use direct observation of the beacon when it is re-captured in the FOV. Such an estimator is used in an implementation of beacon tracking in a laboratory test-bed with a range camera (Kinect [Kinect]) as the sensor mounted on a mobile ground robot. A high precision (marker-based) motion capture system (Vicon [Vicon]) is used to determine ground truth and analyze the performance. In addition, the unconstrained tracking of the moving beacon problem is revisited and it is shown that the resulting dynamics can be identified with motion of a charged particle in an electromagnetic field. Moreover, at a particular value of the beacon curvature, the combined dynamics is exactly same as the Kepler problem of two bodies.

2.2.1 Tracking a Moving Beacon

Let us consider two agents moving on a plane, each abiding the self steering particle equations of motion. We assume that both their speeds ν_1, ν_2 are constants. It is possible to represent the dynamics of the system of two agents by the help

of scalar shape variables ρ, κ_1, κ_2 (Fig. 2.1) as

$$\begin{aligned}\dot{\rho} &= -\nu_1 \cos\kappa_1 - \nu_2 \cos\kappa_2 \\ \dot{\kappa}_1 &= -\nu_1 u_1 + \frac{1}{\rho}(\nu_1 \sin\kappa_1 + \nu_2 \sin\kappa_2) \\ \dot{\kappa}_2 &= -\nu_2 u_2 + \frac{1}{\rho}(\nu_1 \sin\kappa_1 + \nu_2 \sin\kappa_2).\end{aligned} \tag{2.1}$$

This is rather a straightforward calculation. We view agent 1 as a slowly moving beacon to which agent 2 pays attention. Let us make the following assumption.

A-1: The speed of agent 1 is less than the speed of agent 2, i.e. $\nu_1 < \nu_2$.

We pick the feedback control law for agent 2 as follows:

$$u_2 = -\tilde{\mu}\left(R(\alpha)\mathbf{y}_2 \cdot \frac{\mathbf{r}_{21}}{|\mathbf{r}_{21}|}\right) - \frac{1}{\nu_2|\mathbf{r}_{21}|}\left(\frac{\mathbf{r}_{21}}{|\mathbf{r}_{21}|} \cdot \dot{\mathbf{r}}_{21}^{\perp}\right), \tag{2.2}$$

for some $\tilde{\mu} > 0$. Here we denote $\mathbf{a}^{\perp} = R(\pi/2)\mathbf{a}$, for any vector $\mathbf{a}$ in the plane of motion, $R(\cdot)$ is the planar rotation matrix. Note that this control law is a standard constant bearing (CB) pursuit law [Galloway et al., 2013] with parameter α. The feedback control law can be expressed in terms of the scalar shape variables as

$$u_2 = \tilde{\mu}\sin(\kappa_2 - \alpha) + \frac{1}{\nu_2\rho}(\nu_1 \sin\kappa_1 + \nu_2 \sin\kappa_2)$$

The closed loop dynamics of (2.1) then takes the form

$$\begin{aligned}\dot{\rho} &= -\nu_1 \cos\kappa_1 - \nu_2 \cos\kappa_2 \\ \dot{\kappa}_1 &= -\nu_1 u_1 + \frac{1}{\rho}(\nu_1 \sin\kappa_1 + \nu_2 \sin\kappa_2) \\ \dot{\kappa}_2 &= -\tilde{\mu}\nu_2 \sin(\kappa_2 - \alpha).\end{aligned} \tag{2.3}$$

A fundamental result [Galloway et al., 2013] for the CB strategy tells us that under the action of the control law (2.2), the manifold

$$\mathcal{M}_{CB}^{\alpha} = \{(\rho, \kappa_1, \kappa_2) \in \mathbb{R}^+ \times S^1 \times S^1 \ : \ \kappa_2 = \alpha\}$$

is an attractive invariant manifold for all initial conditions except $\kappa_2(0) = \alpha + \pi$. The invariance follows directly from the closed loop dynamics (2.3). The attractiveness can be proved by defining $\Lambda(t) = -\cos(\kappa_2(t) - \alpha)$. Thus $\Lambda(0) \neq 1$ implies $\Lambda(t) \to -1$ as $t \to \infty$ or equivalently κ_2 converges to α.

2.2.2 Dynamics Restricted to the Invariant Manifold

At this stage, we are ready to make another assumption:

A-2: We consider the curvature of the beacon to be constant, i.e. $u_1 = u$, for some $u \in \mathbb{R}$ constant.

Now we focus our analysis on the dynamics on the invariant manifold (called $\mathcal{M}_{Shape} = \mathbb{R}^+ \times S^1$) which may be expressed as

$$\begin{aligned} \dot{\rho} &= -\nu_1 \cos\kappa_1 - \nu_2 \cos\alpha \\ \dot{\kappa}_1 &= -\nu_1 u + \frac{1}{\rho}(\nu_1 \sin\kappa_1 + \nu_2 \sin\alpha). \end{aligned} \tag{2.4}$$

It is of interest to characterize the solutions of the restricted dynamics (2.4) on the invariant manifold. Note that given ν_1, ν_2, u and α, (2.4) might have at most two equilibrium points (ρ^*, κ_1^*), with $\cos\kappa_1^* = -\frac{\cos\alpha}{\nu}$ and $\rho^* = \frac{\nu\sin\kappa_1^* + \sin\alpha}{\nu u}$, where we denote $\nu = \frac{\nu_1}{\nu_2} < 1$. Existence of such equilibrium points is guaranteed if $\nu \geq |\cos\alpha|$ and $(\nu\sin\kappa_1^* + \sin\alpha)u > 0$. Linearizing (2.4) around such an equilibrium point gives the Jacobian matrix

$$\nu_2 \begin{bmatrix} 0 & \nu\sin\kappa_1^* \\ -\frac{\nu u}{\rho^*} & -\frac{\cos\alpha}{\rho^*} \end{bmatrix},$$

with associated Eigenvalues

$$\lambda = \nu_2 \left(\frac{-\cos\alpha \pm \sqrt{\cos^2\alpha - 4\nu^2\rho^* u \sin\kappa_1^*}}{2\rho^*} \right).$$

Depending on α, following cases will arise

I. $\alpha \in (-\pi, -\pi/2) \cup (\pi/2, \pi]$

In this region, $\cos\alpha < 0$, which makes the equilibrium points unstable. So all trajectories tend to blow up in (ρ, κ_1) plane.

II. $\alpha \in (-\pi/2, \pi/2)$

Here, $\cos\alpha > 0$, then (locally) stable equilibrium exists if $u \sin\kappa_1^* > 0$, otherwise (ρ^*, κ_1^*) is unstable which leads to eventual collision. We note that [Davis, 1962] (pages 119-125) studies the same problem with $\alpha = 0$. For the $\alpha = 0$ case, the existence conditions of equilibrium read $\nu \geq 1$ and $u \sin\kappa_1^* > 0$, which in turn means we will have a stable equilibrium only when $\nu \geq 1$. The current problem can be viewed as a generalization of that considered in [Davis, 1962].

III. $\alpha \in \{\pi/2, -\pi/2\}$

In this case, however, the dynamics (2.4) produces a rich behavior which we analyze next. We only provide the analysis for $\alpha = \pi/2$ case, the other case being analogous.

2.2.3 Special Case: $\alpha = \frac{\pi}{2}$

We rewrite (2.4) in this particular case,

$$\begin{aligned} \dot{\rho} &= -\nu_1 \cos\kappa_1 \\ \dot{\kappa}_1 &= -\nu_1 u + \frac{1}{\rho}(\nu_2 + \nu_1 \sin\kappa_1). \end{aligned} \tag{2.5}$$

All the trajectories of (2.5) are closed and we will prove this in the same way as exploited in [Mischiati and Krishnaprasad, 2012]. We first introduce the following definitions and a theorem due to Birkhoff.

Definition 2.1 (**Involution**). A diffeomorphism $F : M \to M$ from a manifold M onto itself is said to be an *involution* if $F \neq id_M$, the identity diffeomorphism and $F^2 = id_M$, i.e. $F(F(m)) = m,\ \forall m \in M$.

Definition 2.2 (**F-reversibility**). A vector field X defined over a manifold M is said to be *F-reversible* if there exists an involution F such that $F_*(X) = -X$, i.e. F maps orbits of X to orbits of X, reversing the time parametrization. Here $(F_*(X))(m) = (DF)_{F^{-1}(m)}X(F^{-1}(m)),\ \forall m \in M$ is the push-forward of F. We call F the *reverser* of X.

Theorem 2.2.1 (**G.D. Birkhoff**, [Birkhoff, 1915]). *Let X be a F-reversible vector field on M and Σ_F the fixed-point set of the reverser F . If an orbit of X through a point of Σ_F intersects Σ_F at another point, then it is periodic.*

See [Mischiati and Krishnaprasad, 2012] for a detailed proof of this theorem. Based on these definitions and the theorem, we propose the following.

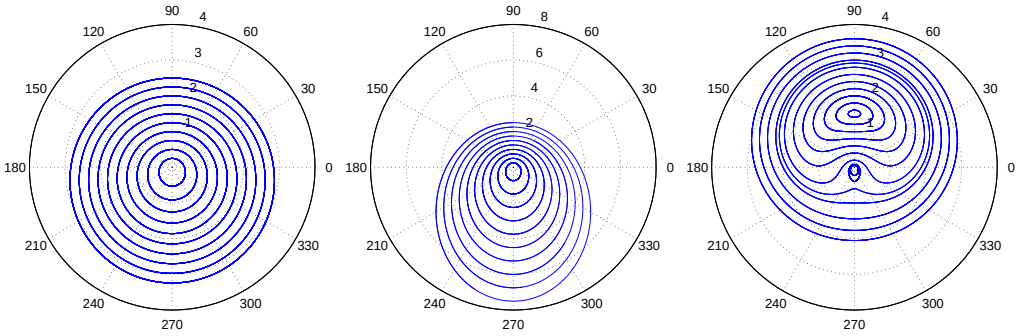

(a) $u = -2$ (b) $u = 0$ (c) $u = +2$

Figure 2.2: Phase portrait (polar plot) of the system dynamics restricted to the invariant manifold (2.5) with different values of u, keeping $\nu_1 = 0.5, \nu_2 = 1$ fixed for all three cases.

Theorem 2.2.2. *(i) The quantity,*

$$E(\rho, \kappa_1) = \rho(\nu_2 + \nu_1 \sin \kappa_1) - \frac{1}{2}\nu_1 u \rho^2 = E(\rho(0), \kappa_1(0)) \tag{2.6}$$

is conserved along any trajectory of (2.5).

(ii) Every solution of (2.5) *is periodic.*

Proof. (i) Denote, $\chi = \rho(\nu_2 + \nu_1 \sin \kappa_1)$, then

$$\begin{aligned} \frac{d\chi}{dt} &= \dot{\rho}(\nu_2 + \nu_1 \sin \kappa_1) + (\rho \nu_1 \cos \kappa_1)\dot{\kappa}_1 \\ &= \nu_1 u \rho \frac{d\rho}{dt} \\ \implies \chi(t) &= \frac{1}{2}\nu_1 u \rho^2(t) + c, \end{aligned}$$

where $c = \chi(0) - \nu_1 u \rho^2(0)/2 = \text{constant}$, which, in turn implies

$$E(\rho, \kappa_1) = \rho(\nu_2 + \nu_1 \sin \kappa_1) - \frac{1}{2}\nu_1 u \rho^2 = E(\rho(0), \kappa_1(0)).$$

(ii) *Step-1:* Vector field defined by (2.5) is F-reversible with reverser $F(\rho, \kappa_1) = (\rho, \pi - \kappa_1)$.

Clearly, F is an involution since $F^2(\rho, \kappa_1) = (\rho, \kappa_1)$. Next,

$$\begin{aligned}(F_*(X))(\rho, \kappa_1) &= (DF)_{F^{-1}(\rho,\kappa_1)} X(F^{-1}(\rho, \kappa_1)) \\ &= \begin{bmatrix} 1 & 0 \\ 0 & -1 \end{bmatrix} X(\rho, \pi - \kappa_1) \\ &= -X(\rho, \kappa_1).\end{aligned}$$

Hence, X is F-reversible.

Step-2: Fixed point set of F is given by $\Sigma_F = \{(\rho, \kappa_1) \ : \ \rho > 0, \kappa_1 = \pm\frac{\pi}{2}\}$. So every orbit of (2.5) crossing $\kappa_1 = \pm\frac{\pi}{2}$ line twice is periodic. Now, depending on the value of u, different cases will arise.

(a) $u \leq 0$: In this case, we note that the assumption $\nu_2 > \nu_1$ is sufficient to guarantee monotonicity of $\dot{\kappa}_1$, in particular $\dot{\kappa}_1 > 0$ for all time. Hence, any trajectory originating from any point on the $\kappa_1 = \pm\pi/2$ line (excluding the origin) will travel counter clockwise until it hits the line again when κ_1 gets incremented by an amount of π radian (see Fig. 2.2a, 2.2b). Note that the conserved energy, E prohibits any trajectory that starts with positive energy to go to the origin (with zero energy).

(b) $u > 0$: Because $\dot{\kappa}_1$ can assume any sign under this case, we need a more serious argument for this case. To determine the nullcline $\dot{\kappa}_1 = 0$, we compute

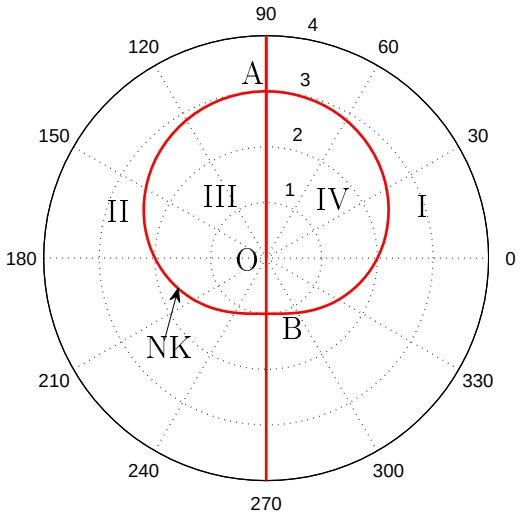

Figure 2.3: Nullclines of (2.5) with $u = 1, \nu_1 = 0.5, \nu_2 = 1$.

$\rho = \frac{\nu_2 + \nu_1 \sin\kappa_1}{\nu_1 u}$ and $\nu_2 > \nu_1$ ensures existence of a valid ρ for each value of κ_1. The $\dot{\rho}$ nullcline is simply the $\kappa_1 = \pm\pi/2$ line. This is illustrated in Fig. 2.3. It is immediate that in this case we have two equilibrium points, $\mathrm{A} = \left(\frac{\nu_2+\nu_1}{\nu_1 u}, +\frac{\pi}{2}\right)$ and $\mathrm{B} = \left(\frac{\nu_2-\nu_1}{\nu_1 u}, -\frac{\pi}{2}\right)$. The trajectories starting from either of those points are clearly periodic.

Depending on the nullclines, the whole space can be divided into four regions as shown in Fig. 2.3 and those regions are characterized as

$$\text{Region I} : \dot{\rho} < 0,\ \dot{\kappa}_1 < 0, \quad \text{Region III} : \dot{\rho} > 0,\ \dot{\kappa}_1 > 0,$$

$$\text{Region II} : \dot{\rho} > 0,\ \dot{\kappa}_1 < 0, \quad \text{Region IV} : \dot{\rho} < 0,\ \dot{\kappa}_1 > 0.$$

Now imagine trajectories starting on the line segment OA, excluding both points. Since $\dot{\kappa}_1 < 0$, they will move into region III, which can produce two outcomes:

(b1) It hits the OB line (excluding both points).

(b2) It exits region III through NK and goes into region II. Now the constancy of E gives the following observation, if a trajectory of (2.5) crosses NK at a certain angle $\kappa_1^{(1)}$, then it must cross it again at a different angle $\kappa_1^{(2)}$ and these angles are symmetric about $\kappa_1 = \pi/2$. This means trajectories must not enter region III from region II. This leads all the trajectories in region II to hit the $\kappa_1 = +\pi/2$ line beyond point A.

Next, consider trajectories starting at the boundary of region I and II with $\kappa_1 = \pi/2$. $\dot{\kappa}_1 < 0$ gives rise to clockwise motion into region I. Again, we need to analyze two scenarios:

(b3) The trajectories reach boundary between region I and II with $\kappa_1 = -\pi/2$.

(b4) They enter region IV through NK. Similar argument as in case (b2) can be employed to prove they must reach boundary between region III and IV with $\kappa_1 = \pi/2$.

Now, trajectories starting on OB line (excluding both points) must move in region IV and hence must hit OA line (excluding both points).

Finally, trajectories starting on the boundary between region I and II with $\kappa_1 = -\pi/2$ must go into region II and must eventually hit the boundary between region I and II with $\kappa_1 = \pi/2$ following a clockwise path (and without entering region III).

This completes the proof. ■

Remark 2.1. In a special case $u = 0$, (2.6) reads exactly as the polar equation of an ellipse $\frac{1}{\rho} = \tilde{c}(1 + \nu\cos\theta)$, where the origin is placed at one focus of the ellipse,

the angle θ is measured from the origin with respect to the major axis of the ellipse and $\nu = \frac{\nu_1}{\nu_2}$ is the eccentricity of the ellipse (recall A-1). It is of interest to note that the same elliptic equation comes from the analysis of the Kepler two-body problem [Goldstein et al., 2001].

A result of the dynamics (2.5) regarding time period is immediate in the light of Proposition 2.2.2.

Corollary 2.2.1. *Every orbit of (2.4) has a period*

$$T = 2\int_{\rho_{min}}^{\rho_{max}} \frac{d\rho}{\sqrt{\nu_1^2 - (\frac{1}{2}\nu_1 u\rho + \frac{E_0}{\rho} - \nu_2)^2}}, \tag{2.7}$$

where ρ_{min} and ρ_{max} are solutions of the pair of equations

$$\rho(\nu_2 \pm \nu_1) - \frac{1}{2}\nu_1 u\rho^2 = E(\rho(0), \kappa_1(0)) =: E_0 \tag{2.8}$$

In particular, for the case $u = 0$, the time period becomes, $T = \frac{2\pi\nu_2 E_0}{(\nu_2^2 - \nu_1^2)^{\frac{3}{2}}}$.

Remark 2.2. Note that for an "admissible" value of E_0, the pair of equations (2.8) has only two solutions. For the special case, $u = 0$, we know the closed loop trajectories are described by the ellipses $\rho = E_0/(\nu_2 + \nu_1 \sin\kappa_1)$ with semi-major axis, $a = \frac{1}{2}(\rho_{min} + \rho_{max}) = \frac{E_0}{2}\left(\frac{1}{\nu_2+\nu_1} + \frac{1}{\nu_2-\nu_1}\right) = \frac{E_0\nu_2}{\nu_2^2-\nu_1^2}$. Then, from Corollary 2.2.1, we find $T^2 = \left(\frac{4\pi^2}{\nu_2 E_0}\right) a^3$.

Remark 2.3. The condition $\nu_2 > \nu_1$ is necessary for the existence of periodic orbits for the case $u = 0$ while it is merely a sufficient condition for other values of u.

2.2.4 The Limited Field of View (FOV) Problem

In this section, we will describe the problem of tracking a stationary beacon by a controlled agent equipped with a sensor (e.g. a depth camera like Kinect) with limited field of view. As opposed to the problem discussed in the previous section, this problem is inspired by an implementation point of view. The backbone model (2.1) of the system stays the same. Agent 2 is supposed to sense the position of the beacon relative to its own position and use the sensed quantities to determine the control action. Using the shape variables, it has access to the pair (ρ, κ_2) (refer to Fig. 2.1), with the limitation that $|\kappa_2| \leq \kappa_{\max} < \pi/2$, which we call the field of view constraint. Although various feedback control laws have been proposed (for e.g. [Justh and Krishnaprasad, 2004]) to encircle a stationary beacon, permanent loss of the target (beacon) from the field of view cannot be avoided by those laws. More precisely, the limited FOV problem boils down to encircling the beacon while being able to sense it (at least) periodically.

Putting beacon speed, $\nu_1 = 0$ in (2.1) and ignoring κ_1 dynamics, the equivalent shape space equations can be reduced to

$$\begin{aligned} \dot{\rho} &= -\nu_2 \cos \kappa_2 \\ \dot{\kappa}_2 &= -\nu_2 u_2 + \frac{1}{\rho} \nu_2 \sin \kappa_2. \end{aligned} \tag{2.9}$$

Remark 2.4. From (2.9), it is guaranteed that under the field of view constraint, the attempt of encircling the beacon would eventually make the beacon permanently invisible (as long as a circular orbit around the beacon is considered). Moreover, from ρ dynamics, meeting the constraint $|\kappa_2| \leq \kappa_{\max} < \pi/2$ for all time

will lead to definite collision.

Once the beacon goes out of the FOV, the only choice for the vehicle would be to efficiently estimate the position of the beacon and apply the control based on those estimates. Accepting the fact mentioned in remark 2.4, one can only try to design the control u_2 in such a way that the control law provides some promise to bring the beacon back in the field of view after losing it. The following proposition is meant to serve that purpose.

Proposition 2.2.1. *The feedback control law given by*

$$u_2^{FOV} = u_0 - \frac{\mu}{\rho\nu_2}, \quad u_0 \leq 0,\ \mu > \nu_2, \tag{2.10}$$

guarantees the periodic return of the beacon to the field of view under ideal estimates.

Proof. With the feedback control (2.10), the closed loop system becomes,

$$\begin{aligned} \dot{\rho} &= -\nu_2 \cos\kappa_2 \\ \dot{\kappa}_2 &= -\nu_2 u_0 + \frac{1}{\rho}(\mu + \nu_2 \sin\kappa_2). \end{aligned} \tag{2.11}$$

Noticing that (2.11) is equivalent to (2.5), the claim follows directly from Theorem 2.2.2. From the polar phase portrait (Fig. 2.2), we see that the condition $u_0 \leq 0$ is required for the angle variable κ_2 to go through a full 360° rotation which is essential in order to bring the beacon back in the FOV. ■

As we will discover next, the condition on the parameter u_0 can be relaxed to include positive values as well. From Theorem 2.2.2, the condition $\mu > \nu_2$ is

only sufficient for any value of u_0. It becomes necessary for the particular case of $u_0 = 0$.

Although the feedback control law (2.10) produces all periodic orbits and it inherently takes care of collision avoidance problem (see Fig. 2.2), it lacks in the freedom of driving the vehicle to a particular desired orbit (*cf.* the circular orbits with desired radius as in [Justh and Krishnaprasad, 2004]). Moreover, the periodic orbits are not orbitally asymptotically stable which makes them susceptible to disturbances. To overcome these shortcomings, we propose the following.

Proposition 2.2.2. *Let E_d denote the admissible value of the desired energy, i.e. there exists a periodic orbit with $E(\rho, \kappa_2) = E_d$. Here $E(\rho, \kappa_2)$ is as in (2.6) with the pair (ν_1, ν_2) interpreted as (ν_2, μ) in present context. Then the control law*

$$u_2 = u_2^{FOV} + u_2^{AD} = u_0 - \frac{\mu}{\rho\nu_2} + k_d(E(\rho, \kappa_2) - E_d)\cos\kappa_2, \tag{2.12}$$

with $k_d > 0$ makes the orbit with energy E_d asymptotically stable with region of attraction given by $\mathcal{M}_{Shape} \setminus \{(\rho, \kappa_2) : \cos\kappa_2 = 0, \rho = \frac{(\mu+\nu_2\sin\kappa_2)}{\nu_2 u_0}, u_0 > 0\}$, where $\mathcal{M}_{Shape} = \mathbb{R}^+ \times S^1$.

Proof. Note that the trajectories of (2.9) with control (2.12) will no longer be periodic because of the inclusion of the extra u_2^{AD} term. Since $E(\rho, \kappa_2)$ is a continuous function of both ρ and κ_2, it suffices to prove that the quantity $(E(\rho, \kappa_2) - E_d)^2$ is monotonically decreasing. We obtain,

$$\frac{d}{dt}(E(\rho, \kappa_2) - E_d)^2 = -2k_d\rho\nu_2^2(E(\rho, \kappa_2) - E_d)^2\cos^2\kappa_2.$$

Clearly, with $k_d > 0$, $d(E(\rho, \kappa_2) - E_d)^2/dt \leq 0$, for all (ρ, κ_2) such that $\rho > 0$. The largest invariant subset of $\{(\rho, \kappa_2) : d(E(\rho, \kappa_2) - E_d)^2/dt = 0\}$ is indeed $\{(\rho, \kappa_2) : E(\rho, \kappa_2) = E_d\}$, which, in turn establishes the statement of the proposition. ■

In the light of Theorem 2.2.2, we see that the restriction $u_0 \leq 0$ in Proposition 2.2.1 can be relaxed. In particular, for $u_0 > 0$, one only has to choose E_d such that k_2 completes full 360° rotation (for e.g. one might pick $E_d = E(\rho, -\pi/2)$, with $\rho > \frac{\mu - \nu_2}{\nu_2 u_0}$, see Fig. 2.2(c)).

2.2.5 Implementation

In this laboratory implementation, we chose to use the newest Kinect model, which was created for Microsoft's Xbox One. The Kinect primarily functions as a motion-sensing input device, enabling players to interact with video games in exciting ways. To accomplish this, the device is equipped with several sensors including an RGB sensor, 3D Depth Sensor, as well as Multi-array Microphones. The Kinect's RGB sensor has a 70.6 degree horizontal field of view, and a 60 degree vertical field of view (see Fig. 2.4). The Kinect operates at a rate of 30 Hz, and has an effective range between 0.5 meters, and 4.5 meters where accuracy is reliable. Despite it's original use case as a video game controller, the Kinect has been studied recently as a sensor for many robotics applications, including autonomous vehicles [Oliver et al., 2012] and healthcare [Nghiem et al., 2012].

In this experiment, the Kinect RGB camera acts as a primary sensor for determining the distance and relative heading of the beacon (i.e. ρ, κ_2), which in

Figure 2.4: Robot (Pioneer 3 DX) with Kinect mounted, and the orange cone used as the beacon.

our experiment was an orange cone. OpenCV [OpenCV] is used to perform a simple blob detection algorithm that calculates the centroid of the cone in pixel coordinates, and then uses the Kinect's coordinate mapping feature to transform the result into physical, or camera space. To take advantage of these API features, we mount a laptop running the Windows operating system onto the robot, and utilize a custom TCP/IP server to stream the coordinates back to the robot control station. The control station is a Dell computer running ROS [ROS], and the algorithm implementation is done using the MATLAB ROS toolbox [MATLAB]. Finally, the Vicon motion capture system [Vicon] is used to track the motion of the robot and beacon in the lab coordinate space to obtain ground truth results of the implementation.

2.2.5.1 Estimation

In order to successfully implement the proposed control law, the robot has to be able to efficiently determine the beacon position relative to its own position during

the periods of time when the beacon is not in FOV. Equivalently, the estimation problem then is to integrate the closed loop shape dynamics ((2.9) with control (2.12)) given some initial condition, which in this case would be the last known (ρ, κ_2) value before the robot loses sight of the beacon. Since there is a conserved quantity associated with (2.11) (Proposition 2.2.2), a mid-point based update rule performs better than the naive Euler rule [Austin et al., 1993]. Denoting the estimate of (ρ, κ_2) by $(\hat{\rho}, \hat{\kappa}_2)$ and the discrete time step by Δt, the update rule may be implicitly expressed as follows:

$$\begin{aligned} \frac{\hat{\rho}^{n+1} - \hat{\rho}^n}{\Delta t} &= -\nu_2 \cos\left(\frac{\hat{\kappa}_2^n + \hat{\kappa}_2^{n+1}}{2}\right) \\ \frac{\hat{\kappa}_2^{n+1} - \hat{\kappa}_2^n}{\Delta t} &= -\nu_2 u_2^n + \frac{2\nu_2}{\hat{\rho}^{n+1} + \hat{\rho}^n} \sin\left(\frac{\hat{\kappa}_2^n + \hat{\kappa}_2^{n+1}}{2}\right), \end{aligned} \tag{2.13}$$

where $u_2^n = u_2(\hat{\rho}^n, \hat{\kappa}_2^n)$ as in (2.12) and $(\hat{\rho}^0, \hat{\kappa}_2^0)$ is the last successful measurement of the beacon position. We then solve the nonlinear equations (2.13) numerically (using MATLAB's *fsolve*) to produce the necessary estimates whenever the beacon is not in the field of view of the sensor. This procedure can be summarized in Algorithm 1.

2.2.5.2 Experimental Results

To demonstrate our solution to the limited field of view problem, we constructed an experiment for which the robot sees the orange cone and attempts to encircle it using the described control mechanisms. The result is a trajectory that periodically brings the cone back in its FOV so that the robot can fulfill its net

Algorithm 1: Steering Law Computation for Limited FOV Problem

Data: ρ : measured distance to beacon, κ_2 : measured angle to beacon;

$\hat{\rho}$: estimate of ρ, $\hat{\kappa}_2$: estimate of κ_2

Parameters: u_0, μ, k_d, E_d

begin

- **while** *not stopped* **do**
  - **if** *beacon visible* **then**
    - Compute $u_2 = u_2(\rho, \kappa_2)$ using equation (2.12)
  - **else**
    - Initialize: $(\hat{\rho}^0, \hat{\kappa}_2^0) \longleftarrow (\rho^{last}, \kappa_2^{last})$
    - Calculate $(\hat{\rho}, \hat{\kappa}_2)$ from (2.13)
    - Determine $u_2 = u_2(\hat{\rho}, \hat{\kappa}_2)$ using (2.12)

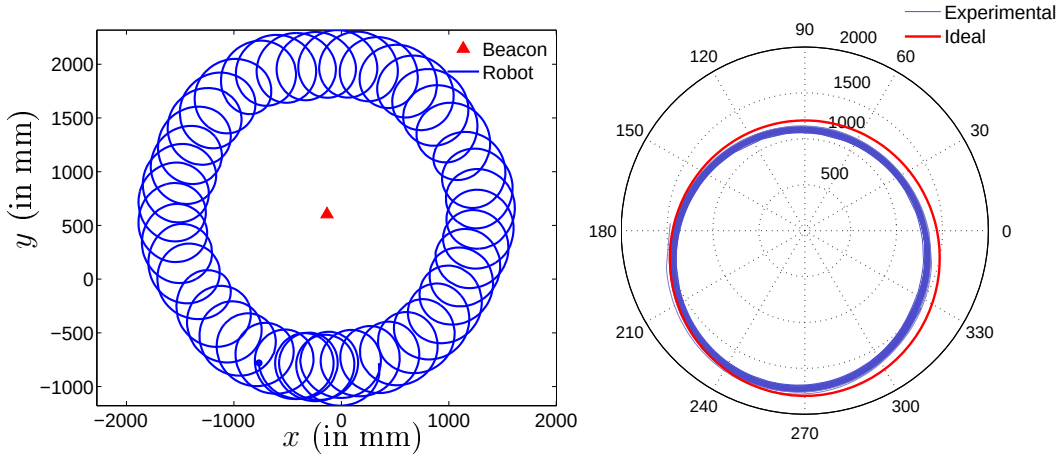

(a) Robot Trajectory

(b) Phase Portrait

Figure 2.5: Implementation results as recorded by Vicon (with $\nu_2 = 200$ mm/sec, $u_0 = 0$ mm^{-1}, $\mu = 1000$ mm/sec, $k_d = 5 \times 10^{-9}$ mm^{-3}sec and $E_d = 1.44 \times 10^6$ mm^2/sec).

encircling of the beacon. The ground truth data was obtained using Vicon. We ran the experiment using a robot speed $\nu_2 = 200$ mm/sec, and the parameters were $u_0 = 0$ mm^{-1}, $\mu = 5\nu_2 = 1000$ mm/sec, $k_d = 5 \times 10^{-9}$ mm^{-3} sec and E_d was taken to be energy corresponding to the orbit which maintains the minimum distance of 1200 mm from the beacon, in other words $E_d = 1.44 \times 10^6$ mm^2/sec.

Implementation results are shown in Fig. 2.5. The ground truth polar plot can be seen in comparison to the desired ellipse (since u_0 was taken to be 0) in Fig. 2.5b. The mid-point rule estimation method results in a robust controller that achieves the desired trajectory although it is slightly closer to the beacon than the theory predicts. The error between these two orbits is observed (~ 200 mm) to be within the size of the robot (~ 400 mm).

2.2.6 Associated Lagrangian

Here we will re-visit the problem of tracking a moving beacon as considered in Section 2.2.1. It is of specific interest to ask whether the system dynamics admits some Lagrangian formulation. Without loss of generality, at this stage we take $\nu_2 = 1$ and denote $\nu_1 = \nu$ (note that A-1 translates to $\nu < 1$). Writing $\mathbf{r} = \mathbf{r}_1 - \mathbf{r}_2$, we see that on the invariant manifold, the feedback control law (2.2) takes the form

$$u_2 = -\frac{\mathbf{r} \cdot \dot{\mathbf{r}}^{\perp}}{|\mathbf{r}|^2}.$$

Now it is a straightforward exercise to see that the baseline vector satisfies the following second order ODE:

$$\begin{aligned}\ddot{\mathbf{r}} &= \nu^2 u \mathbf{y}_1 - u_2 \mathbf{y}_2 \\ &= \nu^2 u \mathbf{y}_1 + \left(\frac{\mathbf{r}\cdot\dot{\mathbf{r}}^\perp}{|\mathbf{r}|^2}\right)\left(\frac{\mathbf{r}}{|\mathbf{r}|}\right). \end{aligned} \tag{2.14}$$

Note that here we used the fact that on the invariant manifold the bearing angle of the second agent to the beacon, $\kappa_2 = \pi/2$ and hence the $\mathbf{y}_2$ vector is aligned with the baseline vector $\mathbf{r}$, or in other words $\mathbf{y}_2 = \left(\frac{\mathbf{r}}{|\mathbf{r}|}\right)$.

Proposition 2.2.3. *On every level set of E, ($E(\rho, \kappa_1) = E_0$, as in (2.6)) the two dimensional system (2.14) is actually the Euler-Lagrange equation of the Lagrangian function (of the type kinetic energy−potential energy)*

$$\begin{aligned} L(\mathbf{r}, \dot{\mathbf{r}}) &= K(\mathbf{r}, \dot{\mathbf{r}}) - V(\mathbf{r}, \dot{\mathbf{r}}) \\ &= \frac{1}{2}|\dot{\mathbf{r}}|^2 - \left(-\frac{E_0}{|\mathbf{r}|} - \frac{1}{2}\nu u|\mathbf{r}| - \mathcal{A}(\mathbf{r})\cdot\dot{\mathbf{r}}\right), \end{aligned} \tag{2.15}$$

where $\mathcal{A}$ is defined as $\mathcal{A}(\mathbf{r}) := -\frac{1}{2}\nu u \mathbf{r}^\perp$.

Proof. Note that the quantity, $E_0 = \rho(1 + \nu\sin\kappa) - \frac{1}{2}\nu u \rho^2$ is conserved and $\mathbf{r}\cdot\dot{\mathbf{r}}^\perp = -\rho(1+\nu\sin\kappa)$. From here, we can rewrite (2.14) as

$$\begin{aligned} \ddot{\mathbf{r}} &= \nu u(\nu\mathbf{y}_1 - \mathbf{y}_2) + \left(-\frac{E_0}{|\mathbf{r}|^2} + \frac{1}{2}\nu u\right)\left(\frac{\mathbf{r}}{|\mathbf{r}|}\right) \\ &= (\dot{\mathbf{r}}\times\mathbf{B}) - \nabla\left(-\frac{E_0}{|\mathbf{r}|} - \frac{1}{2}\nu u|\mathbf{r}|\right) \\ &= (\dot{\mathbf{r}}\times\mathbf{B}) + \mathbf{E}(\mathbf{r}), \end{aligned} \tag{2.16}$$

where we introduce $\mathbf{B} := -\nu u\hat{\mathbf{z}}$, a static "magnetic field" in the direction perpendicular to the plane of motion of the agents, $\hat{\mathbf{z}}$ being the unit vector in

that direction. Also, we call $\mathbf{E}(\mathbf{r}) := -\nabla\Phi(\mathbf{r})$, the "electric field" and $\Phi(\mathbf{r}) := -\left(\frac{E_0}{|\mathbf{r}|} + \frac{1}{2}\nu u|\mathbf{r}|\right)$, the corresponding electrostatic potential.

Now, the equation (2.16) resembles with that of the equation of motion of a charged particle in an electromagnetic field and one can find obvious similarity of the right hand side with that of Lorentz force law. Then a standard result [Goldstein et al., 2001] in the theory of electromagnetism gives the Lagrangian formulation of (2.16). Since $\nabla \cdot \mathbf{B} = 0$, $\mathbf{B}$ can be written as curl of a "magnetic vector potential" $\mathcal{A}(t, \mathbf{r})$, i.e. $\mathbf{B} = \nabla \times \mathcal{A}$. Also, the electric field $\mathbf{E}$ can be written as $\mathbf{E} = -\nabla\Phi(\mathbf{r}) - \frac{\partial \mathcal{A}}{\partial t}$. Matching this with (2.16), we can see that $\mathcal{A}$ is a vector valued function of $\mathbf{r}$ only. It is a straightforward exercise to show that $\mathcal{A} = -\frac{1}{2}(\mathbf{r} \times \mathbf{B}) = -\frac{1}{2}\nu u\mathbf{r}^{\perp}$ satisfies $\mathbf{B} = \nabla \times \mathcal{A}$. Then the Lagrangian which generates (2.16) is given by

$$\begin{aligned} L(\mathbf{r}, \dot{\mathbf{r}}) &= K(\mathbf{r}, \dot{\mathbf{r}}) - V(\mathbf{r}, \dot{\mathbf{r}}) \\ &= \frac{1}{2}|\dot{\mathbf{r}}|^2 - (\Phi(\mathbf{r}) - \mathcal{A}(\mathbf{r}) \cdot \dot{\mathbf{r}}) \\ &= \frac{1}{2}|\dot{\mathbf{r}}|^2 + \frac{E_0}{|\mathbf{r}|} + \frac{1}{2}\nu u|\mathbf{r}| - \frac{1}{2}\nu u\mathbf{r}^{\perp} \cdot \dot{\mathbf{r}} \end{aligned}$$

■

Remark 2.5. In essence, Proposition 2.2.3 reveals that with open loop constant curvature control of one agent and with feedback control (2.2), namely constant bearing pursuit law with parameter $\alpha = \pi/2$, of the other, (on every level set of an invariant manifold) the coupled system behaves exactly the same way as a charged particle in a static electromagnetic field. Moreover, the magnetic field, $\mathbf{B}$ is dependent on the constant curvature (u) of the first agent. Thus $u = 0$ implies

the absence of the magnetic field and the agents are subject to the electrostatic field only. The field $\mathbf{E}$ has familiar inverse square form and hence the results for the special case $u = 0$ agree with Kepler's laws which are obtained from a two-body problem subject to Newtonian gravitational force.

2.3 Biomimetic Algorithms for Coordinated Motion

In this section, we will report implementation of two feedback control strategies on our laboratory test-bed. The first of these two strategies is called mutual motion camouflage (MMC) [Mischiati and Krishnaprasad, 2012]. Existing literature on dragonflies [Corbet, 1999] provides qualitative analysis of territorial battles, wherein the trajectories display spiraling motion consistent with the theoretical predictions [Mischiati and Krishnaprasad, 2011]. This particular bio-inspired control algorithm inherits an appealing coverage property through the mechanism of space filling curves, and our implementations are able to reproduce coverage patterns similar to the predicted ones.

Although there has been a long history of control algorithms for flocking, almost every model of collective motion predicts diffusive transport of information. But, contrary to the existing models, recent findings [Attanasi et al., 2014] from starling flocks suggest that directional information within a flock propagates with an almost constant speed, and this linear growth of information can be explained

by models with wave-like aspects. In [Dey, 2015; Halder and Dey, 2015] a control strategy called topological velocity alignment (TVA) was introduced, which conforms to this criterion and can explain how information about local neighbors can influence the agents in a flock to align their headings in a single common direction. Hence it seems reasonable to use TVA strategy for collective motion synthesis. Furthermore, our implementation results in real robots have shown that reduction in neighborhood size and external perturbation (similar to predator attack) can split a flock into smaller subgroups.

2.3.1 Mutual Motion Camouflage (MMC)

Here we consider the *mutual* interaction between two agents each applying the same pursuit law, while perceiving the other one as a target. As the dynamics of MMC in a planar setting has been studied earlier [Mischiati and Krishnaprasad, 2012], we just reiterate some key results in order to have a comprehensive framework. Allowing different speeds for the agents, we begin with the following symmetry:

$$u_1\nu_1 = u_2\nu_2 = u. \tag{2.17}$$

Then the dynamics of the relative motion vectors, namely $\mathbf{r} = \mathbf{r}_1 - \mathbf{r}_2$, $\mathbf{g} = \dot{\mathbf{r}} = \nu_1\mathbf{x}_1 - \nu_2\mathbf{x}_2$ and $\mathbf{h} = \mathbf{g}^{\perp} = \dot{\mathbf{r}}^{\perp}$, can be expressed as

$$\begin{aligned} \dot{\mathbf{r}} &= \mathbf{g} \\ \dot{\mathbf{g}} &= u\mathbf{h} \\ \dot{\mathbf{h}} &= -u\mathbf{g}. \end{aligned} \tag{2.18}$$

Now we introduce three scalar shape variables defined as $\rho = |\mathbf{r}|$, $\gamma = (\mathbf{r} \cdot \mathbf{g})/|\mathbf{r}|$ and $\lambda = (\mathbf{r} \cdot \mathbf{h})/|\mathbf{r}|$. Then, according to [Justh and Krishnaprasad, 2006], we have

$$u = -\mu \left(\frac{\mathbf{r}}{|\mathbf{r}|} \cdot \dot{\mathbf{r}}^{\perp} \right) = -\mu \left(\frac{\mathbf{r}}{|\mathbf{r}|} \cdot \mathbf{h} \right) = -\mu\lambda, \tag{2.19}$$

where, $\mu > 0$ denotes the feedback gain. As shown earlier, the dynamics of relative motion (2.18) can be reduced to yield a second order dynamics given by

$$\begin{aligned} \dot{\rho} &= \gamma \\ \dot{\gamma} &= (1/\rho - \mu)\left(\delta^2 - \gamma^2\right), \end{aligned} \tag{2.20}$$

where, $\delta = |\mathbf{g}| = |\mathbf{h}|$ is conserved along any trajectory of (2.18). As detailed in the original work [Mischiati and Krishnaprasad, 2012], individual trajectories can be reconstructed from the solutions of (2.20). Moreover, the solutions of the reduced dynamics (2.20) constitute level sets for another conserved quantity, defined as

$$E(\rho, \gamma) = \rho^2(\delta^2 - \gamma^2)e^{-2\mu\rho} = E(\rho_0, \gamma_0). \tag{2.21}$$

However, the absence of damping in the reduced dynamics (2.20) has potential to deteriorate the performance of the original MMC law (2.19). A modified feedback law, with an added dissipative term to neutralize any deviation from the predicted trajectories, can be expressed as

$$u_{tot} = u + u_{dis} = -\mu\lambda + k_d\lambda\gamma\big(E(\rho, \gamma) - E_d\big), \tag{2.22}$$

where E_d is set as the initial value of the conserved quantity $E(\rho, \gamma)$, *i.e.* $E_d = E(\rho_0, \gamma_0)$. Previous work [Mischiati and Krishnaprasad, 2010] has shown that this modified control law (2.22) with $k_d > 0$ makes the periodic orbit (with energy E_d)

orbitally asymptotically stable, and the corresponding domain of attraction is characterized by $\{(\rho,\gamma) : \rho > 0, -\delta < \gamma < \delta, (\rho,\gamma) \neq (1/\mu, 0)\}$.

2.3.2 Topological Velocity Alignment (TVA)

Here we formalize the strategy of topological velocity alignment (TVA) [Halder and Dey, 2015; Dey, 2015], and assume that each member in a group of n-agents uses this strategy to move together while keeping its heading parallel to the neighborhood center of mass velocity. Letting $\mathcal{N}_i$ denote the neighborhood of the i-th agent, the center of mass (COM) velocity of this neighborhood is given by

$$\mathbf{v}_{COM} = \frac{1}{|\mathcal{N}_i|} \sum_{j \in \mathcal{N}_i} \nu_j \mathbf{x}_j, \tag{2.23}$$

where $|\mathcal{N}_i|$ represents the number of neighbors influencing the i-th agent. Next, by assuming that $\mathbf{v}_{COM}$ does not vanish to zero, we define the direction of the center of mass motion as

$$\mathbf{x}_{\mathcal{N}_i} = \frac{\mathbf{v}_{COM}}{|\mathbf{v}_{COM}|}. \tag{2.24}$$

It should be noted that $\mathbf{x}_{\mathcal{N}_i}$ is *not well-defined over a thin set in the state space*. As the chance of getting into the thin set is very small, we can overlook this situation for all practical purposes. Now we introduce a contrast function

$$\Theta_i = \frac{1}{2} (\mathbf{x}_{\mathcal{N}_i} - \mathbf{x}_i) \cdot (\mathbf{x}_{\mathcal{N}_i} - \mathbf{x}_i) = 1 - \mathbf{x}_i \cdot \mathbf{x}_{\mathcal{N}_i}, \tag{2.25}$$

as a quantitative measure for the misalignment between the heading of an agent and the direction of motion of its neighborhood center of mass. Clearly, this contrast function (Θ_i) assumes its minimum value ($= 0$) whenever the i-th agent's

velocity is aligned with its neighborhood center of mass velocity, and increases monotonically with increase in the misalignment between them. Thus, Θ_i can be interpreted as a measure of departure from our goal of achieving alignment.

Next, by assuming a non-zero velocity for the neighborhood center of mass ($\mathbf{v}_{COM} \neq 0$), the TVA law is given by [Dey, 2015]

$$u_i = \mu \left(\frac{\mathbf{x}_{\mathcal{N}_i} \cdot \mathbf{y}_i}{\nu_i} \right), \tag{2.26}$$

where $\mu > 0$ denotes a positive gain, and $\mathbf{y}_i$ carries its usual meaning. Alternatively, lateral acceleration for this choice of control laws (2.26) can be expressed as

$$\mathrm{a}_i^{lat} = \mu\nu_i \big(\mathbf{x}_{\mathcal{N}_i} - \big[\mathbf{x}_{\mathcal{N}_i} \cdot \mathbf{x}_i \big] \mathbf{x}_i \big), \tag{2.27}$$

and this provides a physical intuition behind (2.26) as the lateral acceleration is proportional to the projection of the normalized velocity of its neighborhood center of mass onto the transverse of its own direction of motion.

Remark 2.6. Earlier works [Justh and Krishnaprasad, 2003, 2004] have considered a very similar form of this control law with three components for attraction (while the agents are far away), repulsion (to avoid collision) and velocity alignment. However, the TVA control law considers only velocity alignment, but extends the scope from a planar setting to a three dimensional environment. Moreover it relaxes the assumption on uniform speed of the collective by allowing the agents non-uniform and time-varying speed profiles. This relaxation plays an important role in the context of applying this control law to a group of heterogeneous agents.

It was shown in [Halder and Dey, 2015; Dey, 2015], for a two agent system it is possible to show that the TVA strategy (2.26) aligns the velocity of the agents, only if their velocity vectors were not exactly opposite to each other initially. [Dey, 2015] also provides further analytical results for a general n agent system with a cyclic interaction scenario. As analysis of an n-agent system with neighborhood defined as the set of K-nearest neighbors poses hard challenges, we propose an algorithmic way (Algorithm 2) to implement TVA in a real system. We bring in an additional neighbor into consideration whenever $\mathbf{v}_{COM}$ becomes zero. Clearly, this provides a way to avoid ill-posedness associated with $\mathbf{v}_{COM}$ being zero because non-zero speeds of individual agents ensure that considering an extra neighbor will make an otherwise zero $\mathbf{v}_{COM}$ non-zero.

2.3.3 Implementation Results

We present the implementation results of the two control laws in our robotic test-bed. In this section, we are presenting results for which the speeds of all the individual agents are same, i.e. $\nu_i = \nu_j, \forall i, j$. Though it should be noted that both control laws can be implemented with different speeds.

2.3.3.1 Implementation of MMC

Here we will show some implementation results for MMC, and demonstrate the effectiveness of using a dissipative control term (2.22). Our analysis also includes a comparison between the observed trajectories and trajectories obtained from

Algorithm 2: Topological Velocity Alignment

Data: Initial Time - $t_{initial}$; Final Time - t_{final}; Sampling Interval - Δ; Number of Agents - n; Initial Position and Orientation - $\{g_i\}_{i=1}^n$; Neighborhood Size - K

begin

- **Initialize**: $t_{current} \longleftarrow t_{initial}$;
- **for** $i = 1$ *to* n **do**
  - **Initialize**: State - $X_i \longleftarrow g_i$;
- **while** $t_{current} \leq t_{final}$ **do**
  - **for** $i = 1$ *to* n **do**
    - **Define**: $\mathcal{N}_i$ - the set of K-nearest neighbors ;
    - **Compute**: Neighborhood center of mass velocity - $\mathbf{v}_{COM}$;
    - **if** $\mathbf{v}_{COM} = 0$ **then**
      - **Define**: $\mathcal{N}_i$ - the set of $K+1$-nearest neighbors ;
      - **Compute**: Neighborhood center of mass velocity - $\mathbf{v}_{COM}$;
    - **Compute**: Steering control - u_i;
  - **Implement**: Steering Control - $\{u_i\}_{i=1}^n$;
  - **Update**: State - $\{X_i\}_{i=1}^n$;
  - **Update**: Time - $t_{current} \longleftarrow t_{current} + \Delta$;

theoretical predictions, obtained via integrating the reduced system dynamics (2.20). Considering the prersence of a conserved quantity (2.6) in the system, we used the method described in [Austin et al., 1993] for integration instead of general ODE solver, which otherwise would not be able to keep the quantity $E(\rho, \gamma)$ constant to its initial value. Then, from the updated values of ρ^k and γ^k, we reconstruct the trajectories along with their frame vectors, i.e. $\mathbf{r_i}^k$, $\mathbf{x_i}^k$, $\mathbf{y_i}^k$, with $i = 1, 2$ and k denoting the time indices. At each time instance t^k, the error

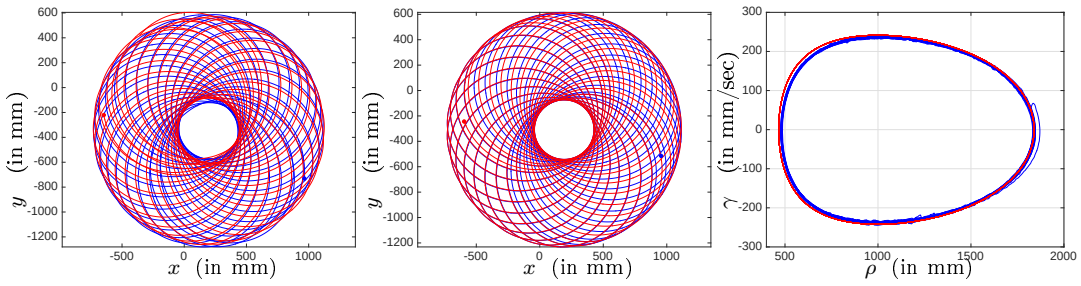

(a) Trajectory (Experiment) (b) Trajectory (Simulation) (c) Phase plot

Figure 2.6: Performance of the system significantly improved upon addition of the dissipative control term (with $\mu = 0.001$ mm^{-1}, $\nu_1 = \nu_2 = 200$ mm/sec and $k_d = 1 \times 10^{-15}$ mm^{-6}sec^3)

(e_i^k) is computed as: $e_i^k = |\mathbf{r}_{i,expt}^k - \mathbf{r}_{i,ideal}^k|$.

The plots of a sample run using the modified MMC feedback law (2.22) are shown in Fig 2.6. This modified control law has been applied with $k_d = 1 \times 10^{-15}$ mm^{-6}sec^3, and the parameters μ, ν_1 and ν_2 are selected as 0.001 mm^{-1}, 200 mm/sec and 200 mm/sec, respectively. The resulting performance is quite satisfactory as shown in Fig 2.6a (refer [YouTube] for implementation video). We have also observed that the error is bounded ($\sim$ 250 mm) within the size of the robots ($\sim$ 400 mm).

2.3.3.2 Implementation of TVA

We implemented the TVA control law (2.26) in a 2 dimensional setting (i.e. $v_i(t)$ is ignored). As the implementation is in discrete time, we followed Algorithm 2 in our implementation in order to avoid the singular case of $|\mathbf{v}_{COM}| = 0$. To demonstrate the performance of TVA control law, we designed three different experiments (refer

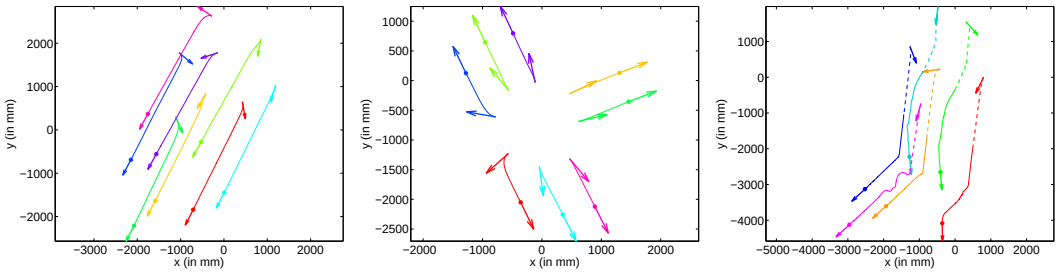

(a) Trajectories: 8 agents, flocking

(b) Trajectories: 8 agents, splitting

(c) Trajectories: 6 agents, perturbation

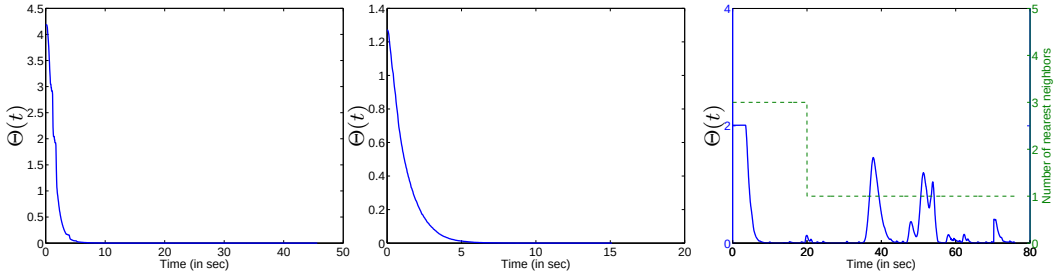

(d) Contrast Function: 8 agents, flocking

(e) Contrast Function: 8 agents, splitting

(f) Contrast Function: 8 agents, perturbation

Figure 2.7: Robot trajectories and contrast functions of TVA for (i) Experiment 1 [Fig (a),(d)] with 8 agents, demonstrates flocking behavior ($K = 3$); (ii) Experiment 2 [Fig (b),(e)] with 8 agents, describes the splitting behavior due to low neighborhood size ($K = 1$), and (iii) Experiment 3 [Fig (c),(f)] with 6 agents, shows that perturbation can cause a swarm to split, the trajectory of the perturbing agent is not shown. ($\mu = 1$ Hz and $\nu_i = 60$ mm/sec is kept fixed for all experiments.)

[YouTube] for implementation videos). In these experiments, the sonar sensors on the robots were activated to sense any obstacle in the direction of motion of the robots and if any robot can sense such an obstacle, it will simply apply a maximum *turning rate* (ω^{sat}) to avoid collision. The sonars are programmed to

detect an obstacle only in close proximity ($\sim$ 300 mm) of the robots. In all our experiments ω^{sat} is taken to be 50 rad/sec, forward speeds of all of the robots are kept constant at 60 mm/sec and the value of the parameter μ is chosen to be 1 Hz. A system with eight agents is considered and we apply same TVA law to all of them. The neighborhood size is taken to be three (i.e. $K = 3$). The robots are initially placed in arbitrary positions and directions. The footprints of the robots and the corresponding contrast function, $\Theta(t) = \sum_i \Theta_i(t)$ is plotted against time in Fig 2.7a, 2.7d. The initial and final directions of the robots are shown using arrows and the final positions of the robots are denoted using dots. It can be seen from Fig 2.7d that the contrast function decays to zero very quickly which indicates perfect velocity alignment within the swarm. Next we decreased the neighborhood size and made it one ($K = 1$), so that every robot only 'communicates' with its closest neighbor. We chose the initial positions in such a way that they may form sub-clusters instead of moving as a single swarm. This behavior is called '*splitting*' in a swarm. From Fig 2.7b, we can clearly see that the swarm of eight robots gradually split from each other and form three different clusters. It is to be noted that even if all the agents are not going in the same direction, the contrast function still converges to zero (Fig 2.7e). This happens because each of the robots are aligned with their nearest neighbors and hence each of the individual contrast functions ($\Theta_i(t)$) are zero. This experiment may explain the splitting phenomenon observable in nature. Lastly, we combined the above two experiments, and conducted an experiment using six robots in a

swarm and another robot as a predator. A separate computer was used for manual control of the 'predator' robot.

At the beginning, neighborhood size is kept at $K = 3$, such that the 'communication' graph among the robots stays connected and they move as an entire swarm in a common direction. When the swarm comes close to the predator, the neighborhood size is decreased to one. As we are not using any onboard visual sensing and the sonar sensing is done only in very close region (~ 300 mm), the change in neighborhood size is made manually. From Fig 2.7f, we can see that the change in neighborhood size takes place at around 20 seconds and we can also see a tiny jump in the contrast function at that time. The predator then slowly approaches to one of the agents in the swarm, which abiding to its collision avoidance rule, turns to avoid the predator. In Fig 2.7c, the trajectories of the agents are drawn in dashed lines before the occurrence of this event and in solid lines afterwards. The trajectory of the predator robot in not shown in the figure. After creating the initial perturbation, the predator is slowly moved through the swarm causing some subsequent disturbances. These perturbations create a noticeable impact in the swarm. As the attacked agent turns, its neighbor also tries to align itself with that agent and so does its neighbor. This goes on until the communication graph becomes disconnected and a split in the swarm is then observed [YouTube] just like in Experiment 2. As we can see in Fig 2.7c, the swarm is divided in two groups after the attack of the predator. The jumps in plot of the contrast function in Fig 2.7f symbolize the perturbations caused by

the external agent. The contrast function eventually converges to zero after the members are aligned with their neighbors within each subgroup.

Chapter 3

Optimal Steering of Agents on a Plane

3.1 Introduction

The kinematic unicycle model is often used in path-planning for ground vehicles, since the configuration of a ground vehicle can often be represented by a point in a plane that is constrained to move in the direction of the current heading [Bellaïche et al., 1998; LaValle, 2006]. The state of this system can be represented as an element of the special Euclidean group SE(2), where the control inputs are a curvature input which controls the rate of change of the heading angle, and a velocity input which controls the rate of change of the unicycle position in the direction of the heading angle.

Given the current configuration of the unicycle and a desired future configuration, an admissible path for moving the unicycle from an initial to a final configuration can be determined via the minimization of some cost functional. There can be many variations to this problem depending on the chosen cost func-

tional. A much celebrated problem is the problem of Euler's elastica [Euler, 1744] where the minimum curvature path joining two given configurations on the plane is considered. Particularly elegant and other well-known variations include the minimum-time solutions of [Dubins, 1957] and [Reeds and Shepp, 1990]. Optimal paths of the minimum-time problem consist only of straight-line and circular-arc segments which, when patched together, create discontinuities in the path curvature and cause potential difficulty in implementation since abrupt changes in curvature are hard to track. Proposed modifications that alleviate this problem enforce that the curvature stay continuous, *e.g.*, [Fraichard and Scheuer, 2004], yet it is also possible to penalize the total curvature along the path in the expectation that the optimal curvature will be continuous. [Halder and Kalabic, 2017] takes the latter approach, considering the minimization of the curvature along a path connecting initial and final unicycle configurations with free final time.

In this chapter, we will present a problem that penalizes both the curvature and speed controls in maneuvering a unicycle from initial to desired final configuration. This helps both the curvature and speed controls to be smooth along an optimal trajectory. These optimal trajectories closely resemble to those obtained in [Halder and Kalabic, 2017]. Our solution is obtained using geometric optimal control, where the necessary conditions for optimality are obtained via the Pontryagin Maximum Principle (PMP), and Lie-Poisson reduction [Krishnaprasad, 1993; Ohsawa, 2013]. Using geometric optimal control on SE(2) to find solutions to path-planning problems has also been considered by [Sussmann and Tang, 1991;

Krishnaprasad, 1993; Agrachev and Sachkov, 2004; Dey and Krishnaprasad, 2014; Justh and Krishnaprasad, 2015b].

Studying a unicycle on the plane is important since often a collective of N agents exhibits single agent behavior under synchronization. In the later part of this chapter, we will present a framework for analyzing such a collective. This framework is based on [Justh and Krishnaprasad, 2015b], where every agent was assumed to have constant speed. Here we will, however, consider a cost function that penalizes both speed and curvature controls. In addition to the individual control costs, there is one cost that is attributed to the 'mismatch in control' of an agent with its 'neighbors'. The neighbors of any agent is dictated by a fixed graph of interaction. The strength of such interaction is captured by a coupling parameter. It is shown that in extreme cases (no coupling and high coupling) the optimal collective controls are directly associated with optimal controls for a single agent problem. This framework is what we use in the later chapters of this thesis where we consider optimal control problems for a continuum of agents.

3.2 Optimal Steering of a Unicycle

In this section, we consider minimizing the curvature and speed control costs of a path in $SE(2)$ connecting an initial unicycle configuration g_0 with its desired final configuration g_T at time T. We formulate this optimization as a geometric optimal control problem and derive the necessary conditions using PMP and Lie-Poisson reduction. From the necessary conditions, we show that there are two

constants of motion: the Hamiltonian and the Casimir. We show that there are three possible families of solutions depending on the values of Casimir and the Hamiltonian. In the first case, the motion consists of segments of a U-turn; in the second case, the motion consists of segments of parallel parking trajectories; in the third case, the motion consists of straight lines or asymptotic approaches thereto.

Consider the unicycle kinematic equations,

$$\dot{x}(t) = v(t)\cos\theta(t), \tag{3.1a}$$

$$\dot{y}(t) = v(t)\sin\theta(t), \tag{3.1b}$$

$$\dot{\theta}(t) = u(t), \tag{3.1c}$$

where $(x(t), y(t)) \in \mathbb{R}^2$ is the position of the unicycle on the Cartesian plane, $\theta(t) \in S^1$ is the heading of the unicycle, $v(t)$ is the unicycle speed control, and $u(t)$ is the steering control, equal to the rate of change of the heading $\theta(t)$.

The configuration of the unicycle can be represented as an element of the matrix Lie group SE(2). Let $g(t) \in \mathrm{SE}(2)$ where,

$$g(t) = \begin{bmatrix} \cos\theta(t) & -\sin\theta(t) & x(t) \\ \sin\theta(t) & \cos\theta(t) & y(t) \\ 0 & 0 & 1 \end{bmatrix}. \tag{3.2}$$

Then the equations (3.1) can be written in left-invariant form,

$$\dot{g}(t) = g(t)\xi(u(t), v(t)), \tag{3.3}$$

where,

$$\xi(u(t), v(t)) = u(t)X_1 + v(t)X_2, \tag{3.4}$$

and,

$$X_1 = \begin{bmatrix} 0 & -1 & 0 \\ 1 & 0 & 0 \\ 0 & 0 & 0 \end{bmatrix}, \; X_2 = \begin{bmatrix} 0 & 0 & 1 \\ 0 & 0 & 0 \\ 0 & 0 & 0 \end{bmatrix}. \tag{3.5}$$

The matrices X_1 and X_2 are elements of the Lie algebra $\mathfrak{se}(2)$. Together with $X_3 = [X_1, X_2] = X_1X_2 - X_2X_1$, X_1 and X_2 form a basis for $\mathfrak{se}(2)$.

Without loss of generality, we can assume that $g_0 = I_3$, since $g(t)$ can always be redefined according to $g(t) := g_0^{-1}g(t)$. Given a final time $T > 0$ and a final state g_T, cost function to be minimized is,

$$\frac{1}{2}\int_0^T \left(u(t)^2 + v(t)^2\right) dt. \tag{3.6}$$

3.2.1 Optimal Control Solution

In order to solve the problem we form the pre-Hamiltonian,

$$H = \langle p, g\xi(u,v)\rangle - \frac{1}{2}(u^2 + v^2), \tag{3.7}$$

where $p(t) \in \mathrm{SE}(2)^*$ is the adjoint variable. To simplify the Hamiltonian, we perform Lie-Poisson reduction, introducing the variable $\mu(t) \in \mathfrak{se}(2)^*$ satisfying the translation to identity,

$$\langle \mu, \xi(u,v)\rangle = \langle p, g\xi(u,v)\rangle.$$

As an element of the dual space, $\mu(t)$ can be represented as $\mu(t) = \mu_1 X_1^\flat + \mu_2 X_2^\flat + \mu_3 X_3^\flat$, where $\{X_1^\flat, X_2^\flat, X_3^\flat\}$ are the basis vectors dual to $\{X_1, X_2, X_3\}$.

The pre-Hamiltonian therefore becomes,

$$\begin{aligned} H(\mu, u, v) &= \langle \mu, \xi(u, v) \rangle - \frac{1}{2}(u^2 + v^2), \\ &= \langle \mu_1 X_1^\flat + \mu_2 X_2^\flat + \mu_3 X_3^\flat, uX_1 + vX_2 \rangle \\ &\qquad - \frac{1}{2}(u^2 + v^2), \\ &= \mu_1 u + \mu_2 v - \frac{1}{2}(u^2 + v^2). \end{aligned}$$

According to the PMP, the optimal control (u^*, v^*) satisfies,

$$H(\mu^*, u^*, v^*) = \max_{(u,v)\in\mathbb{R}^2} H(\mu^*, u, v). \tag{3.8}$$

Therefore the optimal controls are given by,

$$u_1^* = \mu_1, \tag{3.9}$$

$$u_2^* = \mu_2, \tag{3.10}$$

The reduced Hamiltonian is therefore,

$$H = H(\mu, u_1^*, u_2^*) = \frac{1}{2}\left(\mu_1^2 + \mu_2^2\right), \tag{3.11}$$

and the dynamics of the μ_i variables are given by [Krishnaprasad, 1993],

$$\begin{bmatrix} \dot{\mu}_1 \\ \dot{\mu}_2 \\ \dot{\mu}_3 \end{bmatrix} = \begin{bmatrix} 0 & -\mu_3 & \mu_2 \\ \mu_3 & 0 & 0 \\ -\mu_2 & 0 & 0 \end{bmatrix} \frac{\partial h}{\partial(\mu_1, \mu_2, \mu_3)}, \tag{3.12}$$

$$\dot{\mu}_1 = -\mu_2\mu_3, \tag{3.13a}$$

$$\dot{\mu}_2 = \mu_1\mu_3, \tag{3.13b}$$

$$\dot{\mu}_3 = -\mu_1\mu_2. \tag{3.13c}$$

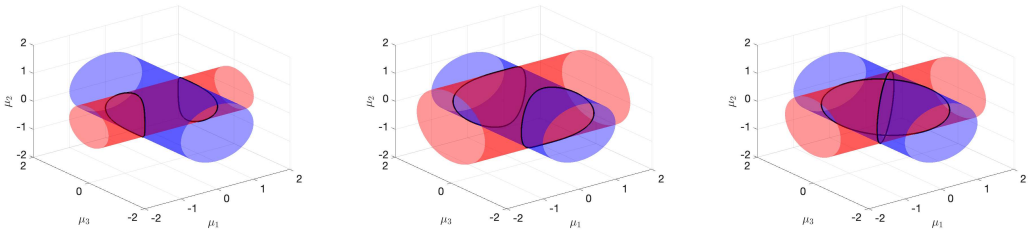

(a) $c = 0.5$ (b) $c = 1.5$ (c) $c = 1$

Figure 3.1: $\mathcal{M}$ (black) plotted as an intersection of $\mathcal{C}$ (red) and $\mathcal{H}$ (blue) for $h = 1$ and three values of the Casimir c

Let,

$$c = \mu_2^2 + \mu_3^2. \tag{3.14}$$

This variable is called the Casimir and it is a constant of motion, implying that the variables μ_2 and μ_3 evolve on circle of radius $\sqrt{c}$. Along with the Casimir, the Hamiltonian (3.11) is also a conserved quantity of motion. For convenience of subsequent calculations, we will work with the following scaled Hamiltonian,

$$h = 2H = \mu_1^2 + \mu_2^2. \tag{3.15}$$

3.2.2 Characterizing the Types of Motion

According to (3.14) and (3.15), the dynamics (3.13) evolve on the manifold $\mathcal{M}$ where,

$$\begin{aligned} \mathcal{M} &= \mathcal{C} \cap \mathcal{H}, \\ \mathcal{C} &= \{(\mu_1, \mu_2, \mu_3) \in \mathbb{R}^3 : c = \mu_2^2 + \mu_3^2\}, \\ \mathcal{H} &= \{(\mu_1, \mu_2, \mu_3) \in \mathbb{R}^3 : h = \mu_1^2 + \mu_2^2\}. \end{aligned} \tag{3.16}$$

The manifold $\mathcal{M}$ is one-dimensional and equal to the intersection of the cylinders $\mathcal{C}$ and $\mathcal{H}$. The shape of $\mathcal{M}$ is determined by the Casimir c, while the shape of $\mathcal{H}$ is determined by h. The motion of μ evolves on $\mathcal{M}$. Due to continuity, it must evolve on a connected component of $\mathcal{M}$, so it is important to consider the types of possible intersections, of which there are three corresponding to three different cases: in Case 1, $\mathcal{C}$ is strictly smaller than $\mathcal{H}$; in Case 2, $\mathcal{C}$ is strictly larger than $\mathcal{H}$; in Case 3, $\mathcal{C}$ is equal in size to $\mathcal{H}$. To perform a case-by-case categorization of $\mathcal{M}$, we note that, according to (3.14), the variable μ_2 is restricted to $\pm\sqrt{c}$ and, according to (3.15), μ_2 is restricted to $\pm\sqrt{h}$. In Case 1, $c < h$, so $|\mu_2| \leq \sqrt{c} < \sqrt{h}$. Therefore the motion evolves on a connected component of $\mathcal{M}$ where μ_1 does not change sign since $\mu_1^2 = h - \mu_2^2 \geq h - c > 0$. Similarly, in Case 2, $c > h$, so $|\mu_2| \leq \sqrt{h} < \sqrt{c}$. The motion evolves on a connected component of $\mathcal{M}$ where μ_3 does not change sign since $\mu_3^2 = c - \mu_2^2 \geq c - h > 0$. In Case 2, $c = h$, so the two constraints agree at the extremes. Instead of having $\mathcal{M}$ as a one connected component, it actually has four disconnected components. These components meet each other asymptotically at the extremes $\mu_1 = \mu_3 = 0, \mu_2 = \pm\sqrt{h}$. See Fig. 3.1 for a visualization of the three cases. In the following, we study the three types of motion in further detail.

Case 1: $0 < c < h$

The equations (3.13) admit the following explicit solutions by means of Jacobian

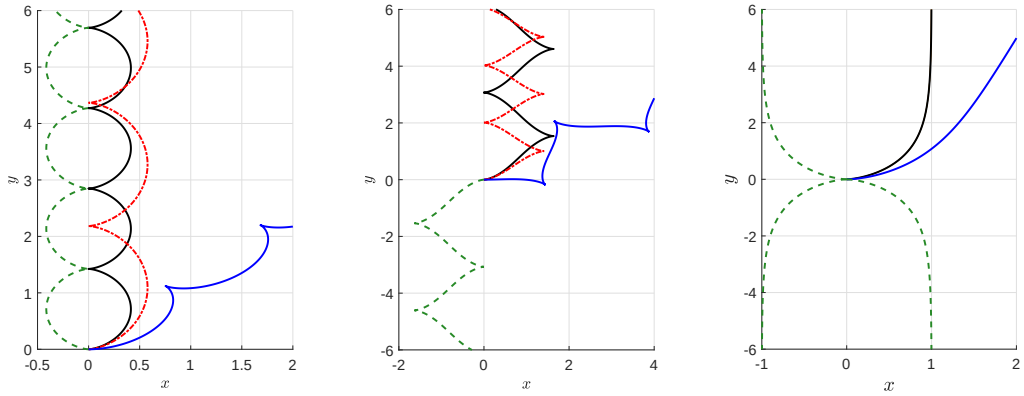

(a) $c = 0.5$ (solid black) and 0.75 (dot-dashed red)

(b) $c = 1.5$ (solid black) and 2 (dot-dashed red)

(c) $c = 1$

Figure 3.2: Extremal trajectories for different cases (solid black) – increasing c produces the dot-dashed red curve; increasing η produces the solid blue curve; changing s_1 or s_2 produces the dashed green curve. $h = 1$ for all three cases.

elliptic functions [Davis, 1962; Byrd and Friedman, 1971],

$$\mu_1 = s_1\sqrt{h}\ \mathrm{dn}\left(\sqrt{h}(t+\eta), k\right), \tag{3.17a}$$

$$\mu_2 = s_1\sqrt{c}\ \mathrm{sn}\left(\sqrt{h}(t+\eta), k\right), \tag{3.17b}$$

$$\mu_3 = \sqrt{c}\ \mathrm{cn}\left(\sqrt{h}(t+\eta), k\right), \tag{3.17c}$$

where the modulus k of the elliptic functions is given by $k^2 = \frac{c}{h}$. The parameters $s_1 \in \{1, -1\}$ and $\eta \in \mathbb{R}$ do not depend on c and h, but on the endpoint constraints. Note that these solutions are periodic with the period given by $T_1 := \frac{4K(k)}{\sqrt{h}}$, where $K(k)$ denotes the complete elliptic integral of the first kind.

Proposition 3.2.1. *Let $0 < c < h$. Assume $\eta = 0$, then any extremal trajectory*

is given by,

$$x(t) = \frac{s_1}{k}\left(1 - \mathrm{dn}\left(\sqrt{h}t, k\right)\right) \tag{3.18a}$$

$$y(t) = \frac{1}{k}\left(\sqrt{h}t - E\left(\mathrm{am}\left(\sqrt{h}t, k\right), k\right)\right) \tag{3.18b}$$

$$\theta(t) = s_1 \cdot \mathrm{am}\left(\sqrt{h}t, k\right) = s_1 \cos^{-1}\left(\mathrm{cn}\left(\sqrt{h}t, k\right)\right) = s_1 \sin^{-1}\left(\mathrm{sn}\left(\sqrt{h}t, k\right)\right), \tag{3.18c}$$

where $E(\cdot, \cdot)$ denotes the incomplete elliptic integral of the second kind.

Proof. We have from (3.9) and (3.17a),

$$u_1 = \mu_1 = s_1\sqrt{h}\ \mathrm{dn}\left(\sqrt{h}t, k\right).$$

Integrating the equation $\dot{\theta} = u_1$ gives

$$\theta(t) = s_1 \cdot \mathrm{am}\left(\sqrt{h}t, k\right) = s_1 \cos^{-1}\left(\mathrm{cn}\left(\sqrt{h}t, k\right)\right) = s_1 \sin^{-1}\left(\mathrm{sn}\left(\sqrt{h}t, k\right)\right).$$

Since the optimal speed control is given by (3.10) and (3.17b),

$$u_2 = \mu_2 = s_1\sqrt{c}\ \mathrm{sn}\left(\sqrt{h}t, k\right),$$

we may now integrate x and y dynamics to obtain position variables as functions of time. We have,

$$\begin{aligned} x(t) &= \int_0^t u_2 \cos(\theta(t))dt \\ &= \int_0^t s_1\sqrt{c}\ \mathrm{sn}\left(\sqrt{h}t, k\right)\mathrm{cn}\left(\sqrt{h}t, k\right)dt \\ &= -s_1\frac{\sqrt{c}}{\sqrt{h}} \cdot \frac{1}{k^2}\left[\mathrm{dn}\left(\sqrt{h}t, k\right)\right]_{t=0}^{t} \\ &= \frac{s_1}{k}\left(1 - \mathrm{dn}\left(\sqrt{h}t, k\right)\right) \end{aligned} \tag{3.19}$$

Similarly,

$$\begin{aligned} y(t) &= \int_0^t u_2 \sin(\theta(t))dt \\ &= \int_0^t \sqrt{c}\, \mathrm{sn}^2\left(\sqrt{h}t, k\right) dt \\ &= \frac{\sqrt{c}}{\sqrt{h}} \cdot \frac{1}{k^2}\left[\sqrt{h}t - E\left(\mathrm{am}\left(\sqrt{h}t, k\right), k\right)\right]_{t=0}^{t} \\ &= \frac{1}{k}\left(\sqrt{h}t - E\left(\mathrm{am}\left(\sqrt{h}t, k\right), k\right)\right) \end{aligned} \tag{3.20}$$

■

Studying the extremal trajectories in $\eta = 0$ case is important since any other trajectory can be expressed by means of these trajectories after a suitable translation and rotation. This is demonstrated in the following proposition.

Proposition 3.2.2. *Assume $0 \leq c < h$. Let us denote an extremal trajectory belonging to $\eta = 0$ case by $(x_0(t), y_0(t), \theta_0(t))$ according to (3.18). Then any extremal trajectory generated by (3.17) can be expressed as,*

$$\begin{bmatrix} x(t) \\ y(t) \end{bmatrix} = R(-\psi)\left(\begin{bmatrix} x_0(t+\eta) \\ y_0(t+\eta) \end{bmatrix} - \begin{bmatrix} x_0(\eta) \\ y_0(\eta) \end{bmatrix}\right), \tag{3.21}$$

$$\theta(t) = \theta_0(t+\eta) - \theta_0(\eta), \tag{3.22}$$

where $R(\cdot)$ is the planar rotation matrix and ψ is defined as,

$$\psi := s \cdot \mathrm{am}\left(\sqrt{h}\,\eta\right) = \theta_0(\eta). \tag{3.23}$$

Proof. Indeed, equation (3.22) is readily achieved by integrating (3.17a). Further, notice that

$$\begin{aligned}\dot{x}(t) &= s_1\sqrt{c}\,\mathrm{sn}\left(\sqrt{h}(t+\eta),k\right)\cos\left(s_1\cdot\mathrm{am}\left(\sqrt{h}(t+\eta),k\right)-\psi\right)\\ &= \sqrt{c}\left(s_1\cdot\cos(\psi)\cdot\mathrm{sn}\left(\sqrt{h}(t+\eta),k\right)\mathrm{cn}\left(\sqrt{h}(t+\eta),k\right)\right.\\ &\qquad\left.+\sin(\psi)\cdot\mathrm{sn}^2\left(\sqrt{h}(t+\eta),k\right)\right),\end{aligned}$$

and,

$$\begin{aligned}\dot{y}(t) &= s_1\sqrt{c}\,\mathrm{sn}\left(\sqrt{h}(t+\eta),k\right)\sin\left(s_1\cdot\mathrm{am}\left(\sqrt{h}(t+\eta),k\right)-\psi\right)\\ &= \sqrt{c}\left(-s_1\cdot\sin(\psi)\cdot\mathrm{sn}\left(\sqrt{h}(t+\eta),k\right)\mathrm{cn}\left(\sqrt{h}(t+\eta),k\right)\right.\\ &\qquad\left.+\cos(\psi)\cdot\mathrm{sn}^2\left(\sqrt{h}(t+\eta),k\right)\right).\end{aligned}$$

Compactly, we have

$$\begin{bmatrix}\dot{x}(t)\\ \dot{y}(t)\end{bmatrix} = \begin{bmatrix}\cos(\psi) & \sin(\psi)\\ -\sin(\psi) & \cos(\psi)\end{bmatrix}\cdot\begin{bmatrix}\dot{x}_0(t+\eta)\\ \dot{y}_0(t+\eta)\end{bmatrix}. \tag{3.24}$$

Integration of (3.24) yields (3.21). ∎

Case 2: $c > h$

This case admits solutions analogous to those of Case 1 and we will proceed in a similar way. To start, we write down solutions to (3.13) as,

$$\mu_1 = \sqrt{h}\,\mathrm{cn}\left(\sqrt{c}(t+\eta),k\right), \tag{3.25a}$$

$$\mu_2 = s_2\sqrt{h}\,\mathrm{sn}\left(\sqrt{c}(t+\eta),k\right), \tag{3.25b}$$

$$\mu_3 = s_2\sqrt{c}\,\mathrm{dn}\left(\sqrt{c}(t+\eta),k\right), \tag{3.25c}$$

with the modulus $k^2 = \frac{h}{c}$. $s_2 \in \{1, -1\}$ and $\eta \in \mathbb{R}$ are similar parameters as in case 1. These solutions are periodic as well, with period given by $T_2 := \frac{4K(k)}{\sqrt{c}}$.

Proposition 3.2.3. *Let $h > 0$ and $c > h$. Assume $\eta = 0$, then any extremal trajectory is given by,*

$$x(t) = s_2 \cdot k \left(1 - \operatorname{cn}\left(\sqrt{c}\, t, k\right)\right) \tag{3.26a}$$

$$y(t) = s_2 \left(\sqrt{c}\, t - E\left(\operatorname{am}\left(\sqrt{c}\, t, k\right), k\right)\right) \tag{3.26b}$$

$$\theta(t) = \cos^{-1}\left(\operatorname{dn}\left(\sqrt{c}\, t, k\right)\right) = \sin^{-1}\left(k \operatorname{sn}\left(\sqrt{c}\, t, k\right)\right), \tag{3.26c}$$

where $E(\cdot, \cdot)$ denotes the incomplete elliptic integral of the second kind.

Proof. The proof is similar to that of Proposition 3.2.1 and uses elementary integrals of Jacobi elliptic functions. ■

Analogous to Proposition 3.2.2, we have the following result.

Proposition 3.2.4. *Assume $h > 0$ and $c > h$. Let us denote an extremal trajectory belonging to $\eta = 0$ case by $(x_0(t), y_0(t), \theta_0(t))$ according to (3.26). Then any extremal trajectory generated by (3.17) can be expressed as,*

$$\begin{bmatrix} x(t) \\ y(t) \end{bmatrix} = R(-\psi) \left(\begin{bmatrix} x_0(t+\eta) \\ y_0(t+\eta) \end{bmatrix} - \begin{bmatrix} x_0(\eta) \\ y_0(\eta) \end{bmatrix} \right), \tag{3.27}$$

$$\theta(t) = \theta_0(t+\eta) - \theta_0(\eta), \tag{3.28}$$

where $R(\cdot)$ is the planar rotation matrix and ψ is defined as,

$$\psi := \cos^{-1}\left(\operatorname{dn}\left(\sqrt{c}\, \eta, k\right)\right) = \sin^{-1}\left(k \operatorname{sn}\left(\sqrt{c}\, \eta, k\right)\right) = \theta_0(\eta). \tag{3.29}$$

Proof. The proof is essentially the same to that of Proposition 3.2.2. Note the different definition of ψ in (3.29) ■

Case 3: $c = h$

This case is transitional between case 1 and case 2. Putting the modulus $k^2 = \frac{c}{h} = 1$ in either of the equations (3.17) or (3.25), we get the following solutions

$$\mu_1 = s_1\sqrt{c}\ \text{sech}\left(\sqrt{c}(t+\eta)\right), \tag{3.30a}$$

$$\mu_2 = s_2\sqrt{c}\ \tanh\left(\sqrt{c}(t+\eta)\right), \tag{3.30b}$$

$$\mu_3 = s_3\sqrt{c}\ \text{sech}\left(\sqrt{c}(t+\eta)\right), \tag{3.30c}$$

with $s_1, s_2, s_3 \in \{1, -1\}$ and $\eta \in \mathbb{R}$. We readily obtain the following result.

Proposition 3.2.5. *Let $c = h > 0$. Assume $\eta = 0$, then any extremal trajectory is given by,*

$$x(t) = s_2\left(1 - \text{sech}\left(\sqrt{c}\,t\right)\right), \tag{3.31a}$$

$$y(t) = s_1 s_2\left(\sqrt{c}\,t - \tanh\left(\sqrt{c}\,t\right)\right), \tag{3.31b}$$

$$\theta(t) = s_1 \tan^{-1}\left(\sinh\left(\sqrt{c}\,t\right)\right). \tag{3.31c}$$

Proof. Indeed, integrating $\dot{\theta} = u_1 = \mu_1$ yields (3.31c). Since $u_1 = \mu_2$, we get

$$\dot{x} = s_2\sqrt{c}\,\text{sech}\left(\sqrt{c}\,t\right)\tanh\left(\sqrt{c}\,t\right),$$

$$\dot{y} = s_1 s_2\sqrt{c}\tanh^2\left(\sqrt{c}\,t\right),$$

which in turn gives (3.31a)–(3.31b) after integration. ■

In the same spirit as before, we write any general extremal trajectories in terms of these trajectories.

Proposition 3.2.6. *Assume $c = h > 0$. Let us denote an extremal trajectory belonging to $\eta = 0$ case by $(x_0(t), y_0(t), \theta_0(t))$ according to (3.31). Then any extremal trajectory generated by (3.30) can be expressed as,*

$$\begin{bmatrix} x(t) \\ y(t) \end{bmatrix} = R(-\psi) \left(\begin{bmatrix} x_0(t+\eta) \\ y_0(t+\eta) \end{bmatrix} - \begin{bmatrix} x_0(\eta) \\ y_0(\eta) \end{bmatrix} \right), \tag{3.32}$$

$$\theta(t) = \theta_0(t+\eta) - \theta_0(\eta), \tag{3.33}$$

where $R(\cdot)$ is the planar rotation matrix and ψ is defined as,

$$\psi := s_1 \tan^{-1}\left(\sinh\left(\sqrt{c}\,\eta\right)\right) = \theta_0(\eta). \tag{3.34}$$

This case consists of two types of solutions: a straight line solution, corresponding to the subcase where the final condition lies on the x-axis, and an asymptotic solution, which asymptotically approaches a straight line with slope $\cot\psi$. See Fig. 3.2c for a graphic.

3.2.3 On Time-optimality

From an engineering perspective, it seems appealing to consider a similar problem where final time T is free. Therefore we want to reach from initial configuration g_0 to the final configuration g_T in a minimal time so that the control cost (u^2+v^2) is minimized along the optimal trajectory. It also makes sense to add a penalty

to the time it takes for the unicycle to complete the maneuver. The cost function can be expressed as

$$\min_{T,u(\cdot),v(\cdot)} \frac{1}{2}\int_0^T (a + u(t)^2 + v(t)^2)dt, \tag{3.35}$$

for some time-penalty parameter $a > 0$. Note that without the penalty on time, a solution could correspond to a prohibitively large final time which is not desired from a practical viewpoint. This time-optimal version is just a special case of what we have considered in section 3.2. To see this, we compute the Hamiltonian (3.11) as, $H = \frac{1}{2}(\mu_1^2 + \mu_2^2 - a)$. Since time-optimality requires the Hamiltonian to be identically zero, we have special case of $h = \mu_1^2 + \mu_2^2 = a$ (c.f. (3.15)). This also gives the bounds of the optimal controls $u_1 = \mu_1, u_2 = \mu_2$ to be within $\pm\sqrt{a}$. We can, therefore, use the parameter a to set a desired bound on the controls that is permitted by physical constraints. A closely related problem was studied in [Halder and Kalabic, 2017], where the speed control v was assumed to be of constant magnitude, and the minimum time problem associated with minimum curvature path was considered.

3.3 Optimal Control of a Collective of Agents

Now we consider a collective of N agents moving on the plane. Motion of each agent can be modeled by the unicycle dynamics (3.1). As seen before, this dynamics can be equivalently expressed as a controlled dynamics in SE(2), $\dot{g}_k = g_k\xi_k(u_k)$,

where

$$\xi_k(u_k) = u_{k1}X_1 + u_{k2}X_2, \quad k = 1, 2, ..., N. \tag{3.36}$$

We suppose these agents interact among themselves directed by a fixed adjacency matrix $A = [a_{ij}] \in \mathbb{R}^{N\times N}$. $a_{ij} = 1$ if agent i and agent j interact and $a_{ij} = 0$ otherwise. The nature of the interaction will be made precise shortly. Let D be the degree matrix, i.e. the diagonal matrix where the i-th diagonal entry represents the number of agents the i-th agent interact with. Then the graph Laplacian is defined by $B := D - A$. In this setup, we seek to minimize

$$\begin{aligned}\mathcal{L} &= \int_0^T L(\xi_1(u_1(t)), ..., \xi_N(u_N(t)))dt \\ &= \frac{1}{2}\int_0^T \left(\sum_{k=1}^N |\xi_k|^2 + \chi \sum_{k=1}^N \sum_{j=1}^N a_{kj} |\xi_k - \xi_j|^2\right) dt,\end{aligned} \tag{3.37}$$

for some constant $\chi \geq 0$ and the fixed endpoint conditions $g_k(0) = g_{k0}, g_k(T) = g_{kT}, k = 1, ..., N$. Note that we used the trace norm $|\xi| = \sqrt{\mathrm{tr}(\xi^\mathsf{T}\xi)}$. The parameter χ is called a coupling constant since it acts as a weight to the second term in the cost functional (3.37). Without the coupling term, this problem simplifies to solving N copies of the single agent problem as considered in Sec. 3.2. The coupling term penalizes agent k through the 'mismatch in control' with the agents that it is interacting with (i.e. nonzero entries of k-th row of the matrix A). This type of cost functional is aimed to capture the 'allelomimetic behavior' or the tendency to copy neighbors in a natural collective. [Justh and Krishnaprasad, 2015b] studies a very similar problem where the speeds of each agent is assumed to be constant. Here the speed controls $(u_{k2}, k = 1, 2, ..., N)$ are to be determined

by solving the optimal control problem (3.37).

Since the underlying optimal control problem is essentially the same, we will use the results from [Justh and Krishnaprasad, 2015b] to derive first order optimality conditions using the Pontryagin's Maximum Principle and the Lie-Poisson reduction technique. Denote $\mu_k \in \mathfrak{se}^*(2)$ by,

$$\mu_k = \sum_{i=1}^{3} \mu_{ki} X_i^\flat, \tag{3.38}$$

where $\{X_1^\flat, X_2^\flat, X_3^\flat\}$ is dual basis to $\{X_1, X_2, X_3\}$. If we define $\tilde{\mu}_k = \begin{bmatrix} \mu_{k1} & \mu_{k2} & \mu_{k3} \end{bmatrix}^\mathsf{T}$, first order optimality (PMP) yields

$$\begin{bmatrix} u_1 \\ \vdots \\ u_N \end{bmatrix} = \Psi \begin{bmatrix} \tilde{\mu}_1 \\ \vdots \\ \tilde{\mu}_N \end{bmatrix}, \tag{3.39}$$

where

$$\Psi = ((\mathbb{I}_N + 2\chi B) \otimes \mathbb{I}_2)^{-1} = (\mathbb{I}_N + 2\chi B)^{-1} \otimes \mathbb{I}_2. \tag{3.40}$$

Here $\otimes$ denotes the Kronecker product. The reduced Hamiltonian in $(\mathfrak{se}^*(2))^N$ takes the form

$$h = \frac{1}{2} \begin{bmatrix} \tilde{\mu}_1^\mathsf{T} & \cdots & \tilde{\mu}_N^\mathsf{T} \end{bmatrix} \Psi \begin{bmatrix} \tilde{\mu}_1 \\ \vdots \\ \tilde{\mu}_N \end{bmatrix}. \tag{3.41}$$

The Lie-Poisson reduced dynamics is then expressed as follows. Define $\boldsymbol{\mu} =$

$\begin{bmatrix} \mu_1^\mathsf{T} & \cdots & \mu_N^\mathsf{T} \end{bmatrix}^\mathsf{T}$. Then,

$$\dot{\boldsymbol{\mu}} = \Lambda(\boldsymbol{\mu})\nabla h, \tag{3.42}$$

where $\Lambda(\boldsymbol{\mu}) = -\text{diag}(\Omega_1, \cdots, \Omega_N)$, with

$$\Omega_k = \begin{bmatrix} 0 & \mu_{k3} & -\mu_{k2} \\ -\mu_{k3} & 0 & 0 \\ \mu_{k2} & 0 & 0 \end{bmatrix}, k = 1, ..., N. \tag{3.43}$$

Also we have $\nabla h = \begin{bmatrix} (\nabla h)_1 \cdots (\nabla h)_N \end{bmatrix}^\mathsf{T}$, $(\nabla h)_k = \begin{bmatrix} \frac{\partial h}{\partial \mu_{k1}} & \frac{\partial h}{\partial \mu_{k2}} & 0 \end{bmatrix}^\mathsf{T}$, $k = 1, ..., N$. Note that along with the Hamiltonian (3.41), there are N Casimirs which are constants of motion. The Casimirs are defined as,

$$c_k = \mu_{k2}^2 + \mu_{k3}^2. \tag{3.44}$$

In both the extreme cases (i) no coupling ($\chi = 0$) and (ii) high coupling ($\chi \to \infty$), the collective optimal problem simplifies to studying the single agent problem as considered in Section 3.2. The $\chi = 0$ case is immediate. The details of the high coupling limit $\chi \to \infty$ is worked out in [Justh and Krishnaprasad, 2015b] (see section 3(c)). Defining the quantities

$$\alpha_1 = \frac{1}{N}\sum_{j=1}^{N} \mu_{j1}, \quad \alpha_2 = \frac{1}{N}\sum_{j=1}^{N} \mu_{j2}, \quad \alpha_3 = \frac{1}{N}\sum_{j=1}^{N} \mu_{j3}, \tag{3.45}$$

we obtain the following differential equations

$$\begin{aligned} \dot{\alpha}_1 &= -\alpha_2\alpha_3, \\ \dot{\alpha}_2 &= \alpha_1\alpha_3, \\ \dot{\alpha}_3 &= -\alpha_1\alpha_2. \end{aligned} \tag{3.46}$$

These are the same equations we already obtained and analyzed in details for a single agent case (3.13).

3.4 Concluding Remarks

In this chapter, we studied an optimal control problem of a unicycle on the plane in detail. First order necessary conditions are obtained by using the Pontryagin's Maximum Principle and the Lie-Poisson reduction technique. All possible motion types are properly categorized by the relative values of the Casimir and the Hamiltonian. In the later part, we presented a framework for studying a class of optimal control problems involving many agents. These agents interact with each other by a pre-determined interaction graph. The interaction enters into the optimal controls of the agents through the additive 'control-mismatch' term in cost functional. This type of cost has been used in literature [Justh and Krishnaprasad, 2015a,b] to capture the 'allelomimetic behavior' in natural flocks. The single agent case, considered in this chapter, emerges naturally in a synchronization limit of the collective model. This collective framework gives us the starting point to conceptualize a continuum flock where we study the limiting case of $N \to \infty$ under a specific interaction graph. These topics are described in detail in later chapters of this thesis.

Part II

Analysis of Collective Motion:

Top-down Approaches

Chapter 4

Continuum Flocking and Control

4.1 Motivation

It is a common practice in classical mechanics to consider a continuous description of a physical system. Applications include vibrating rods, vibrating membranes, fluid mechanics etc. [Goldstein et al., 2001; Chorin et al., 1990] The transition from discrete-particle system to a continuum enables a compact description of the system, often leading to partial differential equations that reveal deep insights into the system, e.g. wave-like phenomena, which may be too obscure or inelegant in the discrete counterpart. In the same spirit, we attempt to conceptualize a continuum flock and address its optimal maneuvering properties. Biological flocks are known to show remarkable response to predator attacks. In the case of an attack, the whole flock seems to divert away from the predator. They can perform these tasks my means of propagating information (in this case, threat) through the flock at a much higher speed than the flocking speed [Attanasi et al., 2014].

A key goal of our approach is to capture this phenomenon, i.e. to uncover the wave-like aspects of flocking. An optimal control problem for a flock of finite agents is presented in Section 3.3. We take the same framework and formulate a general continuum version of the problem.

Consider an ensemble of N identical, self-steering particles, each obeying a drift free left invariant system on a matrix Lie group G,

$$\dot{g}_i = g_i \xi_i, \quad g_i \in G, \ \xi_i \in \mathfrak{g}, \quad i = 1, ..., N, \tag{4.1}$$

where $\mathfrak{g}$ is the Lie algebra of G. These particles interact with each other by a pre-defined graph of interaction. The collective behavior of such a system was extensively studied in [Justh and Krishnaprasad, 2015b] by solving an appropriate optimal control problem. Borrowing the notations of [Justh and Krishnaprasad, 2015b], we write the cost functional as "self-energy" term coupled with a "mismatch in steering" term

$$J = \int_0^T L(\xi_1(t), ..., \xi_N(t)) dt, \tag{4.2}$$

where,

$$L(\xi_1, ..., \xi_N) = \frac{1}{2} \left(\sum_{i=1}^{N} \|\xi_i\|^2 + \chi \sum_{i=1}^{N} \sum_{j=1}^{N} a_{ij} \|\xi_i - \xi_j\|^2 \right), \tag{4.3}$$

where binary valued a_{ij}'s populate the adjacency matrix that defines the graph of interaction and $\chi \geq 0$ is a coupling constant. Note that the inner product $\langle \xi, \eta \rangle = \mathrm{tr}(\xi^T \eta)$, and the corresponding trace norm, $\|\xi\| = \sqrt{\langle \xi, \xi \rangle}$ are in effect, where $\xi, \eta \in \mathfrak{g}$.

In an attempt to extend this view, we consider an infinite number of particles, i.e. the limiting case of $N \to \infty$. Here we consider a one-dimensional continuum of particles, i.e. each particle is labeled by a point on a circle S^1. This way, the agents are thought as a *virtual filament*. Moreover, we consider a cyclic interaction graph, i.e. each particle is thought to be interacting with the 'next' particle on the circle. We introduce the maps, $g : \mathbb{R} \times S^1 \to G$ and $\xi : \mathbb{R} \times S^1 \to \mathfrak{g}$. The mismatch in steering term can then be written as the gradient of ξ in the limiting case. In other words, in continuum limit of $N \to \infty$, the Lagrangian in (4.3) take the form,

$$L(\xi) = \frac{1}{2} \int_0^{2\pi} \left(\|\xi(t,\theta)\|^2 + \chi \left\| \frac{\partial \xi(t,\theta)}{\partial \theta} \right\|^2 \right) d\theta. \tag{4.4}$$

Note that the summations over the number of particles in (4.3) have been replaced by integral over the circle in the continuum setting in (4.4).

Let n be the dimension of the Lie algebra $\mathfrak{g}$ and $\{A_1, A_2, ..., A_n\}$ denote an orthonormal basis of $\mathfrak{g}$. We introduce the controls $u_i : \mathbb{R} \times S^1 \to \mathbb{R}, i = 1, ..., m$, so that ξ can be written as,

$$\xi(t,\theta) = \sum_{i=1}^{m} u_i(t,\theta) A_i, \tag{4.5}$$

where $m < n$. With this substitution, the Lagrangian in (4.4) can be rewritten as,

$$L(u_1, ..., u_m) = \frac{1}{2} \int_0^{2\pi} \sum_{i=1}^{m} \left(u_i^2 + \chi \left(\frac{\partial u_i}{\partial \theta} \right)^2 \right) d\theta. \tag{4.6}$$

Finally, we attempt to minimize the cost functional,

$$J = \int_0^T L(u_1, ..., u_m)dt, \tag{4.7}$$

subject to the group dynamics, $\frac{\partial g(t,\theta)}{\partial t} = g(t,\theta)\xi(t,\theta) = g(t,\theta)\left(\sum_{i=1}^{m} u_i(t,\theta)A_i\right)$ and the fixed end-point constraints, $g(0,\theta) = g_0(\theta)$ and $g(T,\theta) = g_T(\theta)$.

We will note that this optimal control problem can be cast in a more convenient setting of loop groups, the group of smooth functions from the circle to the Lie group G. In Section 4.2, we will develop a general framework for such optimal control problems in loop group setting. Controllability results will be discussed in Section 4.3. This helps us to describe optimal control solutions in Section 4.4. Necessary conditions will be derived by both calculus of variations and Pontryagin's Maximum Principle approach. An example of continuum of nonholonomic integrators will be studied in detail in Section 4.5. Section 4.6 will present derivation of optimal control equations in the SE(2) case along with their numerical treatment. This is a joint work with Dr. E. Justh [Halder et al., 2019a].

4.2 A Control System on a Loop Group

Let G be a finite dimensional matrix Lie group and $\mathfrak{g}$ be its Lie algebra of dimension n. We will study spaces of smooth maps from the circle S^1 to G and $\mathfrak{g}$,

$$\mathscr{G} = C^\infty(S^1; G), \quad \mathscr{L} = C^\infty(S^1; \mathfrak{g}).$$

We can construct Sobolev completions of $\mathscr{G}$ and $\mathscr{L}$ as done in [Krishnaprasad et al., 1983]. We can always view the Lie algebra $\mathfrak{g}$ as a subalgebra of the general linear algebra $\mathrm{gl}(r,\mathbb{R})$ for some $r > n$. Defining the space $\mathscr{R} = C^\infty(S^1; \mathrm{gl}(r,\mathbb{R}))$, we have

$$\mathscr{G} \subset \mathscr{R}, \quad \mathscr{L} \subset \mathscr{R}.$$

For any $f \in \mathscr{R}$, use the Sobolev k-norm ($k \geq 1$)

$$\|f\|_k = \int_{S^1} \sum_{l=0}^{k} \left| \frac{d^l}{d\theta^l} f(\theta) \right|^2 d\theta, \tag{4.8}$$

where

$$|f|^2 = \mathrm{tr}(f^{\mathrm{T}} f).$$

Let the completions of $\mathscr{G}$, $\mathscr{L}$, and $\mathscr{R}$ in this norm be denoted as $\mathscr{G}_k$, $\mathscr{L}_k$, and $\mathscr{R}_k$, respectively. By Proposition 3.1 of [Krishnaprasad et al., 1983], $\mathscr{G}_k$ is actually a Lie group under pointwise multiplication operation $(g_1 g_2)(\theta) = g_1(\theta) \cdot g_2(\theta), \quad g_1, g_2 \in \mathscr{G}_k, \theta \in S^1$. Moreover, $\mathscr{L}_k$ is the Lie algebra of $\mathscr{G}_k$ under pointwise Lie bracket defined as $[f_1, f_2](\theta) = [f_1(\theta), f_2(\theta)], \quad f_1, f_2 \in \mathscr{L}_k, \theta \in S^1$. The spaces $\mathscr{G}_k$ and $\mathscr{L}_k$ are called loop groups and loop algebras [Pressley and Segal, 1986].

Similar to the finite dimensional Lie groups, we introduce (pointwise) left action by $L_g : \mathscr{G}_k \to \mathscr{G}_k, h \mapsto gh$, the left translation by $g \in \mathscr{G}_k$. The tangent map of L_g is then given as $T_h L_g : T_h \mathscr{G}_k \to T_{gh} \mathscr{G}_k$. We now define a left invariant vector field on $\mathscr{G}_k$ as follows. A vector field $X : \mathscr{G}_k \to T\mathscr{G}_k, h \mapsto X(h)$ is called left invariant if

$$T_h L_g(X(h)) = X(gh), \quad \forall h \in \mathscr{G}_k. \tag{4.9}$$

Recognizing the Lie algebra $\mathscr{L}_k$ as the tangent space at identity e of $\mathscr{G}_k$ ($e = \{f \in \mathscr{G}_k | f(\theta) \equiv e_G\}$, where e_G is the identity element of G), i.e. $\mathscr{L}_k = T_e\mathscr{G}_k$, we can define a left invariant control system as,

$$\frac{dg(t)}{dt} = T_e L_{g(t)}(\xi(t)) = g(t) \cdot \xi_{u(t)}, \tag{4.10}$$

where a given control input $u(t)$ determines a controlled vector $\xi_{u(t)}$ in the Lie algebra $\mathscr{L}_k$. Note that the loop algebra $\mathscr{L}_k$ can be identified with the tensor product space $\mathfrak{g} \otimes F$, where F is the ring of real valued C^∞ functions on S^1. Choose a basis of $\mathfrak{g}$ as $\{A_1, A_2, \ldots A_n\}$. Then, any $\xi \in \mathscr{L}_k$ can be written as,

$$\xi(\theta) = \xi_1(\theta)A_1 + \cdots + \xi_n(\theta)A_n, \quad \theta \in S^1,$$

where each of ξ_k's ($k = 1, \ldots, n$) are smooth functions on the circle. We will now limit ourselves to the study of control vectors ξ_u of the form,

$$\xi_{u(t)} = u_1(t)A_1 + \cdots + u_m(t)A_m, \tag{4.11}$$

where $m < n$ and the control input $u(\cdot) = (u_1(\cdot), \ldots, u_m(\cdot))$ belongs to the set $\mathcal{U}$ of piecewise continuous U valued functions, where U is vector space of $\mathbb{R}^m$ valued smooth functions on the circle, i.e. $\mathcal{U} := \{u(\cdot) : u \text{ is piecewise continuous in } t, u(t) \in U = C^\infty(S^1; \mathbb{R}^m)\}$.

4.3 Controllability

Having constructed the control system on the loop group $\mathscr{G}_k$, it is natural to ask the question of controllability or accessibility, i.e. given any two points g_1 and

g_2 in $\mathscr{G}_k$, if they can be connected by a piecewise differentiable curve, consisting of possibly finitely many pieces, each piece being an integral curve of a left invariant vector field defined by choosing a control $u(\cdot) \in \mathcal{U}$. In finite dimensional analogue of this question, i.e. where we shrink the circle S^1 down to a point, the controllability question is answered by the well known Chow-Rashevsky theorem [Wei-Liang, 1939; Rashevsky, 1938]. In infinite dimensional cases, however, it is not immediate if the Chow-Rashevsky theorem remains valid. There is a body of literature [Heintze and Liu, 1999; Salehani and Markina, 2014] that attempts to attack this problem. It is the result of [Heintze and Liu, 1999] that we use in this section. This result addresses the controllability question in a weaker sense which we will make explicit.

Let $\mathcal{M}$ be a complete connected Hilbert manifold and let $\mathfrak{X}(\mathcal{M})$ denote the set of all smooth vector fields defined on $\mathcal{M}$. Let $\mathcal{F} \subset \mathfrak{X}(\mathcal{M})$ be a given family of smooth vector fields on $\mathcal{M}$. Let $\mathcal{R}_{\mathcal{F}}(x)$ be the set of points in $\mathcal{M}$ that can be joined from $x \in \mathcal{M}$ by means of a piecewise differentiable curve, each piece of which is an integral curve of a vector field in $\mathcal{F}$. Let Lie $\mathcal{F}$ be the Lie subalgebra of $\mathfrak{X}(\mathcal{M})$ generated by $\mathcal{F}$, and $\text{Lie}_x\ \mathcal{F} = \{X(x)\ : X \in \text{Lie}\ \mathcal{F}\}$ - the evaluation of Lie $\mathcal{F}$ at $x \in \mathcal{M}$. If $\mathcal{M}$ is finite dimensional, the classical Chow-Rashevsky theorem holds: if $\text{Lie}_x\ \mathcal{F} = T_x\mathcal{M}$ for each $x \in \mathcal{M}$, then $\mathcal{R}_{\mathcal{F}}(x) = \mathcal{M}$, for every $x \in \mathcal{M}$. In a general Hilbert manifold $\mathcal{M}$, the following generalized Chow-Rashevsky theorem holds:

Theorem 4.3.1 ([Heintze and Liu, 1999]). *Let $\mathcal{M}$ be a complete connected Hilbert manifold and $\mathcal{F}$ a family of smooth vector fields defined on $\mathcal{M}$. If $Lie_x\ \mathcal{F}$ is dense in $T_x\mathcal{M}$ for all $x \in \mathcal{M}$, then $\mathcal{R}_{\mathcal{F}}(x)$ is dense in $\mathcal{M}$ for all $x \in \mathcal{M}$.*

Theorem 4.3.1 is a weaker statement than the one for finite dimensional case. Here we make precise the strong and weak notions of controllability. Consider the control system constructed in (4.10)–(4.11). Note that the loop group $\mathscr{G}_k$ can be given a structure of a smooth Hilbert manifold [Eells Jr, 1966; Ebin and Marsden, 1970]. In this case, the family $\mathcal{F} \in \mathfrak{X}(\mathscr{G}_k)$ is given by $\{X_i\}_{i=1}^m$, where $X_i(g(t)) = g(t) \cdot (u_i(t)A_i)$, for $g(t) \in \mathscr{G}_k$.

Definition 4.1. (**Strong Controllability**) The control system (4.10)–(4.11) is said to be *strongly controllable* if $\mathcal{R}_{\mathcal{F}} = \mathscr{G}_k$, i.e. given any two points $g_1, g_2 \in \mathscr{G}_k$, we can find a control input that will transfer the system from g_1 to g_2.

Definition 4.2. (**Weak Controllability**) The control system (4.10)–(4.11) is said to be *weakly controllable* if $\mathcal{R}_{\mathcal{F}}$ is dense in $\mathscr{G}_k$, i.e. given any two points $g_1, g_2 \in \mathscr{G}_k$, we can find a control input that will transfer the system from g_1 to a state that is arbitrarily close to g_2.

The set $\{A_1, ..., A_m\}$ is said to be *bracket generating* if the iterated brackets of its elements span the Lie algebra $\mathfrak{g}$. In the finite dimensional analogue of the control system defined in (4.10)–(4.11), the (strong) controllability condition according to Chow-Rashevsky theorem is equivalent to having the set $\{A_l\}_{l=1}^m$ bracket generating in $\mathfrak{g}$. We will now try to establish (weak) controllability of

the infinite dimensional loop group case by assuming that $\{A_1, ..., A_m\}$ is bracket generating in $\mathfrak{g}$.

Theorem 4.3.2. *Consider the control system (4.10)–(4.11) on the loop group $\mathscr{G}_k$. Assume that the set $\{A_l\}_{l=1}^m$ is bracket generating in $\mathfrak{g}$. Then the system is weakly controllable.*

Proof. The definition of left invariant vector fields on $\mathscr{G}_k$ (4.9) can also be made explicit by means of smooth functions on $\mathscr{G}_k$. Let $\mathcal{D}$ be the set of smooth real valued functions on $\mathscr{G}_k$. Then given an element $\xi \in \mathscr{L}_k$, we can define a differentiable vector field $X_\xi : \mathcal{D} \to \mathcal{D}$ as,

$$(X_\xi f)(g) = (Df)_g \cdot g\xi, \quad f \in \mathcal{D}, \tag{4.12}$$

where D denotes the differential operator. Given two vector fields $X_\xi, X_\eta \in \mathfrak{X}(\mathscr{G}_k)$, we can calculate their Jacobi-Lie bracket defined as,

$$[X_\xi, X_\eta]f = X_\xi(X_\eta f) - X_\eta(X_\xi f), \quad f \in \mathcal{D}.$$

We compute,

$$\begin{aligned} X_\xi(X_\eta f)(g) &= (X_\xi((Df)_g \cdot g\eta))(g) \\ &= D((Df)_g \cdot g\eta)_g \cdot g\xi \\ &= (D^2 f)_g \cdot (g\eta, g\xi) + (Df)_g \cdot (D(g\eta)_g \cdot g\xi) \\ &= (D^2 f)_g \cdot (g\eta, g\xi) + (Df)_g \cdot (g\xi\eta). \end{aligned}$$

Similarly,

$$X_\eta(X_\xi f)(g) = (D^2 f)_g \cdot (g\xi, g\eta) + (Df)_g \cdot (g\eta\xi).$$

The symmetry of the second differential operator D^2 yields

$$[X_\xi, X_\eta]f(g) = (Df)_g \cdot (g(\xi\eta - \eta\xi))$$

$$= X_{[\xi,\eta]}f(g),$$

where $[\xi, \eta]$ is the usual (pointwise) Lie bracket on $\mathscr{L}_k$. This leads us to a detailed study of the Lie bracket of the loop algebra $\mathscr{L}_k$. It is immediate that $\mathscr{L}_k$ is generated by the generators $\{P_r^{m_r}\}_{m_r\in\mathbb{Z},\ r\in\{1,\dots,n\}}$ defined as,

$$P_r^{m_r} = e^{\mathrm{i}m_r\theta}A_r. \tag{4.13}$$

Let the structure constants of $\mathfrak{g}$ be denoted by Γ_{pq}^r. Then,

$$[P_p^{m_p}, P_q^{m_q}] = \sum_{r=1}^{n} \Gamma_{pq}^r P_r^{m_p+m_q}. \tag{4.14}$$

With this notation, a controlled vector $\xi(t) = \xi_{u(t)} \in \mathscr{L}_k$ can be expressed as

$$\xi_{u(t)} = \sum_{r=1}^{m} \left(\sum_{m_r\in\mathbb{Z}} u_r^{m_r}(t) P_r^{m_r} \right), \tag{4.15}$$

where for each $r = 1, \dots, m$, $u_r^{m_r}(t) \in \mathbb{C}$'s are the Fourier coefficients of the control $u_r(t)$ and $\overline{u_r^{m_r}}(t) = u_r^{-m_r}(t)$ (since the controls are real). We now define a family of vector fields on $\mathscr{G}_k$ as $\mathcal{F} = \{X_r^{m_r}\}_{m_r\in\mathbb{Z},\ r\in\{1,\dots,m\}}$, where

$$X_r^{m_r} f(g) = (Df)_g \cdot gP_r^{m_r}, \quad f \in \mathcal{D}.$$

Taking bracket of any two vector fields from the family $\mathcal{F}$ yields another vector filed which is governed by the commutator relationship in (4.14). Note that since the set $\{A_1, \dots, A_m\}$ is bracket generating in $\mathfrak{g}$, for each $l \in \{m+1, \dots, n\}$, we are guaranteed to get the item

$$P_l^{m_l} := P_l^{\sum_r a_r m_r}, \quad a_r \in \mathbb{Z}^+ \cup \{0\}, m_r \in \mathbb{Z}, r \in \{1, \dots, m\},$$

at some depth of iterated brackets from the family $\mathcal{F}$. By choosing $m_r \in \mathbb{Z}, r \in \{1, \ldots, m\}$, we can then achieve any $m_l \in \mathbb{Z}$. We have thus proved that if the set $\{A_r\}_{r\in\{1,\ldots,m\}}$ is bracket generating in $\mathfrak{g}$, $\text{Lie}_g\ \mathcal{F}$ is dense in the tangent space $T_g\mathscr{G}_k$ at each $g \in \mathscr{G}_k$. The generalized Chow's theorem 4.3.1 then provides the required (weak) controllability result. ■

4.4 Optimal Control Problems

We start with the left invariant control system on the loop group $\mathscr{G}_k$ as in (4.10)-(4.11). Now for a given $T > 0$, consider the following fixed end-point optimal control problem,

$$(\mathrm{P}_G) \qquad \begin{aligned} &\min_{u\in\mathcal{U}} J(u) = \int_0^T L(g(t), u(t))dt \\ &\text{subject to:} \quad \dot{g} = g \cdot \xi, \quad g(0) = g_0, g(T) = g_T;\ g_0, g_T \in \mathscr{G}_k. \end{aligned} \tag{4.16}$$

We are interested in deriving necessary conditions for optimality for such optimal control problems. Special care needs to be taken since the problem is posed in an infinite dimensional setting. We provide two different approaches for doing that.

4.4.1 Calculus of Variations Approach

Let $x(t) = (x_1(t), ..., x_r(t)) \in C^\infty(S^1, \mathbb{R}^r) =: X$ denote a vector that can be used to represent the components of $g(t) \in G$, for some $r \geq n$. The group dynamics $\dot{g} = g \cdot \xi(u) = g \cdot (\sum_i u_i A_i)$ effectively lets us write the control $u(t)$ as a function of $(x(t), \dot{x}(t))$. The fixed endpoint constraints in g can be translated to some

nonholonomic constraints of the form

$$\Phi(x, \dot{x}) = \int_0^T \phi(x(t), \dot{x}(t))dt = 0, \tag{4.17}$$

where $\phi(x(t), \dot{x}(t)) \in C^\infty(S^1, \mathbb{R}^l) =: Z$, for some $l < r$. Then the problem (P_G) can be written as,

$$\min J = \int_0^T L(x(t), \dot{x}(t))dt, \tag{4.18}$$

subject to the nonholonomic constraints (4.17). Here we have to keep in mind that the variations in x are to be both in t and θ. This is a well known problem called the 'Lagrange problem' in calculus of variations. The one-dimensional Lagrange problem is well studied [Gelfand and Fomin, 1963; Elsgolc, 2012]. However, the theory behind multidimensional problem is more complicated and less complete [Giaquinta and Hildebrandt, 1996; Bliss, 1946]. The difficulty arises since not all the $\dot{x}$ are freely variable. According to [Giaquinta and Hildebrandt, 1996, p. 112], there exist a Lagrange multiplier $\lambda \in C^\infty(\mathbb{R} \times S^1; \mathbb{R}^l)$, such that we can find the free extremals of the augmented Lagrangian in an usual way. Moreover, since the constraints (4.17) are of isoperimetric type, λ does not depend on t [Rund, 1966, p. 349]. We can write the augmented Lagrangian as

$$\tilde{L} = L + \langle \lambda, \phi \rangle_Z \,, \tag{4.19}$$

where $\lambda = (\lambda_1, \lambda_2, ..., \lambda_l) \in C^\infty(S^1; R^l)$.

Furthermore, we are interested in a special structure of the Lagrangian, namely

$$L(x, \dot{x}) = \int_0^{2\pi} \mathcal{L}(x, \dot{x})\ d\theta, \tag{4.20}$$

where the functional $\mathcal{L}$ is called the Lagrangian density. The augmented cost function take the form,

$$\begin{aligned}\tilde{J}(x,\dot{x}) &= \int_0^T \int_0^{2\pi} \mathcal{L}(x,\dot{x})\ d\theta dt + \sum_{j=1}^{l} \int_0^{2\pi} \lambda_j(\theta)\phi_j(x,\dot{x})\ d\theta \\ &= \int_0^T \int_0^{2\pi} \tilde{\mathcal{L}}(x,\dot{x})\ d\theta dt,\end{aligned}$$

where the redefined Lagrangian density is given by,

$$\tilde{\mathcal{L}} = \mathcal{L} + \sum_{j=1}^{l} \lambda_j \phi_j. \tag{4.21}$$

We will relabel $\tilde{\mathcal{L}}$ by $\mathcal{L}$ in subsequent analysis for convenience. By invoking notations $x_t = \frac{\partial x}{\partial t}$, $x_\theta = \frac{\partial x}{\partial \theta}$, $x_{t\theta} = \frac{\partial^2 x}{\partial t \partial \theta} = x_{\theta t}$ etc., we can write $\mathcal{L} = \mathcal{L}(x, x_\theta, x_t, x_{t\theta})$. In order to optimize this cost functional, the variational principle requires that,

$$\delta\tilde{J} = \int_0^T \int_0^{2\pi} \sum_{i=1}^{r} \left(\frac{\partial \mathcal{L}}{\partial x_i}\delta x_i + \frac{\partial \mathcal{L}}{\partial x_{i,\theta}}\delta x_{i,\theta} + \frac{\partial \mathcal{L}}{\partial x_{i,t}}\delta x_{i,t} + \frac{\partial \mathcal{L}}{\partial x_{i,t\theta}}\delta x_{i,t\theta} \right) d\theta dt = 0,$$

where δy denotes variation of the quantity y that vanishes at the endpoints of t and θ. Using integration by parts, for each i, we may write,

$$\begin{aligned}\int_0^{2\pi} \frac{\partial \mathcal{L}}{\partial x_{i,\theta}}\delta x_{i,\theta} d\theta &= \frac{\partial \mathcal{L}}{\partial x_{i,\theta}}\delta x_i \Big|_0^{2\pi} - \int_0^{2\pi} \frac{\partial}{\partial \theta}\left(\frac{\partial \mathcal{L}}{\partial x_{i,\theta}}\right)\delta x_i d\theta \\ &= -\int_0^{2\pi} \frac{\partial}{\partial \theta}\left(\frac{\partial \mathcal{L}}{\partial x_{i,\theta}}\right)\delta x_i d\theta,\end{aligned}$$

Similarly,

$$\begin{aligned}\int_0^T \frac{\partial \mathcal{L}}{\partial x_{i,t}}\delta x_{i,t} dt &= -\int_0^T \frac{\partial}{\partial t}\left(\frac{\partial \mathcal{L}}{\partial x_{i,t}}\right)\delta x_i dt, \\ \int_0^T \int_0^{2\pi} \frac{\partial \mathcal{L}}{\partial x_{i,t\theta}}\delta x_{i,t\theta} d\theta dt &= \int_0^T \int_0^{2\pi} \frac{\partial^2}{\partial t \partial \theta}\left(\frac{\partial \mathcal{L}}{\partial x_{i,t\theta}}\right)\delta x_i\ d\theta dt.\end{aligned}$$

Hence,

$$\delta\tilde{J} = \int_0^T \int_0^{2\pi} \sum_i \left(\frac{\partial \mathcal{L}}{\partial x_i} - \frac{\partial}{\partial \theta}\left(\frac{\partial \mathcal{L}}{\partial x_{i,\theta}}\right) - \frac{\partial}{\partial t}\left(\frac{\partial \mathcal{L}}{\partial x_{i,t}}\right) + \frac{\partial^2}{\partial t \partial \theta}\left(\frac{\partial \mathcal{L}}{\partial x_{i,t\theta}}\right)\right) \delta x_i \, d\theta dt$$

The Euler-Lagrange equations can then be expressed as,

$$\frac{\partial \mathcal{L}}{\partial x_i} - \frac{\partial}{\partial \theta}\left(\frac{\partial \mathcal{L}}{\partial x_{i,\theta}}\right) - \frac{\partial}{\partial t}\left(\frac{\partial \mathcal{L}}{\partial x_{i,t}}\right) + \frac{\partial^2}{\partial t \partial \theta}\left(\frac{\partial \mathcal{L}}{\partial x_{i,t\theta}}\right) = 0, \quad i = 1, 2, ..., r. \tag{4.22}$$

4.4.2 Maximum Principle Approach

In this section we provide a brief exposure to Pontryagin's Maximum Principle (PMP) type argument in infinite dimensional spaces. It is to be noted that PMP does not automatically hold in general infinite dimensional optimal control problems, one requires some more assumptions for it to work. A detailed study on this subject is done in Appendix A. Here we only define some notations and assumptions to state the necessary theorem.

We consider an abstract differential equation in a Hilbert space X,

$$\frac{dx(t)}{dt} = f(t, x(t), u(t)) \quad \text{a.e. in } [0, T], \tag{4.23}$$

where $x(t) \in X$, $u(\cdot) \in \mathcal{U}$, and $T > 0$. Here X is called the state space and $\mathcal{U}$ is the set of all measurable functions $u(\cdot) : [0, T] \to U$, where U is a separable metric space called the control space. With this setup, we formulate the following optimal control problem (P),

$$\text{(P)} \qquad \begin{aligned} &\min_{u \in \mathcal{U}} J(u) = \int_0^T L(t, x(t), u(t)) dt \\ &\text{subject to:} \quad \dot{x} = f(t, x, u) \ \text{ a.e. in } [0, T], \quad x(0) = x_0, x(T) = x_T. \end{aligned} \tag{4.24}$$

We assume that both the functions $f(\cdot,\cdot,\cdot)$ and $L(\cdot,\cdot,\cdot)$ are Bochner integrable in $t \in [0,T]$ and Lipschitz continuous in $x(t) \in X$, with constant K. Furthermore, we require the existence and continuity of the Fréchet derivatives $f'_x(t,x,u)$ and $L'_x(t,x,u)$. We also assume the functions f, L and their derivatives f'_x, L'_x to be bounded, i.e. there exists an $M > 0$, such that

$$\|f(t,x,u)\| \leq M, \quad \|f'_x(t,x,u)\| \leq M,$$

$$\|L(t,x,u)\| \leq M, \quad \|L'_x(t,x,u)\| \leq M,$$

for all $(t, x(t), u(t)) \in [0,T] \times X \times U$. Note that these hypotheses ensure a continuous and unique solution of (4.23) to exist [Avez, 1986]. The following technical details is one of the key ingredients in the proof of the PMP.

Definition 4.3. (**Finite Codimensionality**) [Fattorini, 1987] A subset S of a Hilbert space Z is called to be *finite codimensional* in Z, if there exists a closed subspace $Z_c \subseteq Z$ of finite codimension such that $S_c = \Pi_c(\overline{\text{co}}(S))$, has nonempty interior in Z_c, where Π_c denotes the orthogonal projection from Z onto Z_c and $\overline{\text{co}}$ means closed convex hull.

We will now make a key assumption to derive a nontrivial maximum principle. Let a solution of problem (P) exist and the optimal control be denoted by $u^* \in \mathcal{U}$ and let the corresponding optimal trajectory be denoted as $x^*(\cdot)$. Then define the 'reachable set' as,

$$\begin{aligned}\mathsf{R} := \Bigg\{ z(T) \in X \mid z(t) = &\int_0^t f'_x(s, x^*(s), u^*(s)) \cdot z(s) ds \\ &+ \int_0^t \left(f(s, x^*(s), v(s)) - f(s, x^*(s), u^*(s))\right) ds, \text{ for some } v(\cdot) \in \mathcal{U} \Bigg\} \quad (4.25)\end{aligned}$$

(**A1**) The set R is finite codimensional in X.

Remark 4.1. In general, it is not clear whether there exists a relationship between controllability (strong or weak) of the system and the finite codimensionality assumption of the 'reachable set' R. We will, however, prove that in a special case of $G = \mathrm{H}(3)$, the Heisenberg group, the strong controllability implies finite codimensionality of R. It is of future consideration to address this question in a general case.

Using usual formalism, we invoke the *pre-Hamiltonian* function $H : \mathbb{R} \times X \times U \times \mathbb{R} \times X^* \to \mathbb{R}$ as,

$$H(t, x(t), u(t), p_0, p(t)) = p_0 L(t, x(t), u(t)) + \langle p(t), f(t, x(t), u(t)) \rangle \,, \tag{4.26}$$

where $p(t) \in X^*$ is called the costate variable. Then the PMP can be written as,

Theorem 4.4.1. ***(Maximum Principle)*** *Let $u^* \in \mathcal{U}$ be an optimal control for problem (P) and $x^*(t)$ be the corresponding optimal trajectory. Then, there exist a pair $(p_0^*, p^*(t)) \in \mathbb{R} \times X^*, t \in [0, T]$, such that $(p_0^*, p^*) \not\equiv (0, 0)$, $p_0^* \leq 0$, $p^*(\cdot)$ satisfies the differential equation,*

$$\dot{p}^*(t) = -\left(f_x'(t, x^*(t), u^*(t))^\star \, p^*(t) - p_0^* L_x'(t, x^*(t), u^*(t)\right), \tag{4.27}$$

where by $\mathcal{A}^\star$ we denote the adjoint operator of the operator $\mathcal{A}$. The pointwise maximization of the pre-Hamiltonian holds,

$$H(t, x^*(t), u^*(t), p_0^*, p^*(t)) = \max_{v \in U} H(t, x^*(t), v, p_0^*, p^*(t)), \tag{4.28}$$

for a.e. $t \in [0,T]$. *Moreover,* x^* *and* p^* *satisfy Hamilton's canonical equations, i.e.*

$$\frac{dx^*}{dt} = \frac{\delta H}{\delta p^*}(t, x^*, u^*, p_0^*, p^*) \tag{4.29}$$

$$\frac{dp^*}{dt} = -\frac{\delta H}{\delta x^*}(t, x^*, u^*, p_0^*, p^*). \tag{4.30}$$

A proof of this theorem is rather complicated and is given in Appendix A. We now use this result to state a maximum principle for the loop group case.

Theorem 4.4.2. ***(Maximum Principle in loop group setting)*** *Let* $u^* \in \mathcal{U}$ *be an optimal control for problem* (P_G) *and* $g^*(t)$ *be the corresponding optimal trajectory. Assume the finite codimensionality condition* (***A1***). *Denote* $\mathscr{R}_k$, *the Hilbert space of* k*-Sobolev completion of the space* $\mathscr{R} = C^\infty(S^1, \mathrm{gl}(r, \mathbb{R}))$, *for some* $r > n$. *Then, there exist a pair* $(p_0^*, p^*(t)) \in \mathbb{R} \times \mathscr{R}_k, t \in [0,T]$, *such that* $(p_0^*, p^*) \not\equiv (0,0), p_0^* \leq 0$, $p^*(\cdot)$ *satisfies the differential equation*

$$\dot{p}^*(t) = -p^*(t) \cdot \xi(u^*(t))^{\mathsf{T}}, \tag{4.31}$$

and the pointwise maximization of the pre-Hamiltonian holds,

$$H(g^*(t), u^*(t), p_0^*, p^*(t)) = \max_{v \in U} H(g^*(t), v, p_0^*, p^*(t)), \tag{4.32}$$

for a.e. $t \in [0,T]$. *Moreover,* g^* *and* p^* *satisfy Hamilton's equations, i.e.*

$$\begin{aligned} \frac{dg^*}{dt} &= \frac{\delta H}{\delta p^*}(g^*, u^*, p_0^*, p^*) \\ \frac{dp^*}{dt} &= -\frac{\delta H}{\delta g^*}(g^*, u^*, p_0^*, p^*). \end{aligned} \tag{4.33}$$

Proof. It is almost immediate that under a finite codimensionality assumption like (**A1**), we can state a maximum principle like Theorem 4.4.1 for problem (P_G). The

only caveat is that the state space $\mathscr{G}_k$ is not a Hilbert space and hence Theorem 4.4.1 cannot be applied directly. However, adopting an 'enlargement' technique [Brockett, 1973; Justh and Krishnaprasad, 2015a], we can state an analogous maximum principle. We recognize that the loop group $\mathscr{G}_k$ is a subset of $\mathscr{R}_k$. The space $\mathscr{R}_k$ can then be regarded as the 'raised' state space. The dynamics (4.10), along with the initial condition $g(0,\theta) = g_0(\theta) \in G$ for all $\theta \in S^1$, ensures that $g(t,\theta)$ remains in G for all $(t,\theta) \in [0,T] \times S^1$. Endow the space $\mathrm{gl}(r,\mathbb{R})$ with the trace inner product and an induced norm, i.e. $\langle A, B\rangle_{\mathrm{gl}(r,\mathbb{R})} = \mathrm{tr}\left(A^\mathsf{T} B\right)$ and $\|A\|_{\mathfrak{gl}(r)} = \sqrt{\mathrm{tr}\left(A^\mathsf{T} A\right)}$, for $A, B \in \mathrm{gl}(r,\mathbb{R})$. We now define the pre-Hamiltonian $H : \mathscr{R}_k \times U \times \mathbb{R} \times \mathscr{R}_k \to \mathbb{R}$ as,

$$H(g(t), u(t), p_0, p(t)) = \langle p(t), g(t)\xi(u(t))\rangle_{\mathscr{R}_k} + p_0 L(u(t)), \tag{4.34}$$

where the duality pairing in the definition of H can be explicitly written as,

$$\begin{aligned}\langle p(t), g(t)\xi(u(t))\rangle_{\mathscr{R}_k} &= \int_0^{2\pi} \sum_{i=0}^{k} \left\langle \frac{d^i}{d\theta^i} p(t,\theta), \frac{d^i}{d\theta^i}\left(g(t,\theta)\xi(u(t,\theta))\right)\right\rangle_{\mathrm{gl}(r,\mathbb{R})} d\theta \\ &= \int_0^{2\pi} \sum_{i=0}^{k} \mathrm{tr}\left(\frac{d^i}{d\theta^i} p(t,\theta)^\mathsf{T} \cdot \frac{d^i}{d\theta^i}\left(g(t,\theta)\xi(u(t,\theta))\right)\right) d\theta.\end{aligned}$$

We are now all set to apply Theorem 4.4.1. If $u^* \in \mathcal{U}$ is an optimal control, then we have,

$$H(g^*(t), u^*(t), p_0^*, p^*(t)) = \max_{v \in U} H(g^*(t), v, p_0^*, p^*(t)). \tag{4.35}$$

It is obvious that $\frac{\delta H}{\delta p^*}(g^*, u^*, p_0^*, p^*) = g^*\xi(u^*) = \dot{g}^*$. We can also derive for any $\tilde{g}(t) \in \mathscr{R}_k$, (suppressing other arguments)

$$\frac{\delta H}{\delta g^*} \cdot \tilde{g} = \lim_{\alpha \to 0} \frac{H(g^* + \alpha\tilde{g}) - H(g^*)}{\alpha} = \langle p^*, \tilde{g}\xi(u^*)\rangle_{\mathscr{R}_k} = \left\langle p^*\xi(u^*)^\mathsf{T}, \tilde{g}\right\rangle_{\mathscr{R}_k},$$

which implies the adjoint equation to (4.10) is,

$$\dot{p}^*(t) = -p^*(t) \cdot \xi(u^*(t))^{\mathsf{T}}. \tag{4.36}$$

■

4.5 Special Case : $G = \mathrm{H}(3)$

The previous section on optimal control provides a concrete foundation in which we can state the maximum principle for the considered optimal control problem. In this section, we will explore a special case where we take the Lie group, G as the Heisenberg group, H(3). Note that the finite number of particles case of this problem has been considered in [Justh and Krishnaprasad, 2016] and hence this work can be thought as a continuum counterpart of it. In H(3), $g(t,\theta) \in \mathrm{H}(3)$ has the structure,

$$g = \begin{bmatrix} 1 & x_1 & x_3 + \frac{x_1 x_2}{2} \\ 0 & 1 & x_2 \\ 0 & 0 & 1 \end{bmatrix},$$

that satisfy the group evolution equation,

$$\frac{\partial}{\partial t} g(t,\theta) = g(t,\theta) \cdot \left(u_1(t,\theta) A_1 + u_2(t,\theta) A_2\right), \tag{4.37}$$

where,

$$A_1 = \begin{bmatrix} 0 & 1 & 0 \\ 0 & 0 & 0 \\ 0 & 0 & 0 \end{bmatrix}, \quad A_2 = \begin{bmatrix} 0 & 0 & 0 \\ 0 & 0 & 1 \\ 0 & 0 & 0 \end{bmatrix},$$

along with $A_3 = [A_1, A_2]$, form an orthonormal basis for the associated Lie algebra $\mathfrak{h}(3)$. We attempt to address the optimal control problem formulated before, under this Heisenberg group setting, i.e. we solve the following,

$$\begin{aligned}\min \int_0^T L(u)dt &= \int_0^T \int_0^{2\pi} \mathcal{L}(u)d\theta dt \\ &= \frac{1}{2}\int_0^T \int_0^{2\pi} \left((u_1^2 + u_2^2) + \chi \left(\left(\frac{\partial u_1}{\partial \theta} \right)^2 + \left(\frac{\partial u_2}{\partial \theta} \right)^2 \right) \right) d\theta dt,\end{aligned} \tag{4.38}$$

where $\mathcal{L}$ is called the Lagrange density function.

4.5.1 Controllability

It is a direct exercise of the generalized Chow-Rashevsky theorem 4.3.1 to show weak controllability in this case. The loop algebra $C^\infty(S^1, \mathfrak{h}(3))$ is spanned by $\{e^{im_1\theta}A_1, e^{im_2\theta}A_2, e^{im_3\theta}A_3\}$. The family $\mathcal{F}$ of left invariant vector fields that is chosen by means of control inputs is given by $\mathcal{F} = \{X_1^{m_1}, X_2^{m_2}\}$, where

$$X_r^{m_r} f(g) = (Df)_g \cdot g e^{im_r\theta} A_r, \quad f \in \mathcal{D}, r = 1, 2.$$

Since the only non-vanishing brackets in $\mathfrak{h}(3)$ are $[A_1, A_2] = A_3 = -[A_2, A_1]$, the set $\text{Lie}_g\ \mathcal{F}$ would span the tangent space at every point $g \in C^\infty(S^1, \text{H}(3))$.

However, we can provide an argument that establishes the strong controllability in this case. Here we describe an approach to construct a candidate smooth control given any endpoint conditions $x_i^0(\theta)$ and $x_i^T(\theta)$, $i = 1, 2, 3$. Without loss of generality, we may assume $x_i^0(\theta) = 0$ for all i. Now since, $x_i(t, \theta) =$

$\int_0^t u_i(t,\theta)dt, i = 1,2$, we can choose smooth controls $v_i(t,\theta), t \in [0,\bar{t}\,], i = 1,2$, for some $\bar{t} < T$, such that x_1 and x_2 reach their final endpoints. At time $t = \bar{t}$, let the 'error' in x_3 variable be denoted as $\Delta x_3(\theta) = x_3^T(\theta) - x_3(\bar{t},\theta)$. Note that without loss of generality, we may assume that $\Delta x_3(\theta) > 0$ for all θ. We know that in a single nonholonomic integrator case, if we complete a loop in time for (x_1, x_2) variables, the change in x_3 variable will be given by the area of the loop. We may use the same idea in the continuum case to construct smooth controls. We can generate the following circular loops (in time) in (x_1, x_2) variables,

$$\begin{pmatrix} x_1(t,\theta) \\ \\ x_2(t,\theta) \end{pmatrix} = \begin{pmatrix} x_1^T(\theta) - r(\theta) \\ \\ x_2^T(\theta) \end{pmatrix} + r(\theta) \begin{pmatrix} \cos(\omega(t-\bar{t})) \\ \\ \sin(\omega(t-\bar{t})) \end{pmatrix}, \tag{4.39}$$
$$\omega = \frac{2\pi}{T-\bar{t}},\ t \in (\bar{t}, T],$$

where $r(\cdot)$ is a smooth function in θ. The controls required to generate these loops are given by

$$\begin{pmatrix} \tilde{v}_1(t,\theta) \\ \\ \tilde{v}_2(t,\theta) \end{pmatrix} = r(\theta)\omega \begin{pmatrix} -\sin(\omega(t-\bar{t})) \\ \\ \cos(\omega(t-\bar{t})) \end{pmatrix}, \tag{4.40}$$

We then compute,

$$\begin{aligned} x_3(T,\theta) &= x_3(\bar{t},\theta) + \frac{1}{2}\int_{\bar{t}}^{T} (x_1(t,\theta)\tilde{v}_2(t,\theta) - x_2(t,\theta)\tilde{v}_1(t,\theta))dt \\ &= x_3^T(\theta) - \Delta x_3(\theta) + \pi r^2(\theta). \end{aligned}$$

Since $\Delta x_3(\cdot)$ is smooth, we can always choose smooth function $r(\cdot)$ such that

$\Delta x_3(\theta) = \pi r^2(\theta)$, and thus the smooth controls

$$u_i(t,\theta) = \begin{cases} v_i(t,\theta), & t \in [0,\bar{t}\,] \\ \\ \tilde{v}_i(t,\theta), & t \in (\bar{t},T] \end{cases}, \quad i = 1,2, \tag{4.41}$$

make the required state transitions possible. This shows that in the Heisenberg case we have strong controllability.

Remark 4.2. We can assume $\Delta x_3 > 0$ for all θ because if it was not the case, we could add another piece of controls $\hat{v}_i$'s before applying the controls $\tilde{v}_i$'s. The purpose of the controls $\hat{v}_i$'s would be to make the states (x_1, x_2) undergo a circular loop of radius $\hat{r}$, for all θ. This will produce a change in the x_3 variable by $\pi\hat{r}^2$ for all θ. Hence the new error can be written as $\overline{\Delta x_3}(\theta) = \Delta x_3(\theta) + \pi\hat{r}^2$. We can always pick a $\hat{r}$ so that $\overline{\Delta x_3}(\theta) > 0$ for all θ.

4.5.2 Equations of Optimal Control

Necessary conditions for optimality can be derived by various methods. We will present two such approaches to solve the optimal control problem (4.38).

4.5.2.1 Calculus of Variations Approach

Note that the group dynamics in (4.37) can also be expressed by the differential equations,

$$\frac{\partial x_1}{\partial t} = u_1, \tag{4.42}$$

$$\frac{\partial x_2}{\partial t} = u_2, \tag{4.43}$$

$$\frac{\partial x_3}{\partial t} = \frac{1}{2}(x_1 u_2 - x_2 u_1). \tag{4.44}$$

Since we have an integral constraint, namely, $\Delta x_3(\theta) = \frac{1}{2}\int_0^T (x_1 u_2 - x_2 u_1)dt$, we invoke a Lagrange multiplier, $\lambda \in C^\infty(S^1, \mathbb{R})$ to write the augmented Lagrangian density function as,

$$\mathcal{L} = \frac{1}{2}\left[\left(x_{1,t}^2 + x_{2,t}^2\right) + \chi\left(x_{1,\theta t}^2 + x_{2,\theta t}^2\right) + \lambda\left(x_1 x_{2,t} - x_2 x_{1,t}\right)\right]. \tag{4.45}$$

where we adopted the notation conventions $x_{i,\theta} = \frac{\partial x_i}{\partial \theta}, x_{i,t\theta} = \frac{\partial^2 x_i}{\partial t \partial \theta} = x_{i,\theta t}$ etc. Application of the Euler-Lagrange equations (4.22) gives the following equations,

$$\begin{aligned} \frac{\partial^2 x_1}{\partial t^2} &= \lambda \frac{\partial x_2}{\partial t} + \chi \frac{\partial^4 x_1}{\partial \theta^2 \partial t^2} \\ \frac{\partial^2 x_2}{\partial t^2} &= -\lambda \frac{\partial x_1}{\partial t} + \chi \frac{\partial^4 x_2}{\partial \theta^2 \partial t^2}, \end{aligned} \tag{4.46}$$

which yields the evolution equations for optimal controls,

$$\begin{aligned} \mathcal{A}\frac{\partial u_1}{\partial t} &= \lambda u_2 \\ \mathcal{A}\frac{\partial u_2}{\partial t} &= -\lambda u_1, \end{aligned} \tag{4.47}$$

where we denote $\mathcal{A} := (1 - \chi\Delta)$, Δ being the Laplacian.

Remark 4.3. $\mathcal{A}$ is a positive definite self adjoint operator in $C^\infty(S^1, \mathbb{R})$, having eigenvalues $\alpha_n = 1 + \chi n^2$ with associated eigenvectors $e_n = e^{in\theta}$ for $n \in \mathbb{Z}$.

Lemma 4.5.1. *The quantities,*

$$h_n = \int_0^{2\pi} \left(\frac{\partial^n u_1}{\partial t^n} \mathcal{A} \frac{\partial^n u_1}{\partial t^n} + \frac{\partial^n u_2}{\partial t^n} \mathcal{A} \frac{\partial^n u_2}{\partial t^n} \right) d\theta, \quad n = 0, 1, 2, ... \tag{4.48}$$

are conserved along any optimal trajectories satisfying (4.47).

Proof. It is easy to establish that for each n, $\frac{dh_n}{dt} = 0$, which follows directly from the way optimal controls behave in (4.47) and the fact that the operator $\mathcal{A}$ is self adjoint. ■

4.5.2.2 PMP Approach

We introduce the costate variable $p(t) = (p_1(t), p_2(t), p_3(t)) \in C^\infty(S^1; \mathbb{R}^3)$, $t \in [0, T]$. The pre-Hamiltonian can be written as (considering only normal extremals, i.e. where $p_0 \neq 0$ and can be normalized to -1),

$$\begin{aligned} H &= \langle \dot{x}, p \rangle - L \\ &= \int_0^{2\pi} \left(u_1 p_1 + u_2 p_2 + \frac{1}{2}(x_1 u_2 - x_2 u_1) p_3 - \frac{1}{2}\left(u_1^2 + u_2^2\right) - \frac{\chi}{2}\left(u_{1,\theta}^2 + u_{2,\theta}^2\right) \right) d\theta. \end{aligned} \tag{4.49}$$

Remark 4.4. Note that the finite codimensionality assumption is satisfied in this case. To see this, note that the components of members of the 'reachability set' (4.25) can be expressed as,

$$\begin{aligned} z_1(T) &= \int_0^T w_1(t) dt \\ z_2(T) &= \int_0^T w_2(t) dt \\ z_3(T) &= \frac{1}{2} \int_0^T \left(z_1(t) u_2^*(t) - z_2(t) u_1^*(t) \right) dt + \frac{1}{2} \int_0^T \left(x_1^*(t) w_2(t) - x_2^*(t) w_1(t) \right) dt, \end{aligned}$$

where $w(t) = (w_1(t), w_2(t))$ is any arbitrary control input. If we denote trajectories corresponding to any input $u(\cdot)$ as $x^u(t) = x(t, u(\cdot))$, then, $z_1(T) = x_1^w(T), z_2(T) = x_2^w(T)$. Furthermore note that,

$$\begin{aligned} z_3(T) = \frac{1}{2}\Bigg[&\int_0^T (x_1^* u_2^* - x_2^* u_1^*)dt + \int_0^T (x_1^w w_2 - x_2^w w_1)dt \\ &- \int_0^T ((x_1^* - x_1^w)(u_2^* - w_2) - (x_2^* - x_2^w)(u_1^* - w_1))dt\Bigg] \\ = x_3^*(T) + x_3^w(T) - \tilde{x}_3(T), \end{aligned}$$

where $\tilde{x} = x^* - x^w$. We may now choose $w = u^*$. This makes $\tilde{x}(T) = 0$ and $(z_1(T), z_2(T), z_3(T)) = (x_1^*(T), x_2^*(T), 2x_3^*(T))$. Since the Heisenberg case is strongly controllable, the 'reachability set' R spans the whole of the state space X, making it trivially finite codimensional in X.

We can now directly apply Theorem 4.4.1 to derive necessary optimality conditions. The maximum principle would require us to maximize (4.49) pointwise over the controls, i.e. we are attempting to find the Hamiltonian as,

$$\begin{aligned} \mathcal{H}(x,p) &= \sup_{v_1,v_2 \in C^\infty(S^1;\mathbb{R})} H(x, \{v_i\}_{i=1}^2, p) \\ &= \sup_{v_1,v_2 \in C^\infty(S^1;\mathbb{R})} \int_0^{2\pi} \Bigg(v_1 p_1 + v_2 p_2 + \frac{1}{2}(x_1 v_2 - x_2 v_1) p_3 \\ &\qquad - \frac{1}{2}\left(v_1^2 + v_2^2\right) - \frac{\chi}{2}\left(v_{1,\theta}^2 + v_{2,\theta}^2\right)\Bigg) d\theta \end{aligned} \tag{4.50}$$

This maximization results in two Euler-Lagrange equations,

$$\frac{\partial H}{\partial v_i} - \frac{\partial}{\partial \theta}\left(\frac{\partial H}{\partial v_{i,\theta}}\right) = 0, \quad i = 1, 2, \tag{4.51}$$

that yield the optimal controls,

$$\begin{aligned} \mathcal{A}u_1 &= p_1 - \frac{1}{2}x_2p_3, \\ \mathcal{A}u_2 &= p_2 + \frac{1}{2}x_1p_3, \end{aligned} \tag{4.52}$$

with the usual definition of $\mathcal{A} = (1 - \chi\Delta)$. The Hamiltonian can be read as,

$$\begin{aligned} \mathcal{H} &= \frac{1}{2}\int_0^{2\pi} (u_1\mathcal{A}u_1 + u_2\mathcal{A}u_2)\, d\theta \\ &= \frac{1}{2}\int_0^{2\pi} \left[\left(p_1 - \frac{1}{2}x_2p_3\right)\mathcal{A}^{-1}\left(p_1 - \frac{1}{2}x_2p_3\right)\right. \\ &\qquad \left. + \left(p_2 + \frac{1}{2}x_1p_3\right)\mathcal{A}^{-1}\left(p_2 + \frac{1}{2}x_1p_3\right)\right] d\theta \end{aligned} \tag{4.53}$$

The dynamics of the costate variable p can be calculated from Hamilton's equation, $\frac{\partial p}{\partial t} = -\frac{\delta\mathcal{H}}{\delta x}$, where $\frac{\delta\mathcal{H}}{\delta x}$ denotes the functional derivative of $\mathcal{H}$ with respect to x. Note that the Hamiltonian function $\mathcal{H}$ is smooth in x, so we can take this derivative. This can be defined as, $D\mathcal{H}(x_i)\cdot\sigma = \left\langle \frac{\delta\mathcal{H}}{\delta x_i}, \sigma \right\rangle$, $i = 1, 2, 3$, where $D\mathcal{H}(x_i)\cdot\sigma$ is the Fréchet derivative of $\mathcal{H}$ at x_i in the direction of σ. This is defined as,

$$D\mathcal{H}(x_i)\cdot\sigma = \frac{d}{d\epsilon}\mathcal{H}(x_1 + \epsilon\sigma)\bigg|_{\epsilon=0}.$$

We may calculate, for $i = 1$,

$$\begin{aligned} D\mathcal{H}(x_1)\cdot\sigma &= \frac{1}{2}\frac{d}{d\epsilon}\int_0^{2\pi} \left[\left(p_1 - \frac{1}{2}x_2p_3\right)\mathcal{A}^{-1}\left(p_1 - \frac{1}{2}x_2p_3\right)\right. \\ &\qquad \left. + \left(p_2 + \frac{1}{2}(x_1 + \epsilon\sigma)p_3\right)\mathcal{A}^{-1}\left(p_2 + \frac{1}{2}(x_1 + \epsilon\sigma)p_3\right)\right] d\theta\bigg|_{\epsilon=0} \\ &= \frac{1}{2}\int_0^{2\pi} \left(\sigma p_3\mathcal{A}^{-1}\left(p_2 + \frac{1}{2}(x_1 + \epsilon\sigma)p_3\right)\right) d\theta \\ &= \frac{1}{2}\int_0^{2\pi} \left(\sigma p_3\mathcal{A}^{-1}\left(p_2 + \frac{1}{2}x_1p_3\right)\right) d\theta \\ &= \left\langle \frac{p_3}{2}\mathcal{A}^{-1}\left(p_2 + \frac{1}{2}x_1p_3\right), \sigma \right\rangle, \end{aligned} \tag{4.54}$$

so that we may write,

$$\frac{\delta \mathcal{H}}{\delta x_1} = \frac{p_3}{2}\mathcal{A}^{-1}\left(p_2 + \frac{1}{2}x_1 p_3\right). \tag{4.55}$$

We can similarly calculate $\frac{\delta \mathcal{H}}{\delta x_2} = -\frac{p_3}{2}\mathcal{A}^{-1}\left(p_1 - \frac{1}{2}x_2 p_3\right)$ and $\frac{\delta \mathcal{H}}{\delta x_3} = 0$. The evolution of p can then be expressed as,

$$\begin{aligned}
\frac{\partial p_1}{\partial t} &= -\frac{p_3}{2}\mathcal{A}^{-1}\left(p_2 + \frac{1}{2}x_1 p_3\right) \\
\frac{\partial p_2}{\partial t} &= \frac{p_3}{2}\mathcal{A}^{-1}\left(p_1 - \frac{1}{2}x_2 p_3\right) \\
\frac{\partial p_3}{\partial t} &= 0.
\end{aligned} \tag{4.56}$$

From (4.52) and (4.56), we notice that,

$$\begin{aligned}
\frac{\partial}{\partial t}\mathcal{A}u_1 &= -p_3\mathcal{A}^{-1}u_2 \\
\frac{\partial}{\partial t}\mathcal{A}u_2 &= p_3\mathcal{A}^{-1}u_1
\end{aligned} \tag{4.57}$$

Hence, recognizing p_3 as the negative of Lagrange multiplier λ in the previous section, we rediscover (4.47).

4.5.3 Behavior of Optimal Control

Denote, $z(t,\theta) := u_1(t,\theta) + \mathrm{i}u_2(t,\theta)$. Then, (4.47) can be expressed as,

$$\mathcal{A}\frac{\partial z}{\partial t} = -\mathrm{i}\lambda z. \tag{4.58}$$

Since u_1, u_2 are periodic functions in θ with period 2π, they have a Fourier series representation, $u_\nu(t,\theta) = \sum_{n=-\infty}^{\infty} u_n^{(\nu)}(t)e^{\mathrm{i}n\theta}$, $\nu = 1, 2$, where $u_n^{(\nu)}$'s are the Fourier

coefficients of u_ν. Moreover, since u_ν's are real valued functions of θ, we have, $u_{-n}^{(\nu)} = \overline{u_n^{(\nu)}}$. Transforming (4.58) in Fourier domain, we get,

$$A\frac{d\check{z}}{dt} = -\mathrm{i}\Lambda\check{z}, \tag{4.59}$$

where we denote, $A = \mathrm{diag}\left(\{\alpha_n\}_{n=-\infty}^{\infty}\right)$, $\check{z}(t) = [z_n(t)]_{-\infty}^{\infty}$. $z_n(t) = u_n^{(1)}(t) + \mathrm{i}u_n^{(2)}(t)$, i.e. $z_n(t)$'s are Fourier coefficients of $z(t,\theta)$. Λ is the infinite Toeplitz matrix generated by the Fourier coefficients of λ, i.e.

$$\Lambda = \begin{pmatrix} \lambda_0 & \lambda_{-1} & \lambda_{-2} & \cdots \\ \lambda_1 & \lambda_0 & \lambda_{-1} & \cdots \\ \lambda_2 & \lambda_1 & \lambda_0 & \cdots \\ \cdots & \cdots & \cdots & \cdots \end{pmatrix} \tag{4.60}$$

Since λ_n's are Fourier coefficients of real valued function λ, we have $\lambda_{-n} = \overline{\lambda_n}$. This leads to the observation that Λ is (infinite) Hermitian matrix, i.e. $\Lambda = \Lambda^*$.

4.5.3.1 Truncation of Fourier Coefficients

Here we will consider first $N+1$ Fourier coefficients of z and provide an analysis of (4.59) in the truncated finite dimensional case. We write, $\check{z}_N = (z_{-N} \cdots z_0 \cdots z_N)^T \in \mathbb{C}^{2N+1}$. Then, the truncated version of (4.59) can be written as,

$$A_N\frac{d\check{z}_N}{dt} = -\mathrm{i}\Lambda_N\check{z}_N, \tag{4.61}$$

where A_N and Λ_N's are appropriately truncated matrices from A and Λ, respectively. Note that $A_N \succ 0$. Let us denote, $\hat{z} = A_N^{1/2}\check{z}_N$ and $B_N = A_N^{-1}$, then we get,

$$\frac{d\hat{z}}{dt} = -\mathrm{i}\hat{\Lambda}_N \hat{z}, \tag{4.62}$$

where $\hat{\Lambda}_N = B_N^{1/2} \Lambda_N B_N^{1/2} = \left(\hat{\Lambda}_N\right)^*$. Since the matrix $-\mathrm{i}\hat{\Lambda}_N$ is skew Hermitian, all its eigenvalues are on the imaginary axis. Denote them by $-\mathrm{i}\sigma_n,\ \sigma_n \in \mathbb{R}$, for $n = -N, ..., N$. There exists a unitary matrix V that diagonalizes $-\mathrm{i}\hat{\Lambda}_N$, i.e.

$$-\mathrm{i}\hat{\Lambda}_N = V^* D V, \quad D = \mathrm{diag}(\{-\mathrm{i}\sigma_n\}).$$

We perform another coordinate change by,

$$\tilde{z} = V\hat{z} = V A_N^{1/2} \check{z}_N, \tag{4.63}$$

which yields the decoupled equations,

$$\frac{d\tilde{z}}{dt} = D\tilde{z}, \tag{4.64}$$

i.e.

$$\begin{aligned} \frac{d\tilde{z}_n}{dt} &= -\mathrm{i}\sigma_n \tilde{z}_n, \\ \implies \tilde{z}_n(t) &= e^{-\mathrm{i}\sigma_n t}\tilde{z}_n(0), \quad n = -N, \cdots, N. \end{aligned} \tag{4.65}$$

Performing the inverse Fourier operation, we see that,

$$\begin{aligned} \tilde{z}(t,\theta) &= \sum_{n=-N}^{N} \tilde{z}_n(t) e^{\mathrm{i}n\theta} \\ \implies \tilde{z}(t,\theta) &= \sum_{n=-N}^{N} e^{\mathrm{i}(n\theta - \sigma_n t)} \tilde{z}_n(0). \end{aligned} \tag{4.66}$$

This is an equation of superposition of $2N+1$ traveling waves with n being the wave number and $v_n = \frac{\sigma_n}{n}$ is the speed of propagation associated with n-th mode of the wave.

4.5.3.2 Velocity of Propagation

We know that in the wave equation of (4.66), the velocity v_n of propagation corresponding to n-th frequency is determined as, $v_n = \frac{\sigma_n}{n}$, where σ_n's are (real) eigenvalues of the Hermitian matrix $\hat{\Lambda}_N = B_N^{1/2}\Lambda_N B_N^{1/2}$. Since $B_N^{1/2}\Lambda_N B_N^{1/2} \sim \Lambda_N B_N \sim B_N \Lambda_N$ (similar matrices), the eigenvalues of $\hat{\Lambda}_N$ can be characterized by those of B_N and Λ_N.

We have $\text{eig}(B_N) = \{\beta_n\}_{-N}^{N}$, where $\beta_n = \frac{1}{\alpha_n} = \frac{1}{1+\chi n^2}$. Now, Λ_N is a Toeplitz Hermitian matrix formed by the Fourier coefficients $\{\lambda_n\}_{-2N}^{2N}$. Given those coefficients, it is in general not possible to write down closed form representation of its eigenvalues. However, the bounds of eigenvalues of such a matrix is well known. We will make a little detour to state these results.

4.5.3.3 Toeplitz Matrices and Eigenvalues

Let f be a periodic function over the interval $[0, 2\pi)$ and $\{f_n\}$ are its Fourier coefficients. Let us denote $T_n(f)$, the $n \times n$ Toeplitz Hermitian matrix defined as,

$$T_n(f) = \begin{pmatrix} f_0 & f_{-1} & f_{-2} & \cdots & f_{-(n-1)} \\ f_1 & f_0 & f_{-1} & \cdots & f_{-(n-2)} \\ f_2 & f_1 & f_0 & \cdots & \\ \vdots & & & \ddots & \vdots \\ f_{(n-1)} & & & & f_0 \end{pmatrix}. \tag{4.67}$$

We also define,

$$m_f = \operatorname{ess\,inf}(f), \tag{4.68}$$

$$M_f = \operatorname{ess\,sup}(f). \tag{4.69}$$

Let the eigenvalues of $T_n(f)$ be denoted by $\tau_{n,k}, k = 1, ..., n$. Then,

$$m_f \leq \tau_{n,k} \leq M_f. \tag{4.70}$$

Note that, $\max_k |\tau_{n,k}| \leq \max(|m_f|, |M_f|) \leq M_{|f|}$. We recall another useful result here.

Lemma 4.5.2. *Let P, Q be Hermitian positive definite matrices of same order. If $\tau(X)$ denote eigenvalues of X, then,*

$$\tau_{\max}(PQ) \leq \tau_{\max}(P) \cdot \tau_{\max}(Q) \tag{4.71}$$

$$\tau_{\min}(PQ) \geq \tau_{\min}(P) \cdot \tau_{\min}(Q) \tag{4.72}$$

4.5.3.4 Bounds on the Velocity

To get bounds on σ_n's, we need an useful assumption that will be apparent shortly.

A-1 $m_\lambda > 0$, i.e. $\Lambda_N = T_{2N+1}(\lambda) \succ 0$.

Since $\mu_n = \tau(B_N T_{2N+1}(\lambda))$, Lemma 4.5.2 gives the following bound, for $n = -N, ..., N$,

$$\begin{aligned} &\tau_{\min}(B_N)\tau_{\min}(T_{2N+1}(\lambda) \leq \sigma_n \leq \tau_{\max}(B_N)\tau_{\max}(T_{2N+1}(\lambda)), \\ &\implies \frac{m_\lambda}{1+\chi N^2} \leq \sigma_n \leq M_\lambda. \end{aligned} \tag{4.73}$$

Accordingly, the velocity is bounded by,

$$\frac{m_\lambda}{n(1+\chi N^2)} \leq v_n \leq \frac{M_\lambda}{n} \tag{4.74}$$

Remark 4.5. The assumption A-1 can be extended to include the case $M_\lambda < 0$, i.e. $\Lambda_N \prec 0$ as well.

4.5.3.5 Special Cases

1. *Case - I: Constant λ :*

   $\lambda(\theta) = \lambda_0 \neq 0$, a constant. We may assume that $\lambda_0 > 0$. In this case, (4.59) can be explicitly solved and the solution can be expressed as,

   $$z(t,\theta) = \sum_{\substack{n=-\infty \\ n\neq 0}}^{\infty} e^{in\left(\theta - \frac{\beta_n \lambda_0}{n} t\right)} z_n(0) + e^{-j\lambda_0 t} z_0(0). \tag{4.75}$$

   Here the velocities v_n can be written as, $v_n = \frac{\lambda_0}{n(1+\chi n^2)}, n \in \mathbb{Z} \setminus \{0\}$.

2. *Case - II: Band-limited λ :*

   Here, we consider only one frequency component of λ, i.e. $\lambda(\theta) = \lambda_0 + \lambda_1 e^{\mathrm{i}\theta} + \lambda_{-1} e^{-\mathrm{i}\theta}$. Let A-1 hold, i.e. $\Lambda_N = T_{2N+1}(\lambda) \succ 0$. In this case, Λ_N is a tri-diagonal Toeplitz matrix. The eigenvalues of such a matrix are known to take the following form.

   Lemma 4.5.3.

$$\tau_k(\Lambda_N) = \lambda_0 + 2\,|\lambda_1| \cos\left(\frac{k\pi}{2N+2}\right), \quad k = 1, ..., 2N+1. \tag{4.76}$$

   This, combined with Lemma 4.5.2, we get the following bound,

$$\frac{\lambda_0 + 2\,|\lambda_1| \cos\left(\frac{(2N+1)\pi}{2N+2}\right)}{1+\chi N^2} \leq \sigma_n \leq \lambda_0 + 2\,|\lambda_1| \cos\left(\frac{\pi}{2N+2}\right) \tag{4.77}$$

4.5.4 Strong Coupling Limit, $\chi \to \infty$

It is interesting to note that in the limit $\chi \to \infty$, the equations (4.47) take simple form. To see this, note that for some $z \in C^\infty(S^1; \mathbb{R})$, we may express

$$\mathcal{A}^{-1} z = \sum_{n=-\infty}^{\infty} \beta_n \langle \phi_n, z \rangle \phi_n,$$

where $\beta_n = \frac{1}{1+\chi n^2}$ are the eigenvalues of $\mathcal{A}^{-1}$, and $\phi_n = e^{\mathrm{i}n\theta}$. This implies,

$$\begin{aligned} \lim_{\chi\to\infty} \mathcal{A}^{-1} z &= \sum_n \left(\lim_{\chi\to\infty} \frac{1}{1+\chi n^2}\right) \langle z, \phi_n \rangle \phi_n \\ &= \langle z, 1 \rangle \\ \implies \lim_{\chi\to\infty} \mathcal{A}^{-1} z &= \int_0^{2\pi} z d\theta. \end{aligned}$$

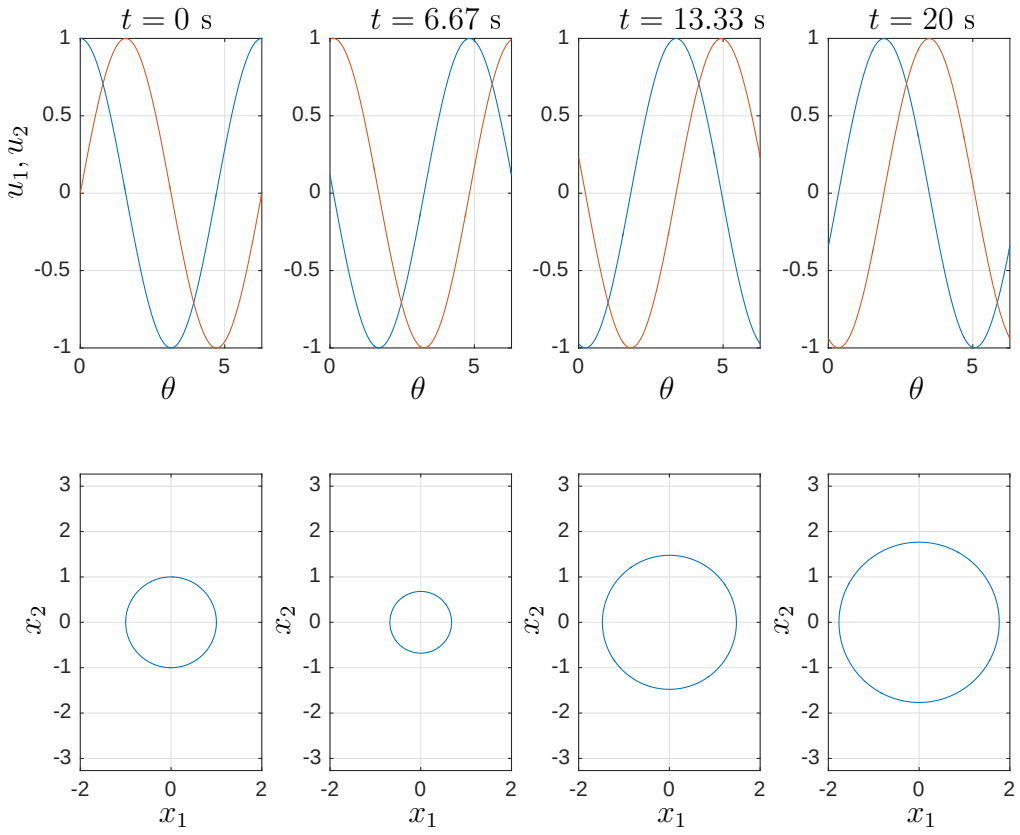

Figure 4.1: Numerical solution of (4.61) for experiment 1. Evolution of u_1 (blue) and u_2 (red) is given in the first row; the controls form a simple traveling wave along the θ domain. The second row shows evolution of x_1, x_2 variables.

With this realization, we may rewrite (4.47) in the strong coupling limit as,

$$\begin{aligned} \frac{\partial u_1}{\partial t} &= \int_0^{2\pi} \lambda u_2 d\theta \\ \frac{\partial u_2}{\partial t} &= -\int_0^{2\pi} \lambda u_1 d\theta. \end{aligned} \tag{4.78}$$

It is clear from (4.52) that both u_1 and u_2 are independent of θ. Then the equations (4.78) can be equivalently written as

$$\begin{aligned} \dot{u}_1 &= \tilde{\lambda} u_2 \\ \dot{u}_2 &= -\tilde{\lambda} u_1, \end{aligned} \tag{4.79}$$

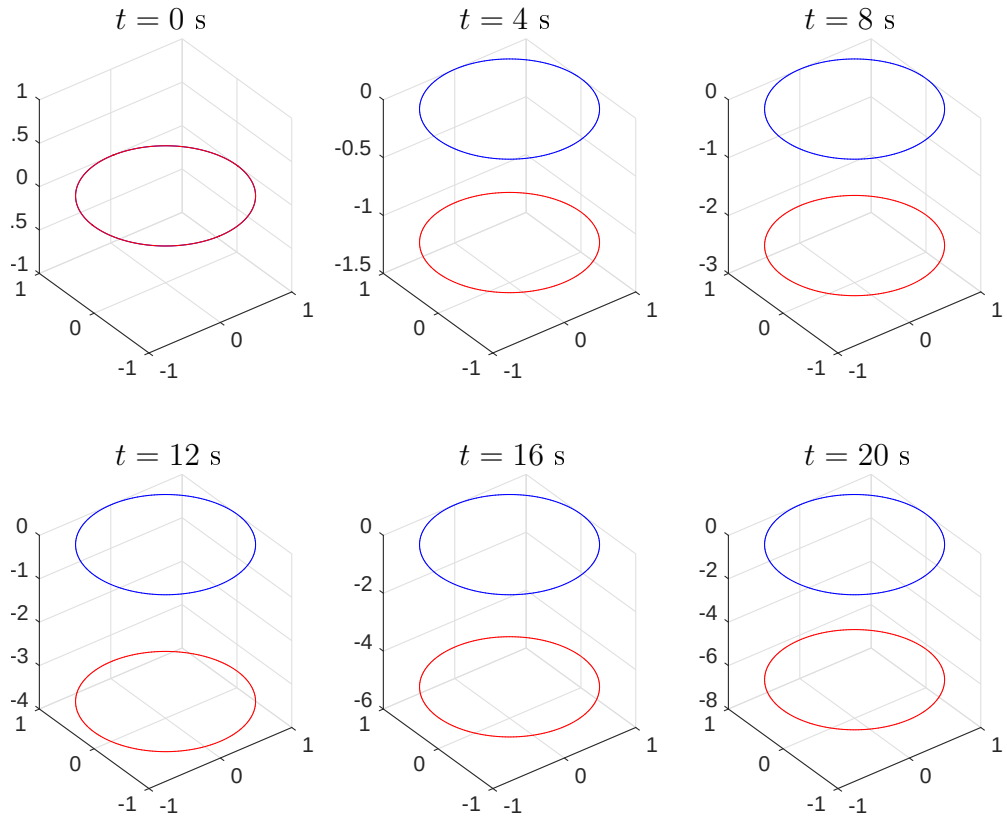

Figure 4.2: Evolution of x_3 for experiment 1. The blue loop represents the circle S^1 while the height of each point on the red loop is given by the value of x_3 at the corresponding point of θ.

where $\tilde{\lambda} = \int_0^{2\pi} \lambda d\theta$. Equations (4.79) are optimal control evolution equations for a single agent [Justh and Krishnaprasad, 2016]. Thus in the strong coupling limit $\chi \to \infty$, the optimal control solutions for the continuum of agents collapses to that of a single agent. This is called the *synchronization* of the flock, where every agent in the flock behaves the same way.

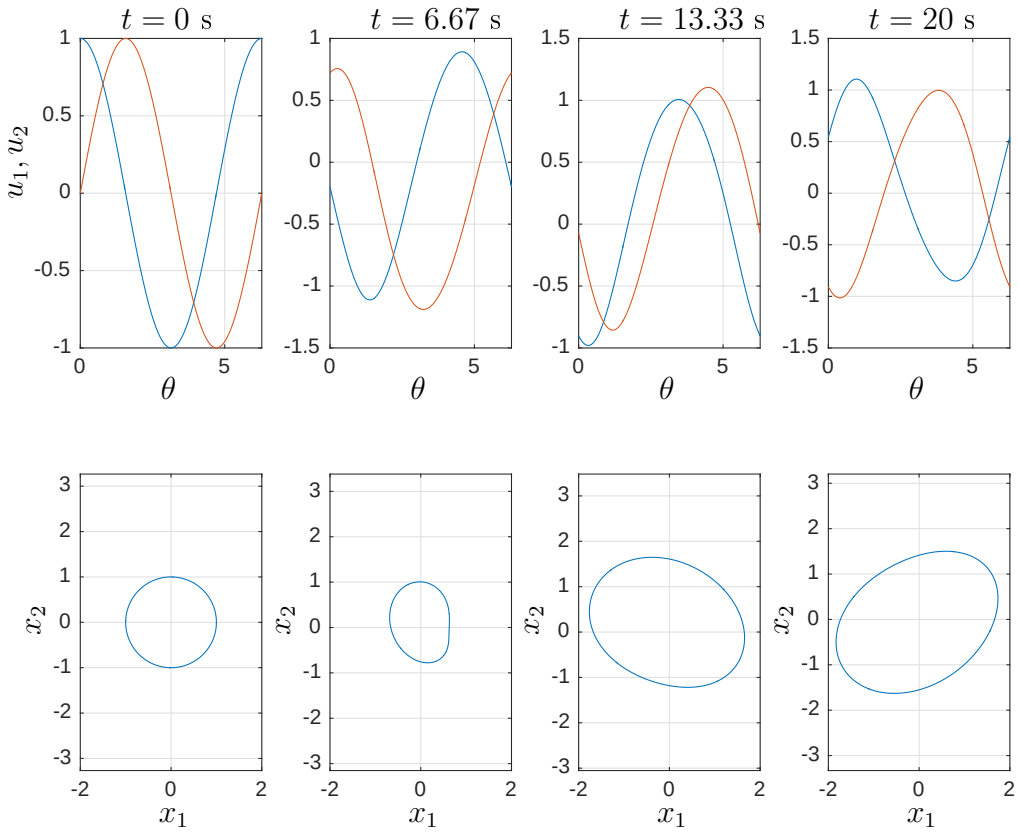

Figure 4.3: Numerical solution of (4.61) for experiment 2. Evolution of u_1 (blue) and u_2 (red) is given in the first row. The second row shows evolution of x_1, x_2 variables.

4.5.5 Simulation Results

We simulate the evolution of optimal controls u_1 and u_2 governed by the linear partial differential equations (4.47) by means of Fourier analysis as presented in the section 4.5.3. In particular, here we present the solutions of the truncated ordinary differential equations (4.61), where we only keep track of first $N + 1$ Fourier coefficients of each variable. Note that λ is assumed to have less than $N + 1$ coefficients. We will now present numerical solutions in different cases by

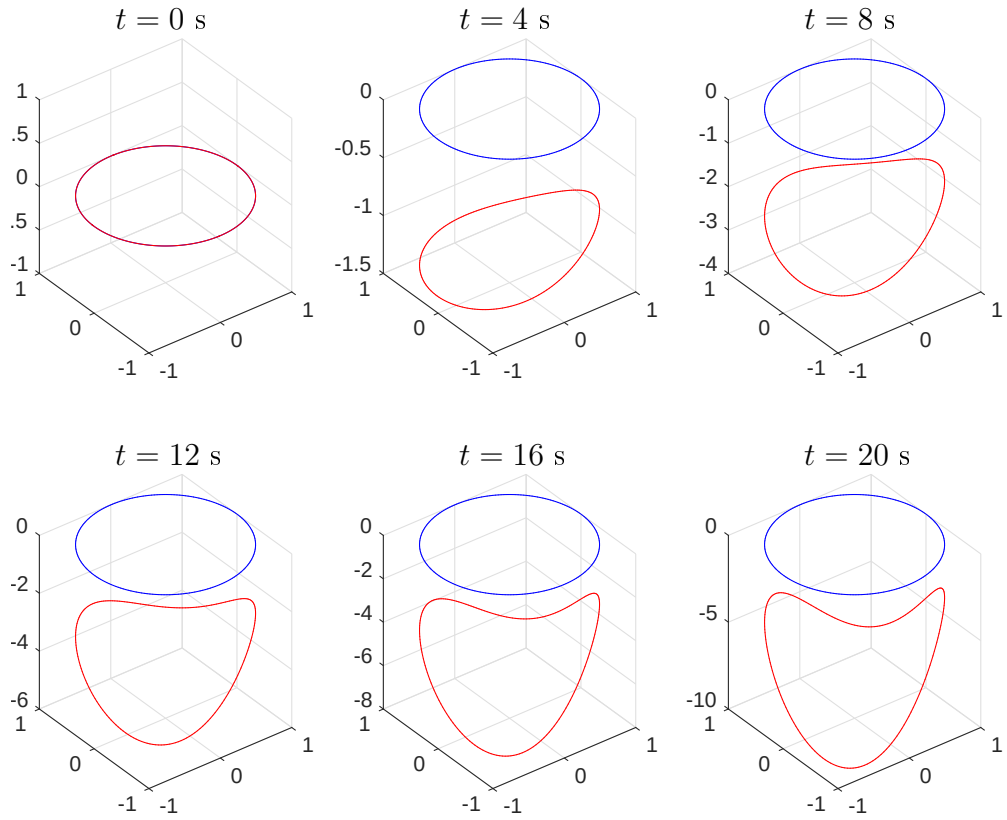

Figure 4.4: Evolution of x_3 for experiment 2. The blue loop represents the circle S^1 while the height of each point on the red loop is given by the value of x_3 at the corresponding point of θ.

varying the initial conditions and parameter values. For all the experiments presented here, N is taken to be 30 and the final time T is set as 20 seconds and four snapshots of the optimal controls are shown. The Hamiltonian is verified to be staying a constant (up to machine precision) for all of the experiments. The evolution of state variables is also recorded. For all the experiments presented here, (x_1, x_2) is set to start from a unit circle and x_3 is initially zero for all values of θ.

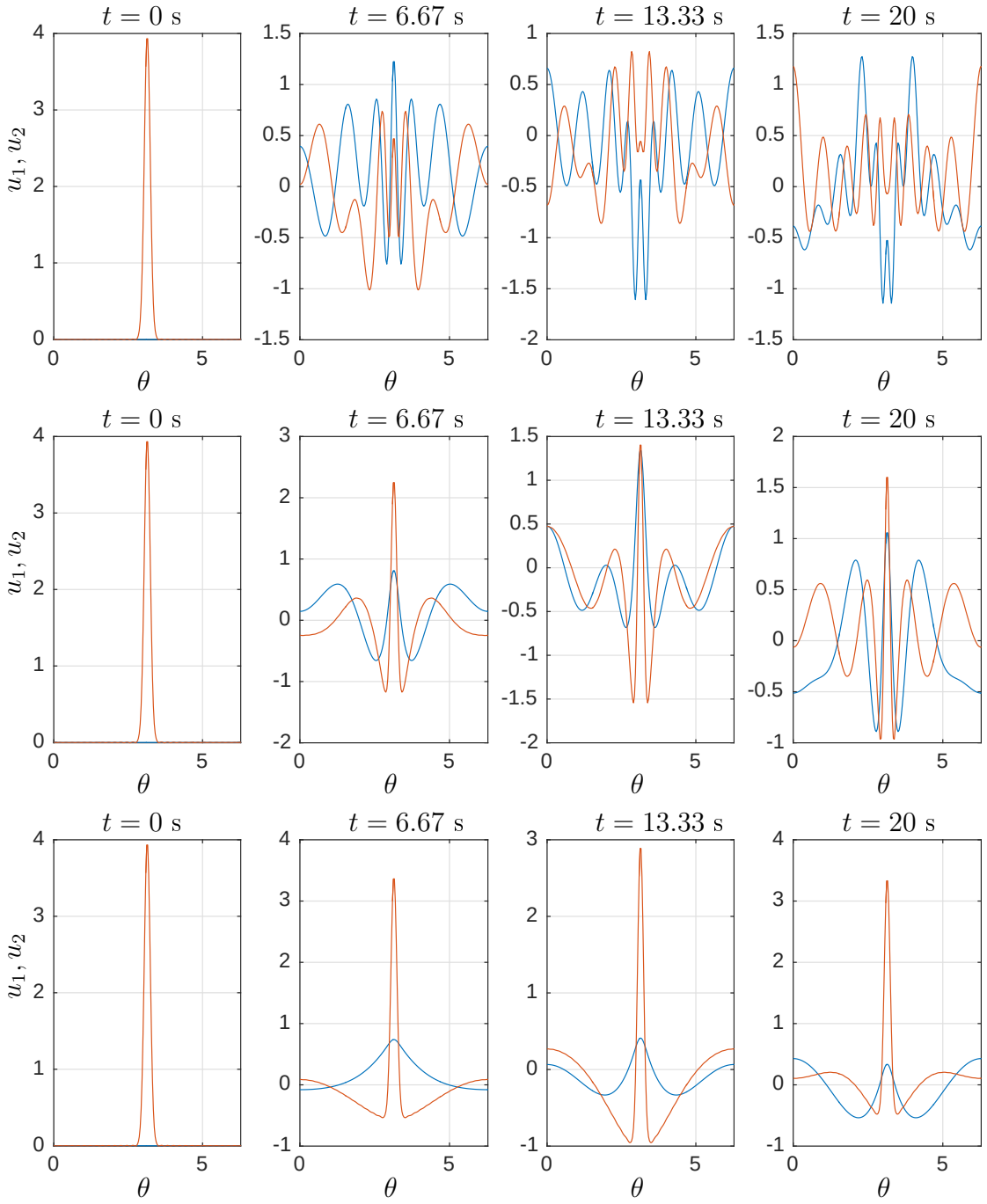

Figure 4.5: Numerical solutions of (4.61) for experiment 3 for (a) first row, $\chi = 0.1$, (b) second row, $\chi = 1$, (c) third row, $\chi = 10$. In all plots, u_1 is shown in blue and u_2 is shown in red. The speed of information propagation decreases as the coupling constant increases.

The simplest set of initial conditions $u_1(0,\theta) = \cos(\theta), u_2(0,\theta) = \sin(\theta), \lambda(\theta) = 5, \chi = 1$ generate a traveling wave solution, according to equation (4.75). This can be seen from Fig. 4.1. The states (x_1, x_2, x_3) are also integrated from an initial condition for (x_1, x_2) forming a circle on the plane and x_3 being identically zero for all θ. The evolution of (x_1, x_2) can be seen from Fig. 4.1. The shape of the (x_1, x_2) circle did not change, although its size varied over time. The evolution of x_3 is shown in Fig. 4.2, which appeared to decrease steadily for all θ. Next, for experiment 2, we consider a band-limited λ, i.e. $\lambda(\theta) = 5 + \cos(\theta)$. Keeping all other conditions same as in experiment 1, we get Fig. 4.3-4.4. Here both size and shape of the (x_1, x_2) circle changed over time. The value of x_3 decreased in this case as well but more asymmetrically than in experiment 1. In experiment 3, we show how a localized disturbance gets spread in the continuum. For this experiment, we let the control u_1 is initially zero everywhere, $u_1(0,\theta) = 0$. However, u_2 has a localized peak at a certain spatial point. We took the example of a Gaussian form,

$$u_2(0,\theta) = \frac{1}{\sqrt{2\pi\rho^2}} e^{-\frac{(\theta-\pi)^2}{2\rho^2}}, \tag{4.80}$$

with $\rho = 0.1$. We then plot the solutions in three different settings of χ values, $\chi = 0.1, 1, 10$ in Fig. 4.5. λ is taken to be a constant in all these cases, $\lambda(\theta) = 5$. It is discovered in the previous section that the speed of traveling wave decreases as χ increases. This can be seen clearly from Fig. 4.5 as the disturbance is seen to be not well propagated for higher values of χ.

4.6 A Continuum of Agents on the Plane

As an extension of the problem considered in Section 3.3, we will explore the case where we take the underlying group as the special Euclidean group, SE(2). This case then can be seen as a continuum counterpart of [Justh and Krishnaprasad, 2015b]. Every $g(t,\theta) \in \mathrm{SE}(2)$ can be represented as,

$$g = \begin{bmatrix} \cos x_3 & -\sin x_3 & x_1 \\ \sin x_3 & \cos x_3 & x_2 \\ 0 & 0 & 1 \end{bmatrix},$$

with group evolution dynamics,

$$\frac{\partial}{\partial t} g(t,\theta) = g(t,\theta) \cdot (u_1(t,\theta) A_1 + u_2(t,\theta) A_2), \tag{4.81}$$

where,

$$A_1 = \begin{bmatrix} 0 & -1 & 0 \\ 1 & 0 & 0 \\ 0 & 0 & 0 \end{bmatrix}, \quad A_2 = \begin{bmatrix} 0 & 0 & 1 \\ 0 & 0 & 0 \\ 0 & 0 & 0 \end{bmatrix},$$

along with $A_3 = [A_1, A_2]$, form a basis for the associated Lie algebra $\mathfrak{se}(2)$. Note that since $\{A_1, A_2\}$ is bracket generating in $\mathfrak{se}(2)$, similar argument as in the Heisenberg case would provide (weak) controllability result in this case as well. We then seek to minimize the same cost functional as in (4.38),

$$J = \frac{1}{2} \int_0^T \int_0^{2\pi} \left((u_1^2 + u_2^2) + \chi \left(\left(\frac{\partial u_1}{\partial \theta} \right)^2 + \left(\frac{\partial u_2}{\partial \theta} \right)^2 \right) \right) d\theta dt$$

4.6.1 Equations of Optimal Control

4.6.1.1 Calculus of Variations Approach

The system dynamics can be equivalently expressed as,

$$\begin{aligned}\frac{\partial x_1}{\partial t} &= u_2 \cos x_3 \\ \frac{\partial x_2}{\partial t} &= u_2 \sin x_3 \\ \frac{\partial x_3}{\partial t} &= u_1.\end{aligned} \tag{4.82}$$

Note that the controls u_1 and u_2 can be expressed by the x_j variables and their derivatives as,

$$u_1 = x_{3,t}, \quad u_2 = x_{1,t} \cos x_3 + x_{2,t} \sin x_3.$$

Since we have two integral constraints in this case, namely,

$$\begin{aligned}\Delta x_1(\theta) &= \int_0^T u_2 \cos x_3 dt = \int_0^T (x_{1,t} \cos x_3 + x_{2,t} \sin x_3) \cdot \cos x_3 dt \\ \Delta x_2(\theta) &= \int_0^T u_2 \sin x_3 dt = \int_0^T (x_{1,t} \cos x_3 + x_{2,t} \sin x_3) \cdot \sin x_3 dt,\end{aligned}$$

we invoke Lagrange multipliers $\lambda, \mu \in C^\infty(S^1; \mathbb{R})$ and the augmented Lagrangian density can be read as,

$$\begin{aligned}\mathcal{L} =& \frac{1}{2}\left[\left(x_{3,t}^2 + (x_{1,t} \cos x_3 + x_{2,t} \sin x_3)^2\right) + \chi\left(x_{3,t\theta}^2 + (x_{1,t\theta} \cos x_3 + x_{2,t\theta} \sin x_3)^2\right)\right] \\ &+ \lambda (x_{1,t} \cos x_3 + x_{2,t} \sin x_3) \cdot \cos x_3 + \mu (x_{1,t} \cos x_3 + x_{2,t} \sin x_3) \cdot \sin x_3.\end{aligned} \tag{4.83}$$

We recall the Euler-Lagrange equations from (4.22),

$$\frac{\partial \mathcal{L}}{\partial x_i} - \frac{\partial}{\partial \theta}\left(\frac{\partial \mathcal{L}}{\partial x_{i,\theta}}\right) - \frac{\partial}{\partial t}\left(\frac{\partial \mathcal{L}}{\partial x_{i,t}}\right) + \frac{\partial^2}{\partial \theta \partial t}\left(\frac{\partial \mathcal{L}}{\partial x_{i,\theta t}}\right) = 0,$$

for $i = 1, 2, 3$. We note the following quantities,

$$
\begin{aligned}
u_2 &= x_{1,t} \cos x_3 + x_{2,t} \sin x_3, \\
u_{2,\theta} &= x_{1,t\theta} \cos x_3 + x_{2,t\theta} \sin x_3, \\
\frac{\partial}{\partial t}\left(\frac{\partial \mathcal{L}}{\partial x_{1,t}}\right) &= u_{2,t} \cos x_3 - u_1 \left(u_2 \sin x_3 + \lambda \sin 2x_3 - \mu \cos 2x_3\right), \\
\frac{\partial^2}{\partial \theta \partial t}\left(\frac{\partial \mathcal{L}}{\partial x_{1,\theta t}}\right) &= \chi \left(u_{2,\theta\theta t} \cos x_3 - x_{3,\theta} \left(u_{2,\theta t} \sin x_3 + u_{2,\theta} u_1 \cos x_3\right)\right. \\
&\qquad \left. - \sin x_3 \left(u_{2,\theta\theta} u_1 + u_{2,\theta} u_{1,\theta}\right)\right), \\
\frac{\partial}{\partial t}\left(\frac{\partial \mathcal{L}}{\partial x_{2,t}}\right) &= u_{2,t} \sin x_3 + u_1 \left(u_2 \cos x_3 + \lambda \cos 2x_3 + \mu \sin 2x_3\right), \\
\frac{\partial^2}{\partial \theta \partial t}\left(\frac{\partial \mathcal{L}}{\partial x_{2,\theta t}}\right) &= \chi \left(u_{2,\theta\theta t} \sin x_3 + x_{3,\theta} \left(u_{2,\theta t} \cos x_3 - u_{2,\theta} u_1 \sin x_3\right)\right. \\
&\qquad \left. + \cos x_3 \left(u_{2,\theta\theta} u_1 + u_{2,\theta} u_{1,\theta}\right)\right), \\
\frac{\partial}{\partial t}\left(\frac{\partial \mathcal{L}}{\partial x_{3,t}}\right) &= u_{1,t}, \\
\frac{\partial^2}{\partial \theta \partial t}\left(\frac{\partial \mathcal{L}}{\partial x_{3,\theta t}}\right) &= \chi u_{1,\theta\theta t}.
\end{aligned}
$$

Subsequently, the Euler-Lagrange equations for the Lagrangian (4.83) take the form,

$$
\begin{aligned}
&u_{2,t} \cos x_3 - u_1 u_2 \sin x_3 - u_1 \left(\lambda \sin 2x_3 - \mu \cos 2x_3\right) \\
&\quad = \chi \left(u_{2,\theta\theta t} \cos x_3 - \sin x_3 \left(u_{2,\theta\theta} u_1 + u_{2,\theta} u_{1,\theta}\right) - x_{3,\theta} \left(u_{2,\theta t} \sin x_3 + u_{2,\theta} u_1 \cos x_3\right)\right), \\
&u_{2,t} \sin x_3 + u_1 u_2 \cos x_3 + u_1 \left(\lambda \cos 2x_3 + \mu \sin 2x_3\right) \\
&\quad = \chi \left(u_{2,\theta\theta t} \sin x_3 + \cos x_3 \left(u_{2,\theta\theta} u_1 + u_{2,\theta} u_{1,\theta}\right) + x_{3,\theta} \left(u_{2,\theta t} \cos x_3 - u_{2,\theta} u_1 \sin x_3\right)\right), \\
&u_{1,t} - \chi u_{1,\theta\theta t} = -u_2 \left(\lambda \sin x_3 - \mu \cos x_3 - \chi u_{2,\theta} x_{3,\theta}\right),
\end{aligned}
\tag{4.84}
$$

which after some readjustments yield,

$$\begin{aligned}
\frac{\partial}{\partial t}(1-\chi\Delta)u_1 &= -u_2\left(\lambda\sin x_3 - \mu\cos x_3 - \chi x_{3,\theta}u_{2,\theta}\right)\\
\frac{\partial}{\partial t}(1-\chi\Delta)u_2 &= u_1\left(\lambda\sin x_3 - \mu\cos x_3 - \chi x_{3,\theta}u_{2,\theta}\right)\\
\frac{\partial}{\partial t}\left(\lambda\sin x_3 - \mu\cos x_3 - \chi u_{2,\theta}x_{3,\theta}\right) &= -u_1(1-\chi\Delta)u_2.
\end{aligned} \tag{4.85}$$

Denoting $\mathcal{A} := (1-\chi\Delta)$ and $\mu_3 := \lambda\sin x_3 - \mu\cos x_3 - \chi u_{2,\theta}x_{3,\theta}$, we then can express (4.85) as,

$$\begin{aligned}
\frac{\partial}{\partial t}\mathcal{A}u_1 &= -\mu_3 u_2\\
\frac{\partial}{\partial t}\mathcal{A}u_1 &= \mu_3 u_1\\
\frac{\partial\mu_3}{\partial t} &= -u_1\mathcal{A}u_2.
\end{aligned} \tag{4.86}$$

4.6.1.2 PMP Approach

We introduce the costate variable $p(t) = (p_1(t), p_2(t), p_3(t)) \in C^\infty(S^1;\mathbb{R}^3),\ t \in [0,T]$. The pre-Hamiltonian (considering only normal extremals) can be written as,

$$\begin{aligned}
H &= \langle\dot{x}, p\rangle - L\\
&= \int_0^{2\pi}\left(u_2\left(p_1\cos x_3 + p_2\sin x_3\right) + u_1p_3 - \frac{1}{2}\left(u_1^2+u_2^2\right) - \frac{\chi}{2}\left(u_{1,\theta}^2+u_{2,\theta}^2\right)\right)d\theta.
\end{aligned} \tag{4.87}$$

Remark 4.6. Here we only consider normal extremals, i.e. when $p_0 \neq 0$ and can be normalized to -1. Note that in this case, the emptiness (i.e. the full costate being identically zero) of the PMP would not occur. It is of future effort to investigate whether the finite codimensionality condition is satisfied in the SE(2) case.

The maximum principle (Theorem 4.4.1) would require us to maximize (4.87) pointwise over the controls, i.e. we are attempting to find the Hamiltonian as,

$$\begin{aligned}\mathcal{H} &= \sup_{v_1,v_2\in C^\infty(S^1;\mathbb{R})} H \\ &= \sup_{v_1,v_2\in C^\infty(S^1;\mathbb{R})} \int_0^{2\pi} \Big(v_2\left(p_1\cos x_3 + p_2 \sin x_3\right) + v_1 p_3 \\ &\qquad -\frac{1}{2}\left(v_1^2+v_2^2\right) - \frac{\chi}{2}\left(v_{1,\theta}^2 + v_{2,\theta}^2\right)\Big)\, d\theta \end{aligned} \tag{4.88}$$

This maximization results in two Euler-Lagrange equations,

$$\frac{\partial H}{\partial v_i} - \frac{\partial}{\partial \theta}\left(\frac{\partial H}{\partial v_{i,\theta}}\right) = 0, \quad i = 1,2, \tag{4.89}$$

that yields the optimal controls,

$$\begin{aligned} \mathcal{A}u_1 &= p_3, \\ \mathcal{A}u_2 &= p_1\cos x_3 + p_2 \sin x_3, \end{aligned} \tag{4.90}$$

where we denote $\mathcal{A} = (1-\chi\Delta)$, as usual. The Hamiltonian can be read as,

$$\begin{aligned}\mathcal{H} &= \frac{1}{2}\int_0^{2\pi} \left(u_1\mathcal{A}u_1 + u_2\mathcal{A}u_2\right) d\theta \\ &= \frac{1}{2}\int_0^{2\pi} \left(p_3\mathcal{A}^{-1}p_3 + \left(p_1\cos x_3 + p_2\sin x_3\right)\mathcal{A}^{-1}\left(p_1\cos x_3 + p_2\sin x_3\right)\right) d\theta \end{aligned} \tag{4.91}$$

The dynamics of the costate variable p can be calculated from Hamilton's equation, $\frac{\partial p}{\partial t} = -\frac{\delta \mathcal{H}}{\delta x}$, where $\frac{\delta \mathcal{H}}{\delta x}$ denotes the functional derivative of $\mathcal{H}$ with respect to x. Explicit calculations yield,

$$\begin{aligned} \frac{\partial p_1}{\partial t} &= 0 \\ \frac{\partial p_2}{\partial t} &= 0 \\ \frac{\partial p_3}{\partial t} &= -u_2\left(-p_1\sin x_3 + p_2\cos x_3\right). \end{aligned} \tag{4.92}$$

If we denote $\mu_3 := -p_1 \sin x_3 + p_2 \cos x_3$, then from (4.90) and (4.92), we can rediscover (4.86). Renaming $\mu_i = \mathcal{A}u_i,\ i = 1, 2$, (4.86) can also be written as,

$$\begin{aligned} \frac{\partial \mu_1}{\partial t} &= -\mu_3 \mathcal{A}^{-1} \mu_2 \\ \frac{\partial \mu_2}{\partial t} &= \mu_3 \mathcal{A}^{-1} \mu_1 \\ \frac{\partial \mu_3}{\partial t} &= -\mu_2 \mathcal{A}^{-1} \mu_1. \end{aligned} \tag{4.93}$$

4.6.2 Strong Coupling Limit, $\chi \to \infty$

Similar to the Heisenberg case, it can be shown that synchronization is achieved in strong coupling limit in this case as well. We know that for some $z \in C^\infty(S^1; \mathbb{R})$, we have $\lim_{\chi \to \infty} \mathcal{A}^{-1} z = \int_0^{2\pi} z d\theta$. Thus, we may rewrite (4.93) in the strong coupling limit as,

$$\begin{aligned} \frac{\partial \mu_1}{\partial t} &= -\mu_3 \left(\int_0^{2\pi} \mu_2 d\theta \right) \\ \frac{\partial \mu_2}{\partial t} &= \mu_3 \left(\int_0^{2\pi} \mu_1 d\theta \right) \\ \frac{\partial \mu_3}{\partial t} &= -\mu_2 \left(\int_0^{2\pi} \mu_1 d\theta \right). \end{aligned} \tag{4.94}$$

If we define the variables,

$$\alpha_i = \int_0^{2\pi} \mu_i d\theta, \quad i = 1, 2, 3, \tag{4.95}$$

then these variables will evolve according to,

$$\begin{aligned} \dot{\alpha}_1 &= -\alpha_2 \alpha_3 \\ \dot{\alpha}_2 &= \alpha_1 \alpha_3 \\ \dot{\alpha}_3 &= -\alpha_1 \alpha_2. \end{aligned} \tag{4.96}$$

Equations (4.96) are the equations for a single agent scenario and they are studied in detail in Section 3.2. This indicates the synchronization phenomenon in the planar continuum flock. Note that α_1 and α_2 are essentially the optimal controls u_1 and u_2, respectively. The Hamiltonian (4.88) simply becomes,

$$h_\infty = \frac{1}{2}\left(\alpha_1^2 + \alpha_2^2\right). \tag{4.97}$$

4.6.3 Simulation Results

While it has not been possible to characterize general solutions of (4.93) analytically, here we demonstrate numerical solutions. To numerically solve the evolution equations of μ_i variables, we used a finite difference method. We partitioning the space domain $[0, 2\pi]$ uniformly in M points, $0 = \theta_1, \ldots, \theta_M = 2\pi$, so that the difference between two consecutive space points become $\delta\theta = \frac{2\pi}{M}$. In this discrete setting any $z(t, \theta)$ can be approximated as an M vector, $z(t, \theta) \approx z(t) = [z_1(t), z_2(t), \ldots, z_M(t)]^T$ with the constraint $z_1(t) = z_M(t)$ for all t to respect the periodicity property. Note also that in a second-order central difference scheme, the double partial space derivative is expressed as,

$$\frac{\partial^2 z(t, \theta_j)}{\partial \theta^2} = \frac{z_{j+1} - 2z_j + z_{j-1}}{\delta\theta^2},$$

for $j = 1, \ldots, M$ with appropriate adjustments for the boundary points $j = 1, M$. The linear operator $\mathcal{A} = (1 - \chi\Delta)$ can then be expressed by the $M \times M$ nonsingular

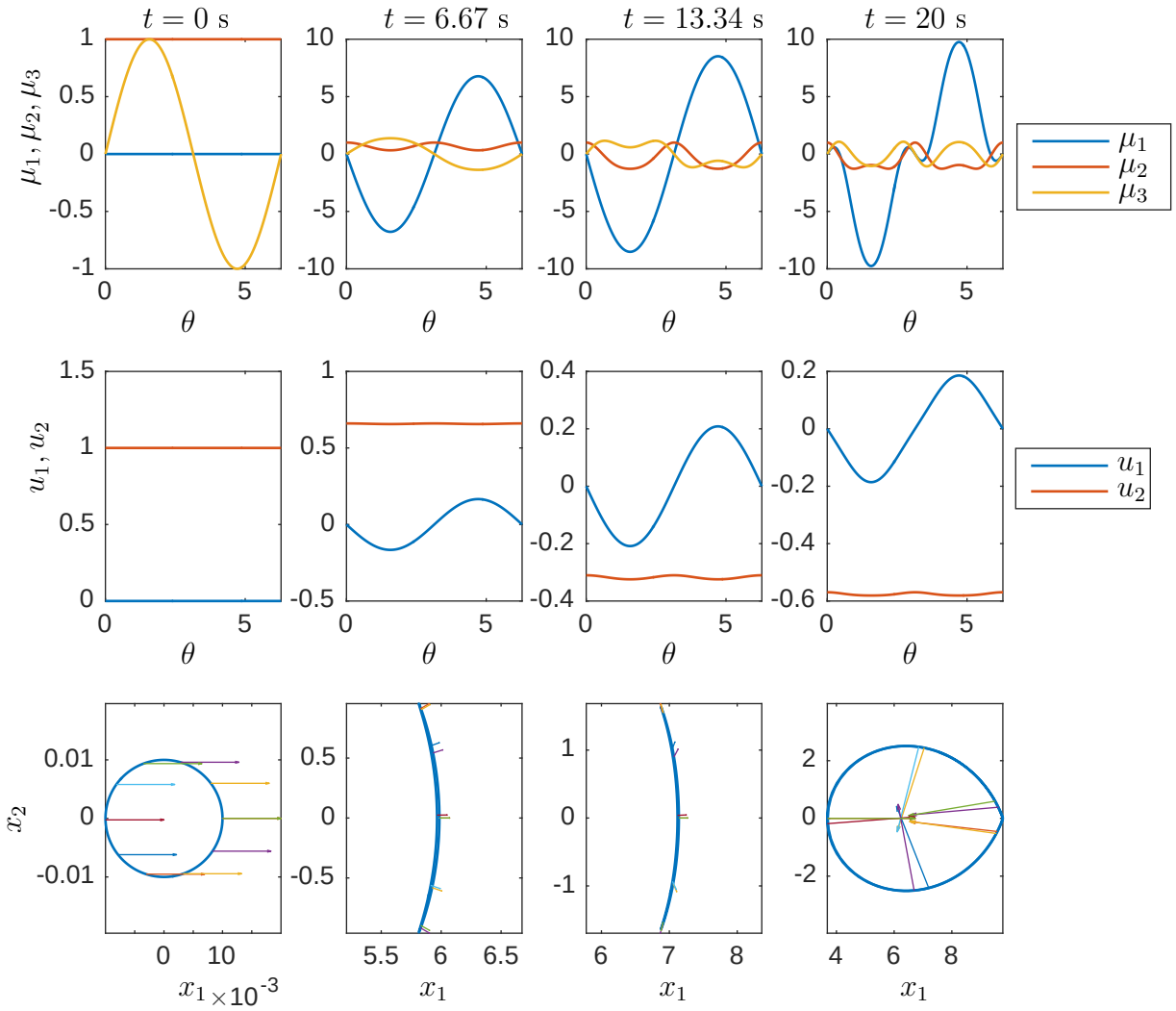

Figure 4.6: Numerical solution of (4.99) (first two rows) along with the state evolution (third row) for experiment 1. The arrows represent the direction of movement of the particle at that point.

matrix A_M,

$$A_M = \begin{pmatrix} 1+\left(\frac{2\chi}{\delta\theta^2}\right) & -\left(\frac{\chi}{\delta\theta^2}\right) & 0 & \dots & -\left(\frac{\chi}{\delta\theta^2}\right) & 0 \\ -\left(\frac{\chi}{\delta\theta^2}\right) & 1+\left(\frac{2\chi}{\delta\theta^2}\right) & -\left(\frac{\chi}{\delta\theta^2}\right) & 0 & \dots & 0 \\ 0 & -\left(\frac{\chi}{\delta\theta^2}\right) & 1+\left(\frac{2\chi}{\delta\theta^2}\right) & -\left(\frac{\chi}{\delta\theta^2}\right) & \dots & 0 \\ \vdots & \vdots & & \ddots & & \vdots \\ 0 & -\left(\frac{\chi}{\delta\theta^2}\right) & \dots & 0 & -\left(\frac{\chi}{\delta\theta^2}\right) & 1+\left(\frac{2\chi}{\delta\theta^2}\right) \end{pmatrix}. \quad (4.98)$$

With this notation, the partial differential equations (4.93) can be expressed as a system of ordinary differential equations (ODE),

$$\begin{aligned} \dot{\mu_1} &= -\mu_3 A_M^{-1} \mu_2 \\ \dot{\mu_2} &= \mu_3 A_M^{-1} \mu_1 \\ \dot{\mu_3} &= -\mu_2 A_M^{-1} \mu_1. \end{aligned} \tag{4.99}$$

These ODEs (4.99) are then solved using a mid-point based ODE solver in MATLAB. The optimal controls u_i's can be derived from the μ variables by the relation, $u_i = A_M^{-1}\mu_i, i = 1, 2$ which are used in the quadrature of the state variables x_j's. Here we present results of some experiments with varying initial conditions. The final time T and space discretization factor M is kept fixed at $T = 20$ seconds and $M = 128$ for all the experiments. A high value of M is chosen for a faithful calculation of the spatial derivatives. In the subsequent experiments we try to investigate the behavior of a simple loop under the optimal controls generated by (4.99), i.e. we take, $x_1(0, \theta) = 0.01\cos(\theta)$ and $x_2(0, \theta) = 0.01\sin(\theta)$ so that initially the particles start on a circle. The remaining initial conditions of x_3 and μ_i variables and the parameter χ is varied in the following experiments. It is to be noted that the Hamiltonian and the Casimir variables are validated to be constant in each of the experiments.

Experiment 1

We take a simple example where each agent start moving in the positive x axis and with unit speeds, i.e. $x_3(0, \theta) = 0, \mu_2(0, \theta) = 1$. The initial curvature of each

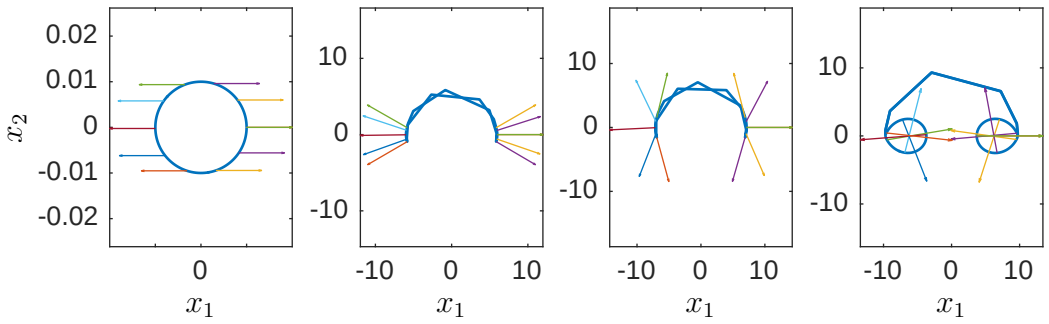

Figure 4.7: State evolution is only shown for experiment 2. The arrows represent the direction of movement of the particle at that point.

agent is taken to be zero, $\mu_1(0,\theta) = 0$ which means every agent starts harmoniously with same velocity and curvature. The value of χ is taken as 1. Four snapshots of the μ, u and x variables are shown in Fig. 4.6. The curvature field is seen to be forming two peaks in the spatial domain which gives rise to the twisted form of the initial circle.

Experiment 2

We keep all the initial conditions same as in experiment 1 except the initial direction of movement of the particles. It is simulated that almost half the particles try to go in one direction while the other half in the opposite direction. To write this as a continuous periodic function, we take

$$x_3(0,\theta) = \begin{cases} \frac{\pi}{2}\left(1+\tanh\left(100\left(\theta-\frac{\pi}{2}\right)\right)\right), & \text{if } 0 \le \theta < \pi \\ \\ \frac{\pi}{2}\left(1-\tanh\left(100\left(\theta-\frac{3\pi}{2}\right)\right)\right), & \text{if } \pi \le \theta \le 2\pi \end{cases} . \tag{4.100}$$

This definition of the initial direction means that the particles on the 'east' part of the circle initially go to the right and the particles on the 'west' part go to the left. The simulation results are shown in Fig. 4.7. Comparing to Fig. 4.6,

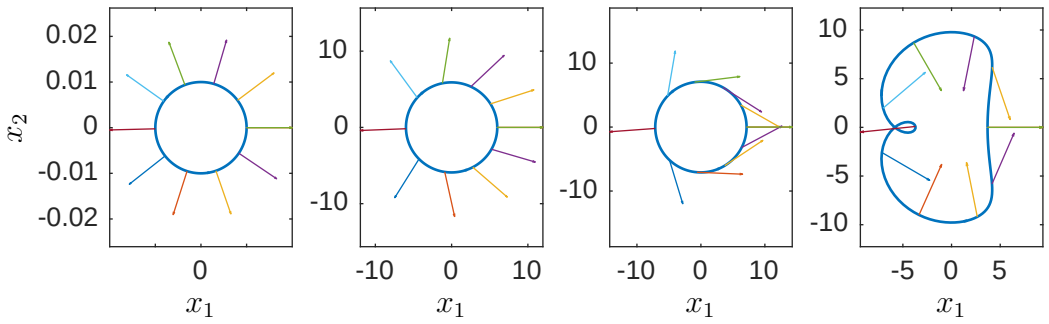

Figure 4.8: State evolution is only shown for experiment 3. The arrows represent the direction of movement of the particle at that point.

the first two rows are identical since the initial conditions of μ variables did not change and hence they are omitted. What is interesting is that the circle splits into two loops connected by very small number of particles.

Experiment 3

Similar to experiment 2, we try to investigate the effect of change in initial direction of movement of the particles. Here, we set the particles to go on a radially outward path, i.e. $x_3(0,\theta) = \theta$, with keeping all other conditions same as in experiment 2. The simulation results are shown in Fig. 4.8. The first two rows are not shown since they are identical with experiment 1.

Experiment 4

In this experiment, again we fix all the initial conditions and parameters same as in experiment 1, except the initial curvature is given a local intensity. In other words we choose this Gaussian function,

$$\mu_1(0,\theta) = \frac{1}{\sqrt{2\pi\sigma^2}} e^{-\frac{(\theta-\pi)^2}{2\sigma^2}}, \tag{4.101}$$

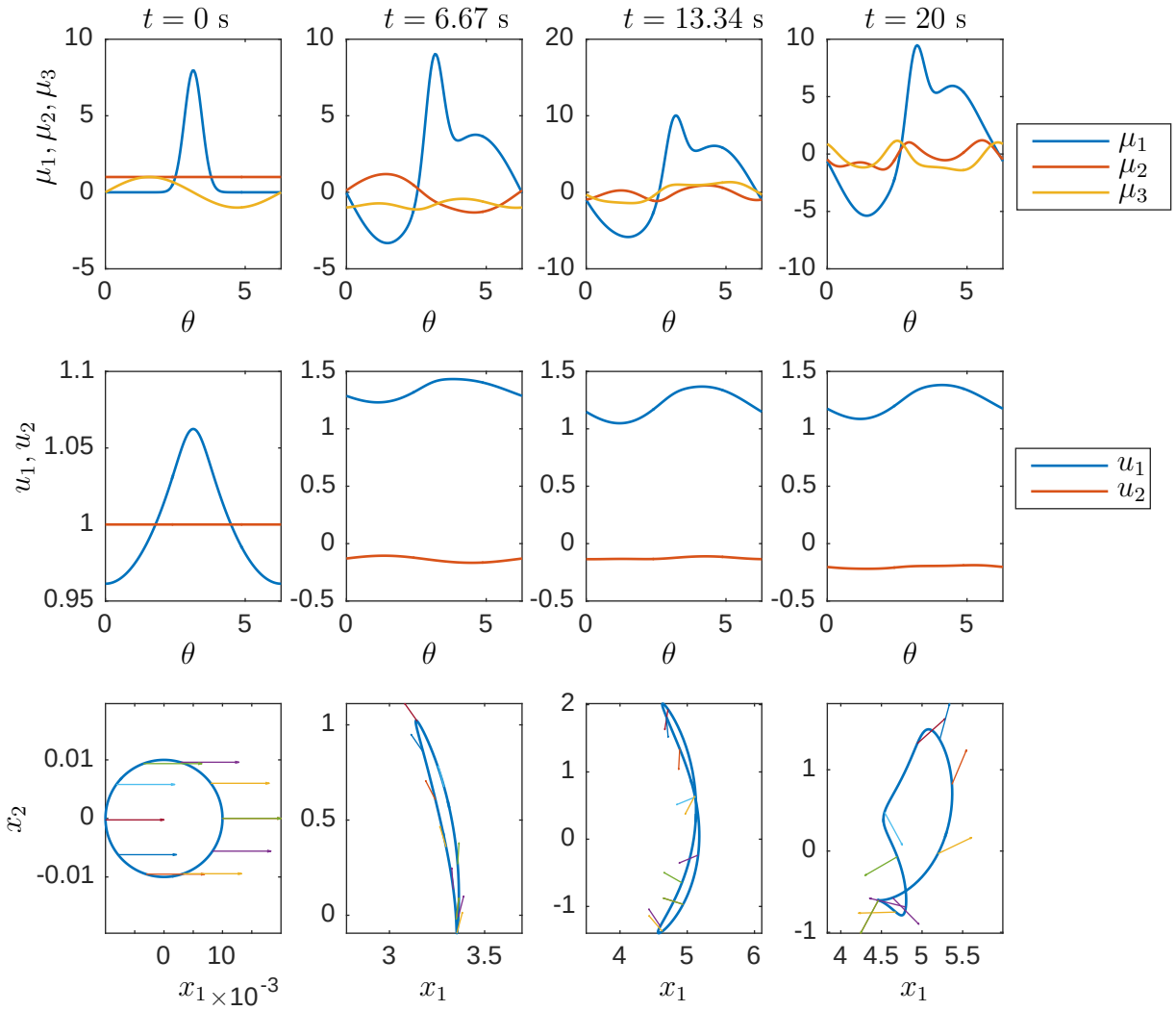

Figure 4.9: Numerical solution of (4.99) (first two rows) along with the state evolution (third row) for experiment 4. The arrows represent the direction of movement of the particle at that point.

with $\sigma = 0.05$. The purpose of choosing this initial condition is to see whether a localized information gets spread across the continuum or not. The simulation results are shown in Fig. 4.9.

Experiment 5

Finally, we demonstrate the effect of strong coupling limit by taking a large value

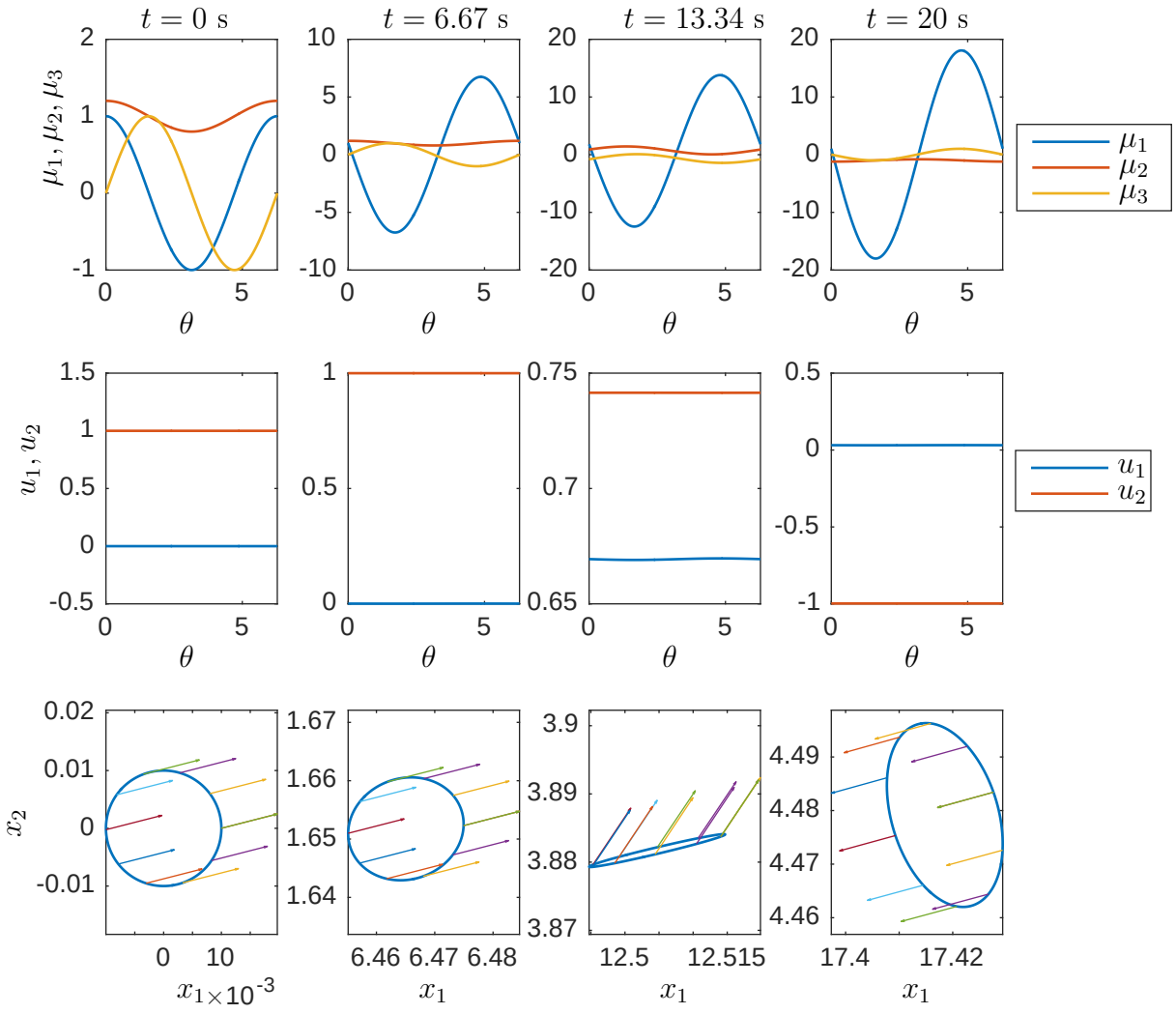

Figure 4.10: Numerical solution of (4.99) (first two rows) along with the state evolution (third row) for experiment 5. The arrows represent the direction of movement of the particle at that point. The u_1, u_2 solutions are almost 'flat', indicating single agent solution or synchronization.

of $\chi = 1000$. We note that even in the case, $\mu_1(0,\theta) = \cos(\theta), \mu_2(0,\theta) = 1 + 0.2\cos(\theta), \mu_3(0,\theta) = \sin(\theta), x_3(0,\theta) = \pi/4$, we essentially get the system derived by the optimal controls that are spatially non varying.

4.7 Discussion and Scope of Future Research

In this chapter, we have presented a general framework for a continuum description of a flock. We are interested in solving optimal control problems to explain collective movement of such a flock. We recognize this is a challenging problem that naturally provides several open questions for further research. We itemize few such possibilities.

- It is shown that under a certain finite codimensionality of a reachable set, the PMP remains valid in a general Hilbert space setting. One might want to discover its relationship with the controllability condition. In particular, if a system on the loop group is strongly controllable, does the PMP condition satisfy automatically? We have been able to show this to be true in the Heisenberg case. Does this remain valid if we only have weak controllability?

- It is of interest to extract meaningful features of the optimal solutions of the SE(2) case. While we have not been able to solve (4.93) analytically, we want to answer few questions about it. For example, do these equations possess a traveling wave like solution (like the Heisenberg case)? If so, what is the speed of those waves? The answer might give an insight toward the information transfer in biological swarms. It is the inherent nature of the numerical study presented here that there exist many possibilities by varying initial configurations which makes it particularly difficult. We explored only a tiny fraction of possible variations in the initial configurations in this

document. A future work could perform more extensive numerical study of these partial differential equations (4.93).

- We have presented the results in this chapter under the case of a fixed cyclic interaction topology. A more general, possibly state dependent (hence time dependent, too) interaction scheme can be modeled and subjected under similar questions.

- It will be an interesting future work to establish continuum parallel of the Lie-Poisson reduction in the loop group case.

Chapter 5

Cognitive Cost of Flocking: A Geometric and Hamiltonian Perspective

5.1 Introduction

It has been an appealing question to researchers from several fields to address how natural collectives function at a fundamental level. Many theories have been proposed to describe this phenomenon over the past few decades. The lack of accurate motion capturing technologies had limited the study of natural collectives for many years. However, as motion capture became more sophisticated, more movement data of these collectives were recorded. This enabled researchers to uncover several underlying mechanisms behind flocking [Ballerini et al., 2008a,b; Attanasi et al., 2014; Cavagna et al., 2018; Nagy et al., 2010]. These studies shed light on how individual agents interact with its neighboring agents or how information may be propagated through the flock.

Continuing the spirit of the 'top-down' view of the flock, we will present a novel perspective for analyzing collective motion data. The flock movement results in a time-series of its kinetic energy, which can be divided into several *energy modes*. Normalized modes define a curve in some appropriate dimensional simplex which we attempt to describe by an evolutionary game dynamics. Individual energy modes are considered as pure strategies of such a game. An optimal control problem is proposed to best fit the data on the simplex, where the control inputs modulate the fitness associated with the strategies. This is in contrast to the optimal control problem posed in Chapter 4, where the controls are 'low-level' i.e. individual control inputs are determined post-solution of the optimal control problem. In the present context however, the control inputs are 'high-level'. The collective itself is thought to be deciding the optimal allocation of its energy among several different modes during a flight event. A notion of *cognitive cost* is introduced to denote the optimal cost for the collective to perform this allocation.

This work brings together several key ingredients for this data-driven approach. In section 5.2, the motion data of European flocks is detailed. This data is then subjected to a linear data smoothing technique [Dey and Krishnaprasad, 2012] that reconstructs smooth trajectory data of each bird in the flock. A nonlinear data smoothing technique [Dey and Krishnaprasad, 2014] is later used for the optimal energy allocation problems. These smoothing techniques are based on optimal control theory and are described in section 5.3. Section 5.4 contains the geometric theory developed in [Mischiati and Krishnaprasad, 2017] to compute

different energy modes. Finally, in section 5.5, a generative model based on [Raju and Krishnaprasad, 2018] is described to construct an optimal control problem on a simplex. Numerical solution of this optimal control problem, as well as the idea of cognitive cost, are presented in section 5.6. This is a joint work with V. Raju [Halder et al., 2019b].

5.2 Flocking Data

We are provided with flight data of European starlings that were taken by Dr. Andrea Cavagna and his collaborators from the Collective Behaviour in Biological Systems (COBBS) group at the Institute for Complex Systems (ISC-CNR), University of Rome “La Sapienza". Starlings gather around urban areas during the winter months in order to get extra warmth from the cities. Flocks of these kind of birds are well known to perform remarkable maneuvers, the purpose and mechanisms of which still elude researchers. Equipped with modern imaging techniques and sophisticated algorithms for stereo reconstruction, these group of researchers managed to capture a series of flight events with different flock sizes in the winter months of 2011. See [Attanasi et al., 2014] for more details about the process. We will study eight particular flocking events, the details of which are given in table 5.1.

Flocking Event	Flock Size (n)	Duration (seconds)	Data Capture Rate (frames/second)
1	175	5.4875	80
2	123	1.8176	170
3	46	5.6118	170
4	485	2.3471	170
5	104	3.8824	170
6	122	4.1588	170
7	380	5.7353	170
8	194	1.7588	170

Table 5.1: Details of captured flocking events

5.3 Data Smoothing

Given a time-indexed sequence of sampled observations on a manifold, generative models provide a meaningful way of capturing them through the use of an underlying dynamical system complete with control inputs having useful interpretations. The control inputs are determined by solving an optimal control problem, where the cost function consists of a fitness term that penalizes mismatch between the generated trajectory and sampled data, and a smoothing term weighted by a parameter λ that affects the smoothness of the generated trajectory. We discuss two generative models that have been proposed to solve this problem.

5.3.1 A linear generative model

A first approach to solving the data smoothing problem, presented in [Dey and Krishnaprasad, 2012], is to formulate an optimal control problem to minimize the jerk path integral, with intermediary state costs determining the fit error. Suppose that $\{\mathbf{r}_i\}_{i=0}^{N}$ denote the positions of the birds at each sampling time, with $\mathbf{r}_i \in \mathbb{R}^3$. In order to recover a trajectory fit $\mathbf{r}(t) : [t_0, t_N] \to \mathbb{R}^3$, one can use the jerk-driven linear generative model,

$$\begin{aligned} \dot{\mathbf{r}}(t) &= \mathbf{v}(t) \\ \dot{\mathbf{v}}(t) &= \mathbf{a}(t) \\ \dot{\mathbf{a}}(t) &= \mathbf{u}(t) \end{aligned} \tag{5.1}$$

where $\mathbf{v}(t), \mathbf{a}(t), \mathbf{u}(t)$ denote the velocity, acceleration and jerk (input) of the trajectory. The cost functional to be minimized is

$$J_l = \sum_{i=0}^{N} ||\mathbf{r}(t_i) - \mathbf{r}(t)||^2 + \lambda \int_{t_0}^{t_N} ||\mathbf{u}(t)||^2 dt \tag{5.2}$$

where the minimization is over initial conditions $\mathbf{r}(t_0), \mathbf{v}(t_0), \mathbf{a}(t_0)$ and the input $\mathbf{u}(t)$. Defining the state and output as

$$\mathbf{x}(t) = \begin{bmatrix} \mathbf{r}(t) \\ \mathbf{v}(t) \\ \mathbf{a}(t) \end{bmatrix} \in \mathbb{R}^9, \mathbf{y}(t) = \mathbf{x}(t) \in \mathbb{R}^3$$

we obtain the linear state equations

$$\dot{\mathbf{x}}(t) = A\mathbf{x}(t) + B\mathbf{u}(t)$$

$$\mathbf{y}(t) = C\mathbf{x}(t), \quad \text{where}$$

$$A = \begin{bmatrix} 0 & \mathbb{1}_3 & 0 \\ 0 & 0 & \mathbb{1}_3 \\ 0 & 0 & 0 \end{bmatrix}, \; B = \begin{bmatrix} 0 \\ 0 \\ \mathbb{1}_3 \end{bmatrix}, \; C = [\mathbb{1}_3 \;\; 0 \;\; 0] \tag{5.3}$$

Therefore, the problem of minimizing J_l subject to (5.3) is a linear, quadratic optimal control problem, which can be solved by a completion of squares of terms in the cost by invoking a path independence lemma, or by applying the Pontryagin Maximum Principle as shown in [Dey and Krishnaprasad, 2012]. This approach has been used to smooth the starling flock data for all the events listed in table 5.1.

5.3.2 Data smoothing in the Euclidean setting

In this section, we present a general result on the Pontyagin Maximum Principle based approach for data smoothing on the Euclidean space $\mathbb{R}^n$. Suppose that $\left\{x_i^d\right\}_{i=0}^N$ denote the sampled data. For a generative model given by the dynamics $\dot{x} = f(x,u)$ on $\mathbb{R}^n$, with the control $u \in \mathbb{R}^m$, the optimal control problem can be formulated as:

$$\min_{x(t_0),\; u\in\mathbb{R}^m} J(x(t_0),u) = \frac{\lambda}{2}\int_{t_0}^{t_N} \|u\|^2\, dt + \sum_{i=0}^{N} F_i(x(t_i), x_i^d), \tag{5.4}$$

$$\text{subject to: } \; \dot{x} = f(x,u),$$

where parameter $\lambda > 0$ is a regularization parameter, and F_i's are suitably defined *fit errors* of the reconstructed trajectories and sampled data at the sampling times. Using Pontryagin's Maximum Principle, the optimal control values can be calculated as a function of the state and a co-state variable. The following result from [Dey and Krishnaprasad, 2014] states this precisely.

Theorem 5.3.1. *(PMP for data smoothing [Dey and Krishnaprasad, 2014]) Let* $u^*(\cdot)$ *be an optimal control input for* (5.28)*, and let* $x^*(\cdot)$ *denote the corresponding state trajectory. Then there exist a costate trajectory* $p : [t_0, t_N] \to \mathbb{R}^n, p \neq 0$ *, such that*

$$\begin{aligned} \dot{x}^* &= \frac{\partial \mathcal{H}}{\partial p}(t, x^*, p, u^*) \\ \dot{p} &= -\frac{\partial \mathcal{H}}{\partial x}(t, x^*, p, u^*) \end{aligned} \tag{5.5}$$

during $t \in (t_i, t_{i+1})$*,* $i = 0, 1, ..., N-1$*, and the Hamiltonian is given as*

$$\mathcal{H}(t, x^*, p, u^*) = \max_{v \in \mathbb{R}^m} H(t, x^*, p, v), \tag{5.6}$$

for $t \in [t_0, t_N] \backslash \{t_0, t_1, ..., t_N\}$*, where the pre-Hamiltonian is defined as* $H(t, x, p, u) = \langle p, f(x, u) \rangle - \frac{\lambda}{2} \|u\|^2$*. Moreover, jump discontinuities of the costate variable can be written as*

$$\begin{aligned} & p(t_0^-) = 0, \\ & p(t_i^+) - p(t_i^-) = \frac{\partial F_i(x(t_i))}{\partial x(t_i)}, \quad i = 0, 1, ..., N, \\ & p(t_N^+) = 0. \end{aligned} \tag{5.7}$$

The piecewise continuous nature of the co-state trajectory due to jump conditions arising from mismatch between the sampled data points and the recon-

structed state must be noted here. The initial condition $x(t_0)$ is identified by using the terminal condition for the co-state, while the optimal value of λ is typically obtained through leave-one-out or ordinary cross validation. The reconstructed trajectory is then obtained as the projection onto the state space of the solution of Hamilton's equations derived from the (maximized pre-) Hamiltonian. We refer the reader to [Dey, 2015] for a detailed treatment of these problems. This is the result that we will use in our data fitting problem on a simplex.

5.4 Energy Modes

Avian flocks display a variety of flight behaviors that may be characterized as collective strategies such as steady directed translation of center of mass (which we denote by *com*), coherent rotation about center of mass (*rot*), change of form (*ens*), internal re-shuffling of relative positions (*dem*), rapid expansion or contraction of volume (*vol*) etc. A flocking event may display all of the mentioned strategies to varying degrees as governed by the time-dependent allocation of kinetic energy to each strategy. We take the viewpoint presented in [Mischiati and Krishnaprasad, 2017] and study the fractions of the total kinetic energy of a flock allocated to several 'kinematic modes' – rigid translations, rigid rotations, inertia tensor transformations, expansion and compression, in order to describe collective behavior.

If the positions of the birds in a flock are denoted by $\{\mathbf{r}_1, \mathbf{r}_2, ..., \mathbf{r}_n\}$, the center

of mass can be written as,

$$\mathbf{r}_{\mathbf{com}} = \frac{1}{n}\sum_{i=1}^{n}\mathbf{r}_i, \tag{5.8}$$

where we treat every bird alike, i.e. their masses are taken to be equal. The *ensemble inertia tensor* is defined by

$$K = \sum_{i=1}^{n}\left(\mathbf{r}_i - \mathbf{r}_{\mathbf{com}}\right)\left(\mathbf{r}_i - \mathbf{r}_{\mathbf{com}}\right)^{\mathsf{T}}. \tag{5.9}$$

Let the velocities of the birds be denoted as, $\{\mathbf{v}_{\mathbf{r}1}, ..., \mathbf{v}_{\mathbf{r}n}\}$, then the total kinetic energy is,

$$E = \frac{1}{2}\sum_{i=1}^{n}\left\|\mathbf{v}_{\mathbf{r}i}\right\|^2. \tag{5.10}$$

We can define the position and velocity vector with respect to the center of mass, i.e. $\mathbf{c} \triangleq [\mathbf{c}_1, ..., \mathbf{c}_n] \in \mathbb{R}^{3\times n}$, where $\mathbf{c}_i = \mathbf{r}_i - \mathbf{r}_{\mathbf{com}}$; $\mathbf{v}_{\mathbf{c}} \triangleq [\mathbf{v}_{\mathbf{c}1}, \mathbf{v}_{\mathbf{c}2}, ..., \mathbf{v}_{\mathbf{c}n}] \in \mathbb{R}^{3\times n}$, where $\mathbf{v}_{\mathbf{c}i} = \mathbf{v}_{\mathbf{r}i} - \mathbf{v}_{\mathbf{com}}$. Then,

$$E_{\text{com}} = \frac{n}{2}\left\|\mathbf{v}_{\mathbf{com}}\right\|^2, \quad E_{\text{rel}} \triangleq \frac{1}{2}\sum_{i=1}^{n}\left\|\mathbf{v}_{\mathbf{c}i}\right\|^2. \tag{5.11}$$

We thus have the splitting, $E = E_{\text{com}} + E_{\text{rel}}$. As presented in [Mischiati and Krishnaprasad, 2017], instantaneous relative energy allocations can be expressed on a probability simplex (Δ^4)[1] by exploiting the fiber bundle structures of the flock's total configuration space to split the total kinetic energy using (i) ensemble fibration or (ii) shape fibration.

(i) *Ensemble Fibration*: We note that the ensemble inertia tensor K (5.9) is a symmetric positive definite matrix. Hence its eigendecomposition can be

[1]Note that in this chapter we will use Δ^n to denote the n-dimensional simplex.

written as, $K = Q\Lambda Q^{\mathsf{T}}$, with $\Lambda = \mathrm{diag}(\lambda_1, \lambda_2, \lambda_3)$, where $\lambda_1 \geq \lambda_2 \geq \lambda_3 > 0$. Define, $F := \mathbf{c}\mathbf{v}_{\mathbf{c}}^{\mathsf{T}} + \mathbf{v}_{\mathbf{c}}\mathbf{c}^{\mathsf{T}}$ and $\tilde{F} = [\tilde{F}_{ij}] = Q^{\mathsf{T}} F Q$. Then the following energy modes can be calculated,

$$\begin{aligned} E_{\text{ens.rot}} &\triangleq \frac{1}{2}\left(\frac{\tilde{F}_{12}^2}{\lambda_1+\lambda_2} + \frac{\tilde{F}_{13}^2}{\lambda_1+\lambda_3} + \frac{\tilde{F}_{23}^2}{\lambda_2+\lambda_3}\right) \\ E_{\text{ens.def}} &\triangleq \frac{1}{8}\left(\frac{\tilde{F}_{11}^2}{\lambda_1} + \frac{\tilde{F}_{22}^2}{\lambda_2} + \frac{\tilde{F}_{33}^2}{\lambda_3}\right). \end{aligned} \tag{5.12}$$

Furthermore,

$$E_{\text{vol}} \triangleq \frac{1}{2}\frac{\mathrm{tr}^2\left(\mathbf{c}\mathbf{v}_{\mathbf{c}}^{\mathsf{T}}\right)}{\mathrm{tr}(K)}, \tag{5.13}$$

so that, $E_{\text{ens.res}} = E_{\text{ens.def}} - E_{\text{vol}}$. We may also calculate $E_{\text{dem}} = E_{\text{rel}} - E_{\text{ens.rot}} - E_{\text{ens.def}}$. Hence, in this fibration we have the following splitting of the kinetic energy,

$$\left\{\frac{E_{\text{com}}}{E}, \frac{E_{\text{dem}}}{E}, \frac{E_{\text{ens.rot}}}{E}, \frac{E_{\text{vol}}}{E}, \frac{E_{\text{ens.res}}}{E}\right\} \in \Delta^4 \tag{5.14}$$

(i) *Shape Fibration*: Define

$$\begin{aligned} \mathbf{J} &= \sum_{i=1}^{n} \left(\mathbf{c}_i \times \mathbf{v}_{\mathbf{c}i}\right), \\ I_{\mathbf{c}} &= \sum_{i=1}^{n} \left(\|\mathbf{c}_i\|^2 \mathbb{1} - \mathbf{c}_i\mathbf{c}_i^{\mathsf{T}}\right). \end{aligned} \tag{5.15}$$

Then the rotational energy E_{rot} can then be calculated as,

$$E_{\text{rot}} \triangleq \frac{1}{2}\mathbf{J}^{\mathsf{T}} I_{\mathbf{c}}^{-1} \mathbf{J}, \tag{5.16}$$

The shape residual energy is given by $E_{\text{shp.res}} = E_{\text{rel}} - E_{\text{rot}} - E_{\text{end.def}}$, which provides the splitting in this fibration as below

$$\left\{\frac{E_{\text{com}}}{E}, \frac{E_{\text{rot}}}{E}, \frac{E_{\text{shp.res}}}{E}, \frac{E_{\text{vol}}}{E}, \frac{E_{\text{ens.res}}}{E}\right\} \in \Delta^4 \tag{5.17}$$

While we can split the kinetic energy in 5 different modes (5.14),(5.17), many flocking events show a predominant allocation of nearly constant energy of rigid translation (E_{com}). We exclude this component from the total E in our analysis, and consider the allocation of the remaining energy E_{rel} to obtain a time dependent trace of each event on a lower dimensional simplex. In particular, we capture the trace generated by the following decomposition of E_{rel} using ensemble fibration on the 1-simplex by two different methods,

$$\text{(ENS-I)} \qquad \left\{ \frac{E_{\text{dem}}}{E_{\text{rel}}}, \frac{E_{\text{ens}}}{E_{\text{rel}}} \right\} \in \Delta^1, \tag{5.18}$$

$$\text{(ENS-II)} \qquad \left\{ \frac{E_{\text{ens.rot}}}{E_{\text{rel}}}, \frac{E_{\text{rel}} - E_{\text{ens.rot}}}{E_{\text{rel}}} \right\} \in \Delta^1, \tag{5.19}$$

where $E_{\text{rel}} = E - E_{\text{com}}$, and $E_{\text{ens}} = E_{\text{rel}} - E_{\text{dem}} = E_{\text{ens.rot}} + E_{\text{vol}} + E_{\text{ens.res}}$. Similarly, a one dimensional simplex description using shape fibration may be given by two ways,

$$\text{(SHP-I)} \qquad \left\{ \frac{E_{\text{shp.res}}}{E_{\text{rel}}}, \frac{E_{\text{rel}} - E_{\text{shp.res}}}{E_{\text{rel}}} \right\} \in \Delta^1, \tag{5.20}$$

$$\text{(SHP-II)} \qquad \left\{ \frac{E_{\text{rot}}}{E_{\text{rel}}}, \frac{E_{\text{shp}}}{E_{\text{rel}}} \right\} \in \Delta^1, \tag{5.21}$$

where $E_{\text{shp}} = E_{\text{rel}} - E_{\text{rot}} = E_{\text{shp.res}} + E_{\text{vol}} + E_{\text{ens.res}}$.

In this way, moment-to-moment decisions made by individuals in a flock, taking account of the decisions of their neighbors, contribute to flock-scale strategies as captured by such time dependent traces on the probability simplex. Treating the strategy prevalence as being given by the respective energy fractions, we resort to a generative evolutionary game dynamics to model the competition between the flock-scale strategies.

5.5 Generative model on the 1-simplex and the data-smoothing problem

Since we are interested in describing the evolution of two flock strategies as in eqs. (5.18) and (5.19) for ensemble fibration or eqs. (5.20) and (5.21) for shape fibration, we capture the trace of flocking events via a generative model on the 1-simplex. We consider an evolutionary game model, namely replicator dynamics equipped with a multiplicative control, in order to describe their evolution in the interior $(0, 1)$ of the one-dimensional simplex. The choice of replicator dynamics is influenced by its universality in describing simplex-preserving dynamics, and by virtue of being an extremal for a variational problem [Svirezhev, 1972; Raju and Krishnaprasad, 2018]. Presently, with the inclusion of a control variable, we consider a different variational problem that aims to perform data smoothing using regularization as in [Dey and Krishnaprasad, 2014]. To see this, let $\underline{x} = [x_1 \ x_2]^\mathsf{T} \in \Delta^1$ where x_i, $i = 1, 2$ denote the prevalence of strategies i (to be specified) on the simplex with the natural constraint $x_1 + x_2 = 1$. $x_i = 1, i = 1, 2$ correspond to allocation of E_{rel} entirely to one of the two pure strategies. Suppose that the frequencies associated with the strategies are updated according to the rule

$$x_i(t+1) = x_i(t)\frac{f^i(\underline{x})}{\bar{f}(\underline{x})} \tag{5.22}$$

where the fitness $f^i(x) = A\underline{x}$ and $\bar{f} = x_1 f^1(\underline{x}) + x_2 f^2(\underline{x})$. Here, $A = [a_{ij}] \in \mathbb{R}^2$ defines a payoff matrix with a_{ij} denoting the payoff of the i^{th} strategy against j^{th} strategy. In the case that the payoffs do not depend on the strategy j of against which it is matched up, the columns of A are identical. In the ode limit of (5.22), after an inhomogeneous time-scale change, we get the mean field equations:

$$\dot{x}_i(t) = x_i(t)(f^i(\underline{x}) - \bar{f}(\underline{x})), i = 1, 2 \tag{5.23}$$

It can be readily verified that (5.23) is simplex-preserving, leaving the pure strategies invariant. Since addition of the same term to each component of the fitness keeps the dynamics (5.23) unchanged, by subtracting a_{21} and a_{12} from the first and second column elements of A respectively, we get the equivalent payoff matrix

$$\tilde{A} = \begin{bmatrix} a_{11} - a_{21} & 0 \\ 0 & a_{22} - a_{12} \end{bmatrix} \tag{5.24}$$

We introduce a control input $\tilde{u}$ that scales the fitness, and choose the parameters of the matrix such that $a_{11} - a_{21} = -(a_{22} - a_{12}) = 1$ so that the fitness can be rewritten as:

$$f(\underline{x}) = \tilde{u} \begin{bmatrix} 1 & 0 \\ 0 & -1 \end{bmatrix} \underline{x} \tag{5.25}$$

Due to the simplex constraint, (5.23) is completely described using $x = x_1$:

$$\dot{x}(t) = \tilde{u}(t)x(t)(1 - x(t))(f^1(x) - f^2(x)) \tag{5.26}$$

with $x = 0, 1$ corresponding to the pure strategies 2 and 1 respectively. Due to our choice of the payoff matrix parameters, $f^1 - f^2$ is a constant. This allows

us to adopt a time-scale change by the factor $f^1 - f^2$ to arrive at our generative model:

$$\dot{x}(t) = u(t)x(t)(1 - x(t)) \tag{5.27}$$

This dynamics results in asymptotic convergence to the pure strategy $x = 1$ in the absence of control, that is, when $u(t) \equiv 1$. However, the time-varying control variable u serves to model changing preferences for the flock strategies by appropriate changes in its sign and magnitude. Such a temporal modulation of the fitness ensures feasibility of capturing arbitrary traces in the interior of the simplex.

Given a set of data points $\{x_0^d, x_1^d, ..., x_N^d\}$ with each $x_k^d \in (0, 1), k = 0, 1, ..., N$, at time instants $\{t_0, t_1, ..., t_N\}$, we formulate the optimal control problem,

$$\begin{aligned} &\min_{x(t_0),\ u\in\mathbb{R}} J(x(t_0), u) = \frac{\lambda}{2}\int_{t_0}^{t_N} u^2 dt + \sum_{i=0}^{N} F_i(x(t_i)), \\ &\text{subject to: } \dot{x} = ux(1 - x), \end{aligned} \tag{5.28}$$

where the fit errors F_i's are given by the Kullback-Leibler divergence measure of mismatch between the data and the state,

$$F_i(x) = x_i^d \log\left(\frac{x_i^d}{x}\right) + (1 - x_i^d)\log\left(\frac{1 - x_i^d}{1 - x}\right), \quad i = 0, 1, ..., N. \tag{5.29}$$

We can directly appeal to Pontryagin's Maximum Principle (PMP) and theorem (5.3.1) to write necessary conditions for optimality. We can write the pre-Hamiltonian as,

$$H(x, p, u) = upx(1 - x) - \frac{\lambda}{2}u^2. \tag{5.30}$$

The Hamiltonian maximization condition (5.6) yields an optimal control in each time interval $t \in (t_i, t_{t+1}),\ i = 0, 1, ..., N-1$,

$$u = \frac{1}{\lambda} px(1-x), \tag{5.31}$$

with Hamiltonian given by,

$$\mathcal{H}(x, p) = \frac{1}{2\lambda} p^2 x^2 (1-x)^2. \tag{5.32}$$

Hamilton's equations (5.5) read,

$$\begin{aligned} \dot{x} &= \frac{1}{\lambda} p x^2 (1-x)^2 \\ \dot{p} &= -\frac{1}{\lambda} p^2 x (1-x)(1-2x). \end{aligned} \tag{5.33}$$

The jump conditions for p (5.7) can be written as,

$$\begin{aligned} & p(t_0^-) = 0, \\ & p(t_i^+) - p(t_i^-) = \frac{x(t_i) - x_i^d}{x(t_i)(1 - x(t_i))}, \quad i = 0, 1, ..., N, \\ & p(t_N^+) = 0. \end{aligned} \tag{5.34}$$

Remark 5.1. Note that the optimal control is piecewise constant since $\frac{du}{dt} = 0$ for each of these time intervals $t \in (t_i, t_{i+1}),\ i = 0, 1, ..., N-1$.

Therefore, denoting $x_k = x(t_k),\ k = 0, 1, ..., N$, any optimal control can be described by a vector $(u_0, u_1, ..., u_N)$ with the conditions

$$\begin{aligned} & u_0 = \frac{1}{\lambda}(x_0 - x_0^d), \\ & u_k - u_{k-1} = \frac{1}{\lambda}(x_k - x_k^d), \quad k = 1, 2, ..., N \\ & u_N = 0. \end{aligned} \tag{5.35}$$

Piecewise constancy of the control input allows us to write the solution to the state equation (5.26) explicitly. Suppose the sampling time of the trace is uniform, i.e. $\Delta t := t_{k+1} - t_k, \forall k \in \{0, ..., N-1\}$, integrating the state equation (5.26) in (t_k, t_{k+1}), we can write

$$x_{k+1} = \frac{x_k e^{u_k \Delta t}}{1 + x_k \left(e^{u_k \Delta t} - 1\right)}, \quad k = 0, 1, ..., N-1. \tag{5.36}$$

By iteration, we can in turn write every x_k as a function of x_0 and $u_0, u_1, ..., u_{k-1}$,

$$x_k = x_k(x_0) = \frac{x_0 e^{(u_0 + u_1 + \cdots + u_{k-1})\Delta t}}{1 + x_0 \left(e^{(u_0 + u_1 + \cdots + u_{k-1})\Delta t} - 1\right)}, \quad k = 1, 2, ..., N. \tag{5.37}$$

The endpoint condition ($u_N = 0$) can then be written as,

$$x_0 + x_1 + \cdots + x_N = x_0^d + x_1^d + \cdots + x_N^d, \tag{5.38}$$

where the left hand side of (5.38) is a function of x_0. Solving the optimal control problem (5.28) thus boils down to solving (5.38) for $x_0 \in (0, 1)$.

Remark 5.2. The value of the regularization parameter λ is usually chosen through cross validation technique. We do not employ any such techniques here. The value of λ is chosen such that the root finding algorithm for solving (5.38) converges for all events. For $\lambda = 0.2$, the roots were found with reasonably good accuracy with value of the function at the root being of the order of 1×10^{-5} or lower for all events. For lower λ however, the problem becomes stiffer and left hand side of (5.38) demonstrates 'effective discontinuity' in x_0. This poses serious problem in solving (5.38). It is to be noted that the original captured flight data was subjected to data-smoothing to obtain smooth trajectories [Dey, 2015].

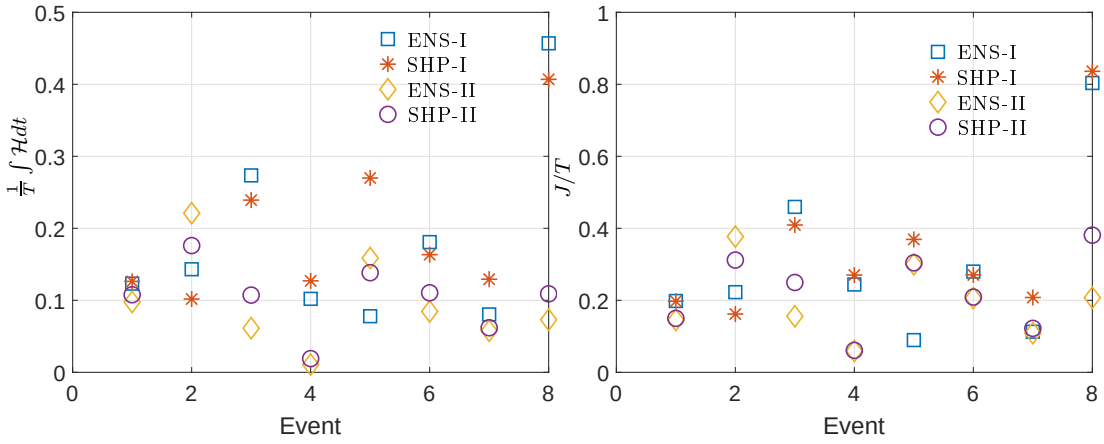

(a) Time Averaged Hamiltonian Integral

(b) Time Averaged Total Cost

Figure 5.1: Hamiltonian signatures

The data-smoothing problem in [Dey, 2015] considered a linear generative model as in Section 5.3.1 and used ordinary cross validation for trajectory of each bird to determine the appropriate weight to the regularization term. This generated smooth trajectories with suppressed level of noise compared to the original data. We then take the sampled data $\{x_0^d, \cdots, x_N^d\}$ from these smooth trajectories. This can justify taking same value of λ across all the events. As a future step, cross validation could be employed to arrive at a good value of λ in the range where (5.38) can be solved.

5.6 Data Fitting Results

For all 8 events, we solve the optimal control problem (5.28) and report the results here. The value of the regularization weight λ is taken to be 0.2 and 100 data samples at regular time intervals are taken for all events. Given the data

vector, we solve equation (5.38) for $x_0 \in (0,1)$. In Table 5.2, we report time averaged Hamiltonian integrals and time averaged total costs for all the different games that we consider in eqs. (5.18) to (5.21). These time averaged Hamiltonian integrals are thought of as *cognitive costs* of the events. As seen from Table 5.2, the trend of (ENS-I) closely follow the game (SHP-I), while the other two games seem to follow each other. This is graphically represented in Fig. 5.1. Optimal control solutions for the games ENS-I (5.18) and SHP-II (5.21) for individual events are shown in Fig. 5.2–5.9. We note that more variation in the energy time signal results in higher cognitive cost (in both measures). This is interpreted as the collecting having to 'think' more to properly allocate the modes, incurring higher costs. These cognitive costs for a particular game can thus indicate overall physical behavior of the flock. For example, in the games (ENS-II) or (SHP-II) where a rotational energy is considered as one of the pure strategies, relatively higher cognitive costs for event 2, 5 indicate that the flocks went through more rotations than the other events during the flight periods. On the other hand, low cost for event 4 is justified by almost rectilinear overall motion. Similar conclusions can be drawn for the other set of games (ENS-I) and (SHP-II), where the respective cognitive cost will stipulate nature of variation of the democratic (reshuffling within the flock) energy. The higher the cost is, more aggressively the relative positions of the birds within the flocks are changed, leading to a more complex flight event.

Duration	$\frac{\int \mathcal{H} dt}{\int dt}$				$\frac{J(x_0,u)}{\int dt}$			
(seconds)	(ENS-I)	(SHP-I)	(ENS-II)	(SHP-II)	(ENS-I)	(SHP-I)	(ENS-II)	(SHP-II)
5.4875	0.1232	0.1263	0.0976	0.1077	0.1981	0.1975	0.1454	0.1499
1.8176	0.1432	0.1018	0.2210	0.1760	0.2227	0.1619	0.3769	0.3118
5.6118	0.2735	0.2392	0.0613	0.1073	0.4595	0.4092	0.1557	0.2495
2.3471	0.1021	0.1270	0.0107	0.0190	0.2440	0.2702	0.0594	0.0610
3.8824	0.0779	0.2699	0.1587	0.1383	0.0896	0.3692	0.3001	0.3041
4.1588	0.1809	0.1634	0.0846	0.1105	0.2799	0.2706	0.2063	0.2090
5.7353	0.0804	0.1293	0.0576	0.0619	0.1127	0.2079	0.1087	0.1221
1.7588	0.4569	0.4069	0.0731	0.1090	0.8037	0.8361	0.2074	0.3810

Table 5.2: Hamiltonian Signature

5.7 Discussion

In this chapter, we have brought together several results from geometry, optimal data-fitting and evolutionary game theory to associate a cognitive aspect to flocking. The flight data of Starling flocks give rise to time-signals of energy mode distributions. Here, the whole flock is conceptualized to making decisions about how to optimally allocate its energy in several modes. The different energy modes are thought as pure strategies of an evolutionary game and their fitness is modulated by some decision or control variables. These controls are then determined by optimally fitting this model to the observed energy mode distributions in the data. The cost to this data-fitting are referred to as cognitive cost for the flock. In this work, we have only considered splitting energy into two modes. In this

setting, the optimal control solutions present interesting characteristics. It will be an important direction to consider energy splitting in several energy modes, hence solving the fitting problem in a higher dimensional simplex. It will also be of interest to interpret the cognitive costs in such scenarios.

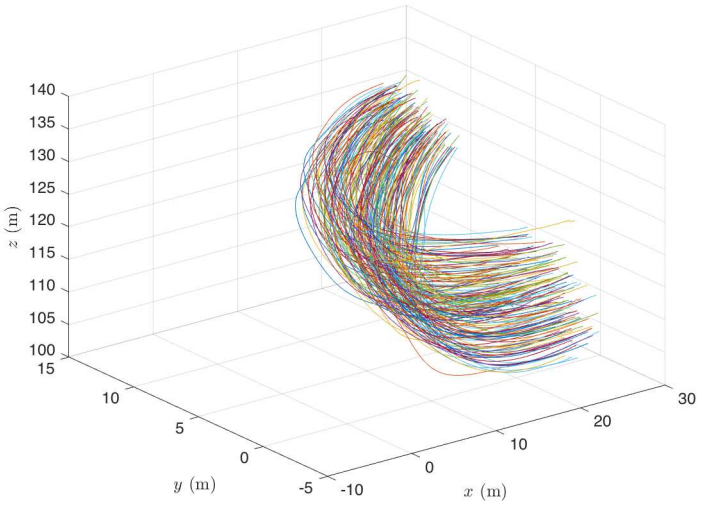

(a) Flock Trajectory

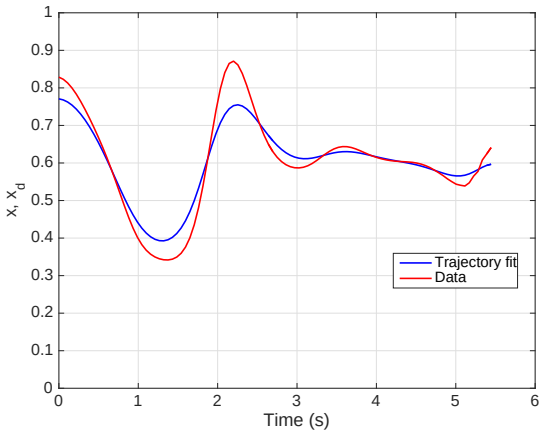

(b) Trajectory Fit

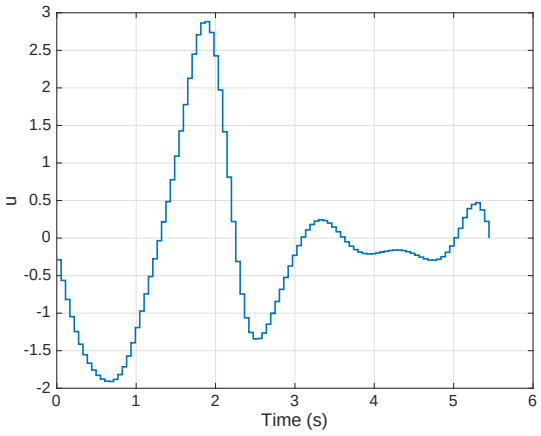

(c) Optimal Control

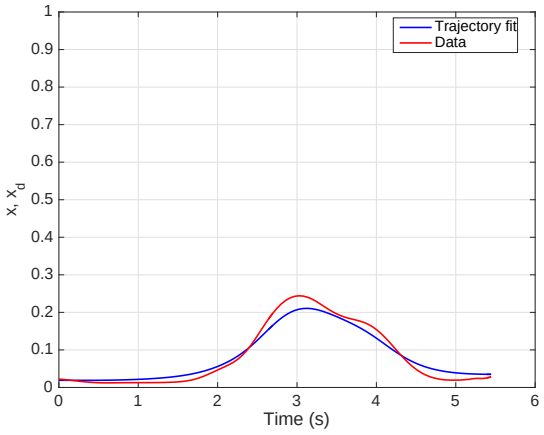

(d) Trajectory Fit

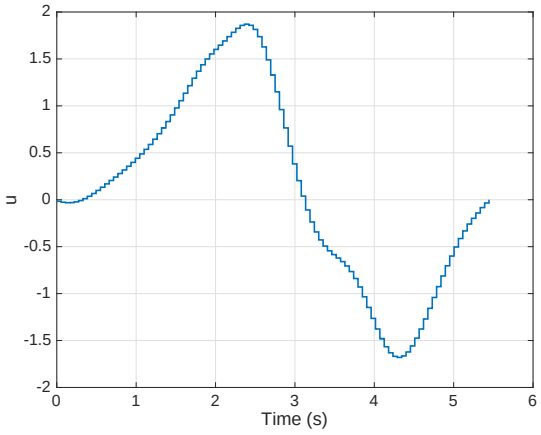

(e) Optimal Control

Figure 5.2: Event 1, $\lambda = 0.2$, Number of samples $= 100$, (b)-(c) $x = \frac{E_{\text{dem}}}{E_{\text{rel}}}$ (ENS-I), (d)-(e) $x = \frac{E_{\text{rot}}}{E_{\text{rel}}}$ (SHP-II)

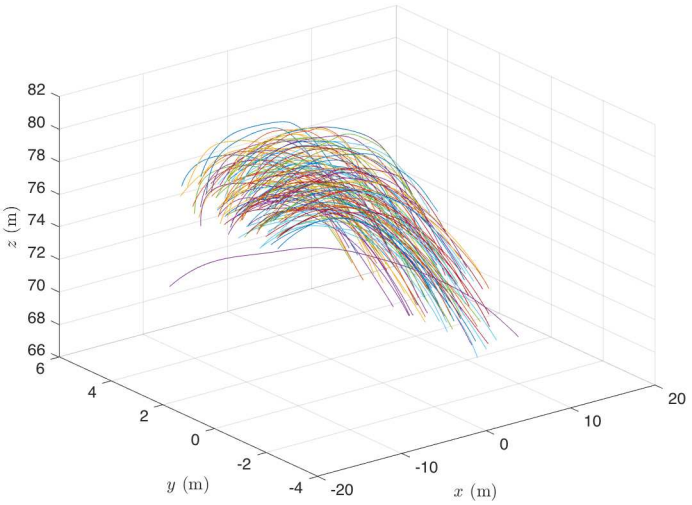

(a) Flock Trajectory

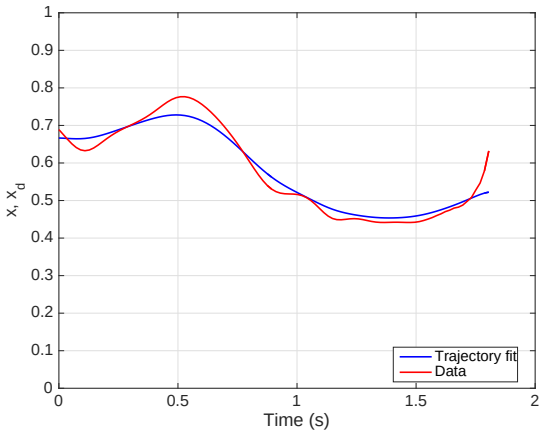

(b) Trajectory Fit

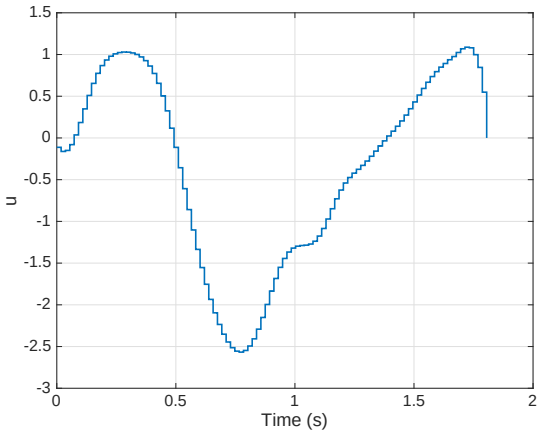

(c) Optimal Control

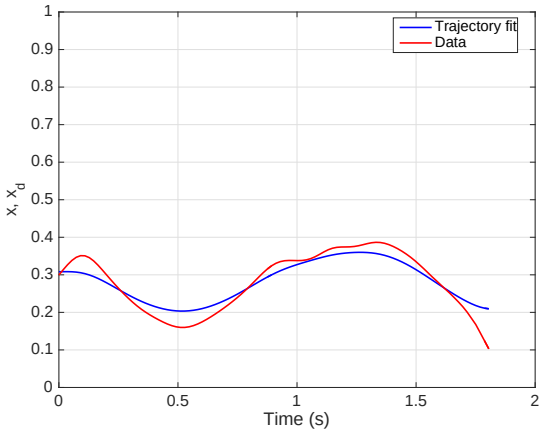

(d) Trajectory Fit

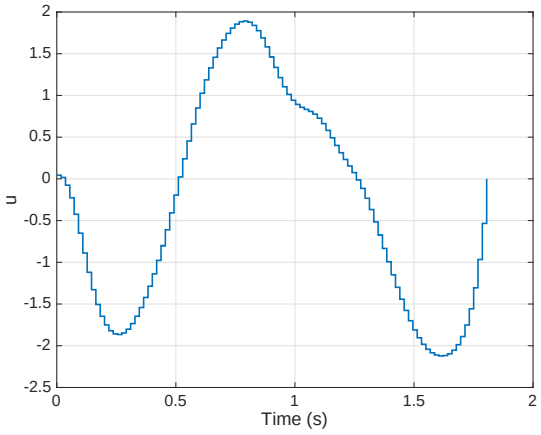

(e) Optimal Control

Figure 5.3: Event 2, $\lambda = 0.2$, Number of samples $= 100$, (b)-(c) $x = \frac{E_{\text{dem}}}{E_{\text{rel}}}$ (ENS-I), (d)-(e) $x = \frac{E_{\text{rot}}}{E_{\text{rel}}}$ (SHP-II)

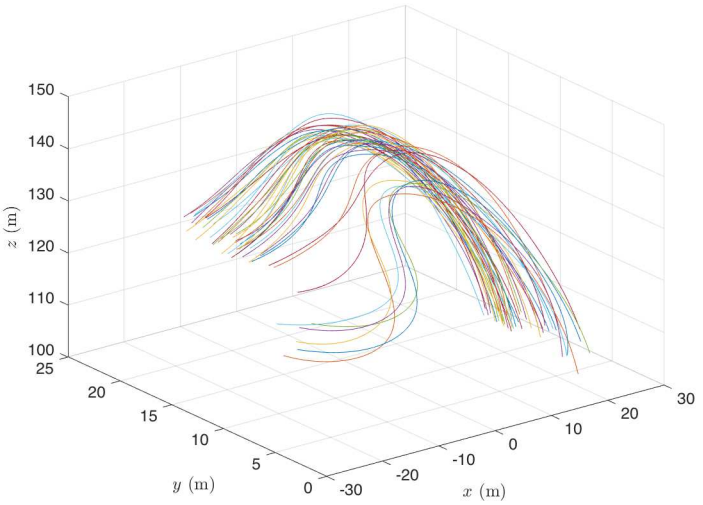

(a) Flock Trajectory

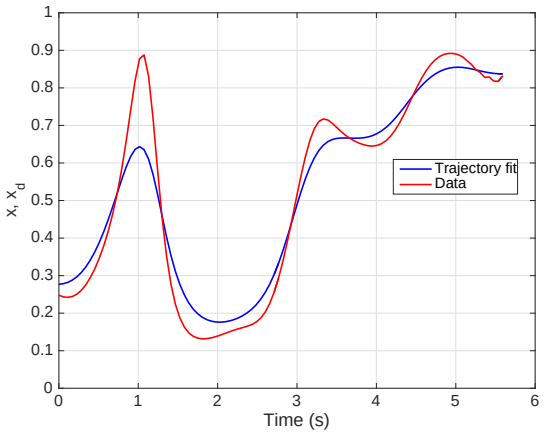

(b) Trajectory Fit

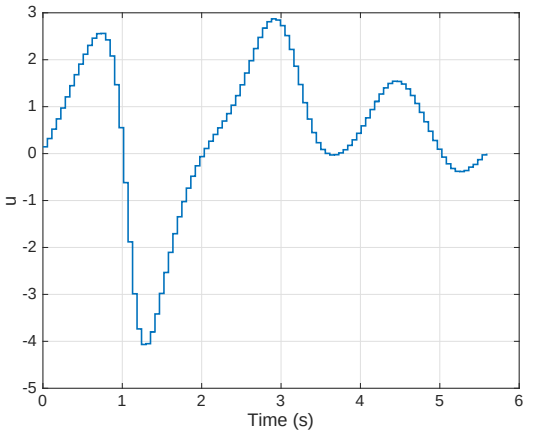

(c) Optimal Control

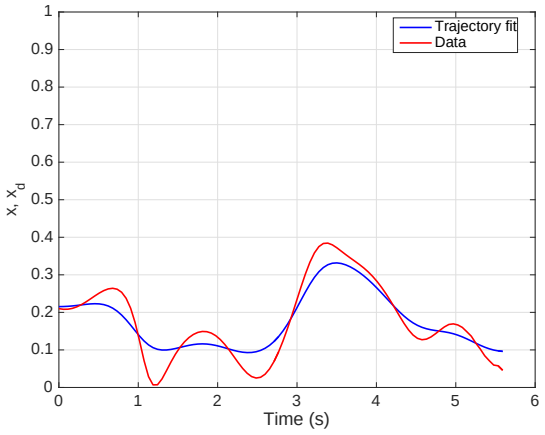

(d) Trajectory Fit

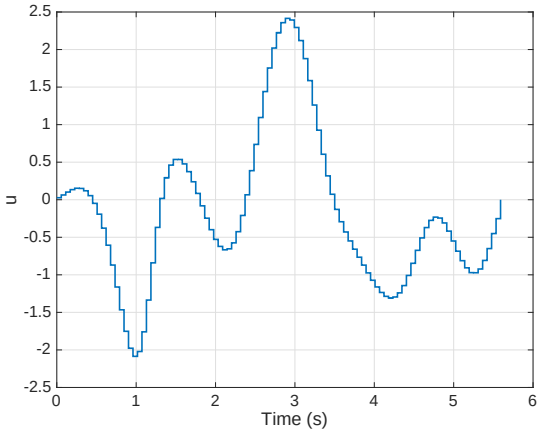

(e) Optimal Control

Figure 5.4: Event 3, $\lambda = 0.2$, Number of samples $= 100$, (b)-(c) $x = \frac{E_{\text{dem}}}{E_{\text{rel}}}$ (ENS-I), (d)-(e) $x = \frac{E_{\text{rot}}}{E_{\text{rel}}}$ (SHP-II)

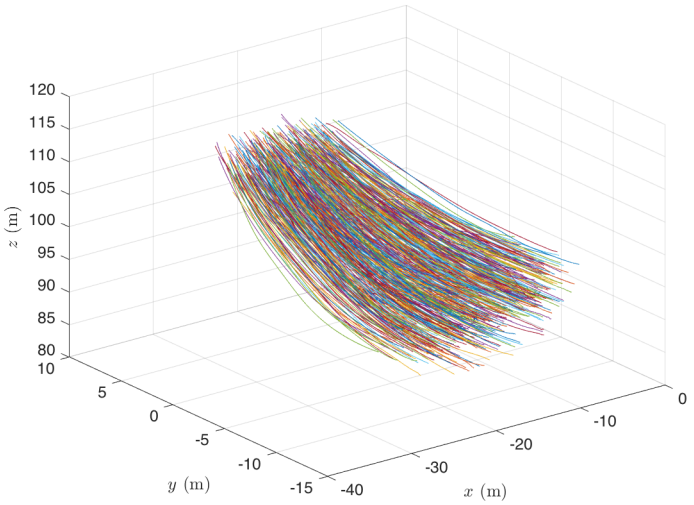

(a) Flock Trajectory

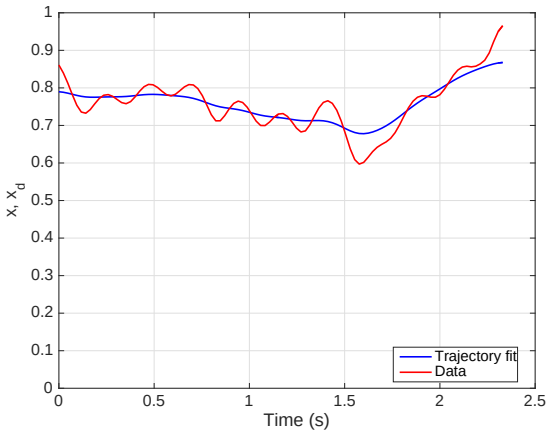

(b) Trajectory Fit

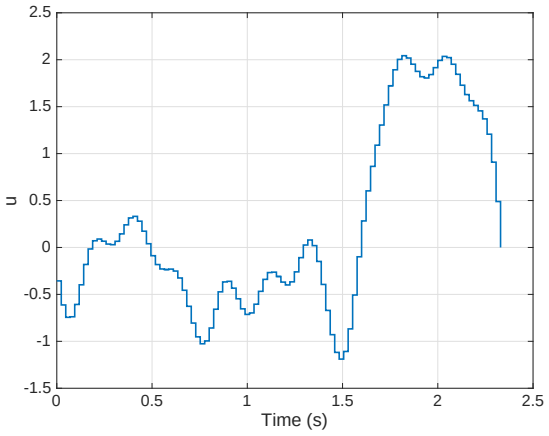

(c) Optimal Control

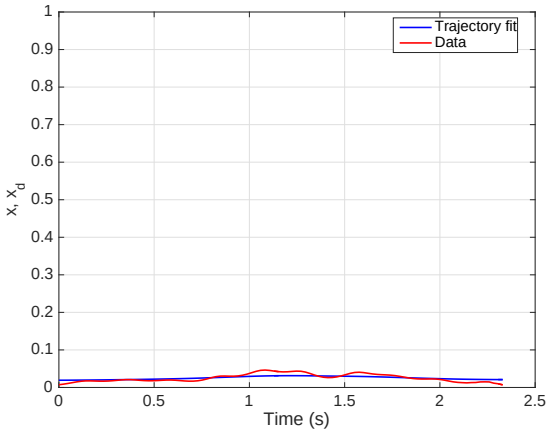

(d) Trajectory Fit

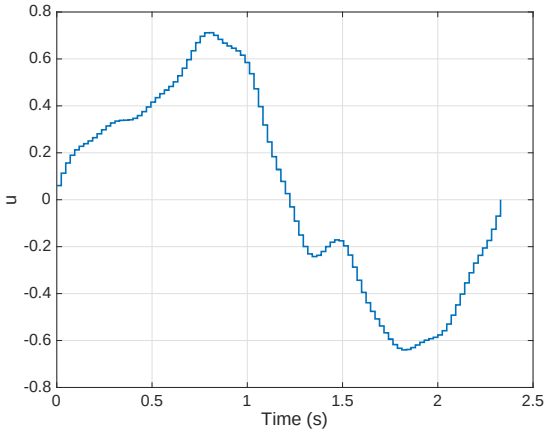

(e) Optimal Control

Figure 5.5: Event 4, $\lambda = 0.2$, Number of samples $= 100$, (b)-(c) $x = \frac{E_{\text{dem}}}{E_{\text{rel}}}$ (ENS-I), (d)-(e) $x = \frac{E_{\text{rot}}}{E_{\text{rel}}}$ (SHP-II)

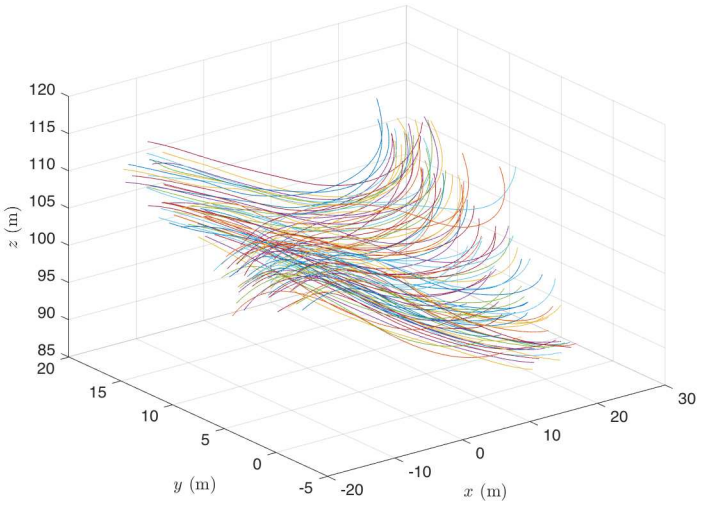

(a) Flock Trajectory

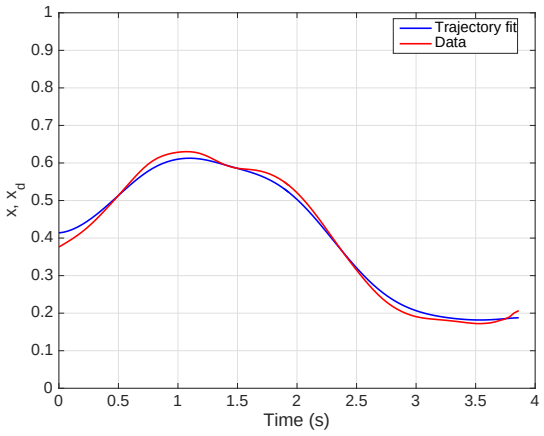

(b) Trajectory Fit

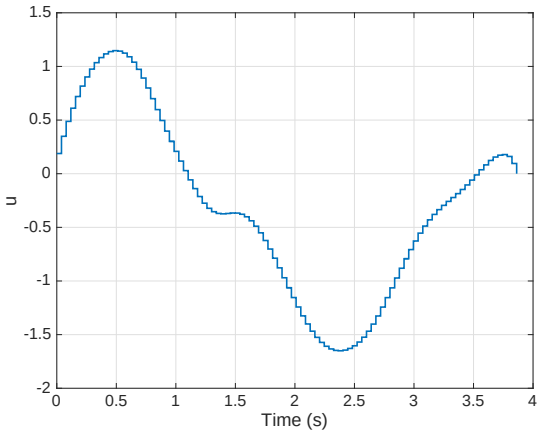

(c) Optimal Control

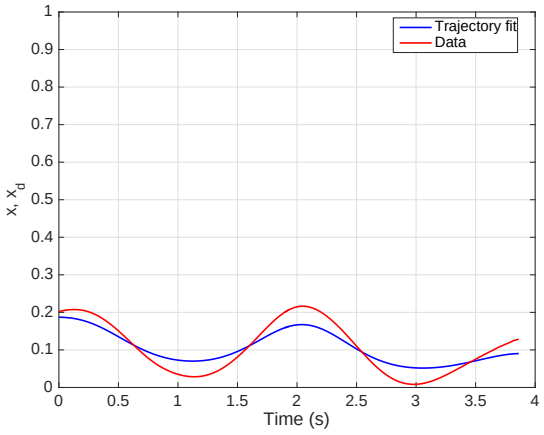

(d) Trajectory Fit

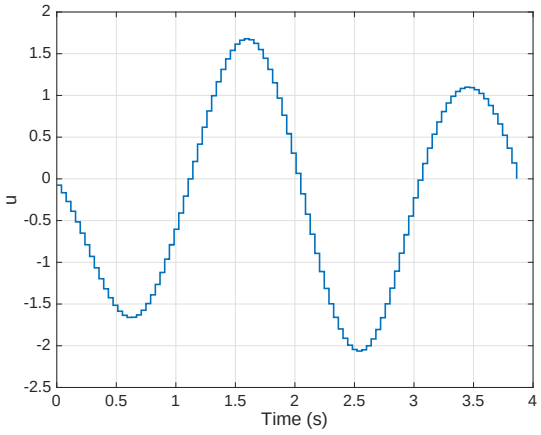

(e) Optimal Control

Figure 5.6: Event 5, $\lambda = 0.2$, Number of samples $= 100$, (b)-(c) $x = \frac{E_{\text{dem}}}{E_{\text{rel}}}$ (ENS-I), (d)-(e) $x = \frac{E_{\text{rot}}}{E_{\text{rel}}}$ (SHP-II)

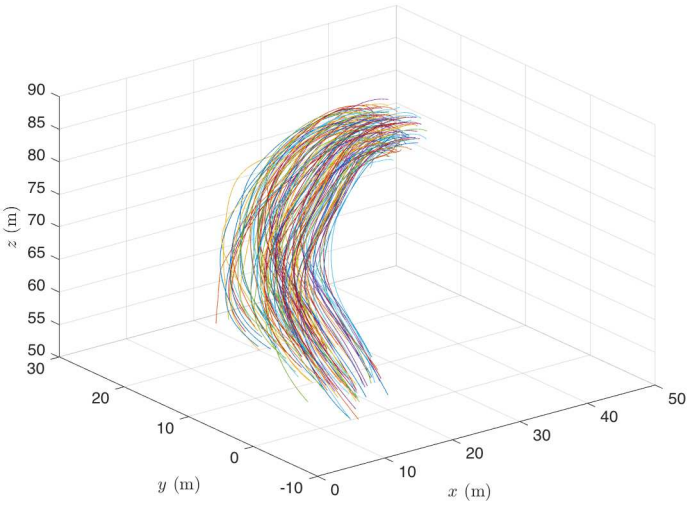

(a) Flock Trajectory

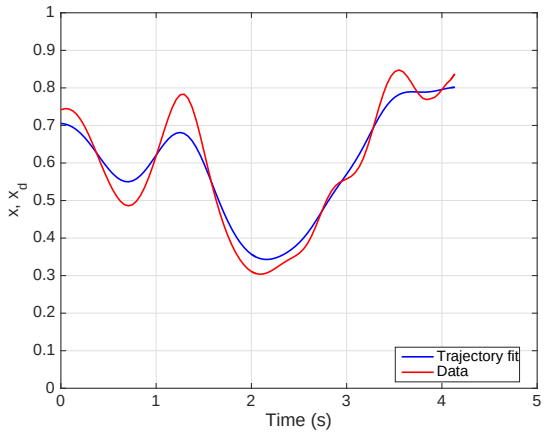

(b) Trajectory Fit

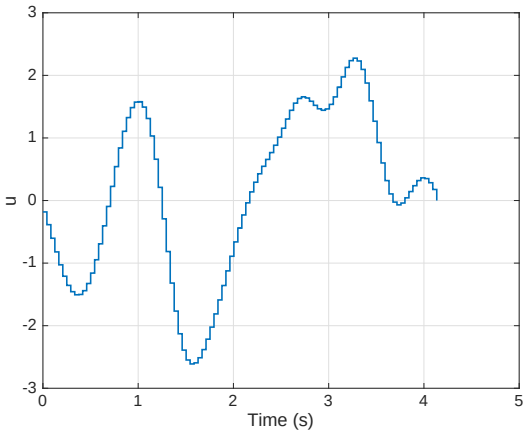

(c) Optimal Control

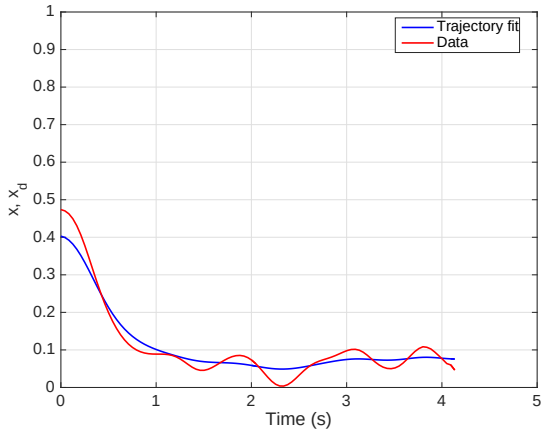

(d) Trajectory Fit

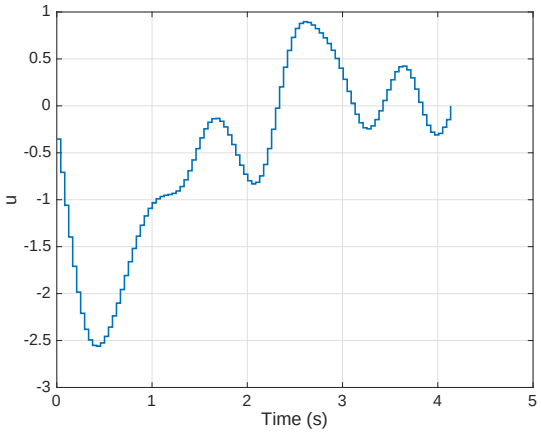

(e) Optimal Control

Figure 5.7: Event 6, $\lambda = 0.2$, Number of samples $= 100$, (b)-(c) $x = \frac{E_{\text{dem}}}{E_{\text{rel}}}$ (ENS-I), (d)-(e) $x = \frac{E_{\text{rot}}}{E_{\text{rel}}}$ (SHP-II)

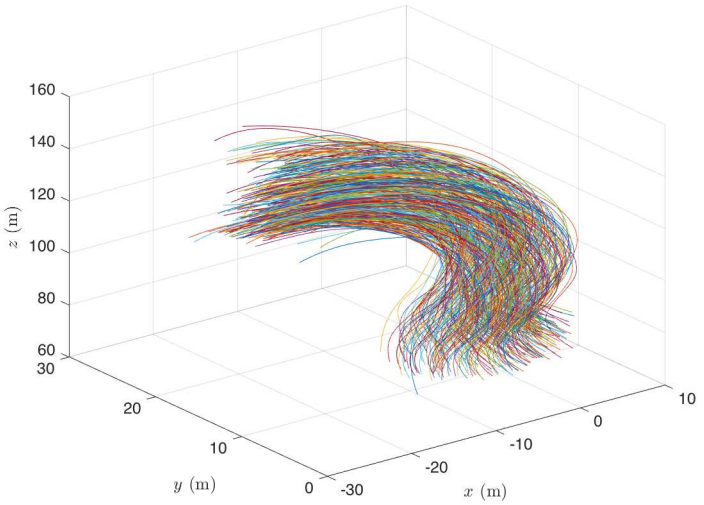

(a) Flock Trajectory

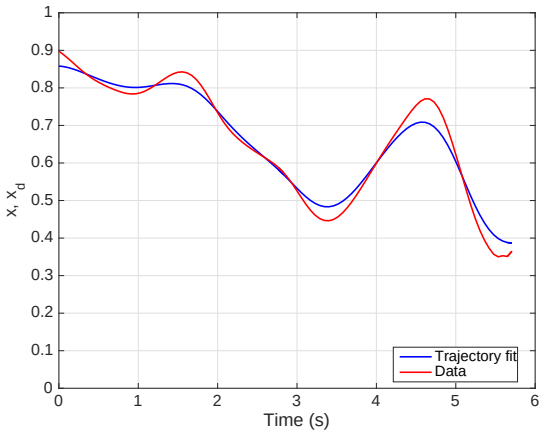

(b) Trajectory Fit

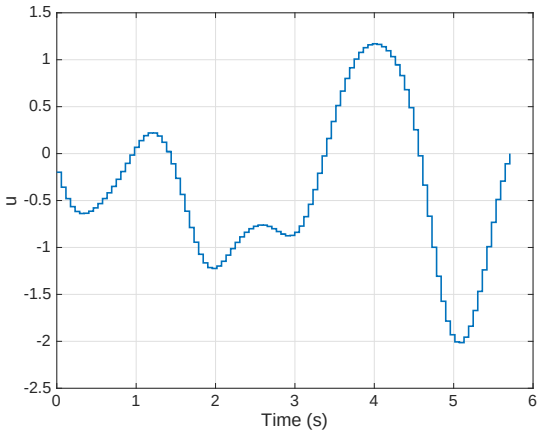

(c) Optimal Control

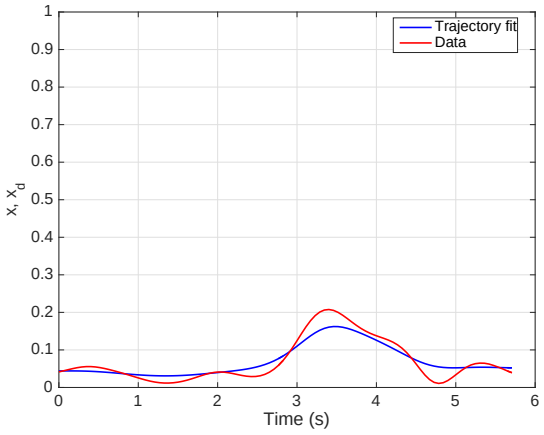

(d) Trajectory Fit

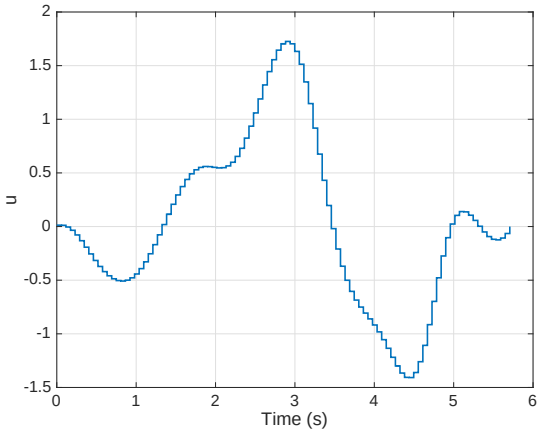

(e) Optimal Control

Figure 5.8: Event 7, $\lambda = 0.2$, Number of samples $= 100$, (b)-(c) $x = \frac{E_{\text{dem}}}{E_{\text{rel}}}$ (ENS-I), (d)-(e) $x = \frac{E_{\text{rot}}}{E_{\text{rel}}}$ (SHP-II)

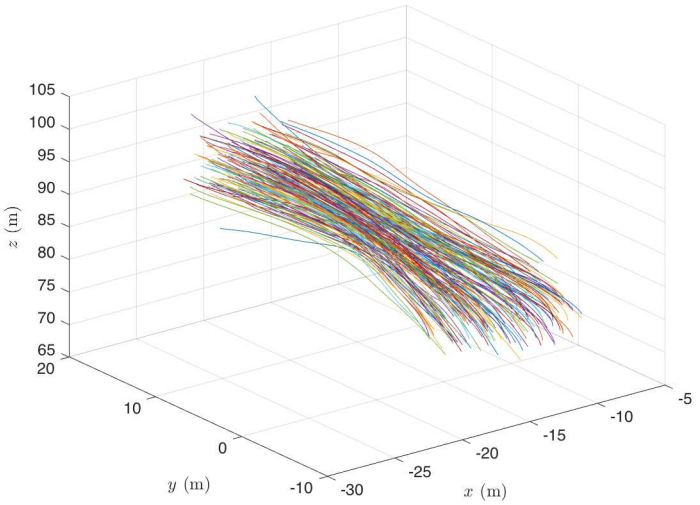

(a) Flock Trajectory

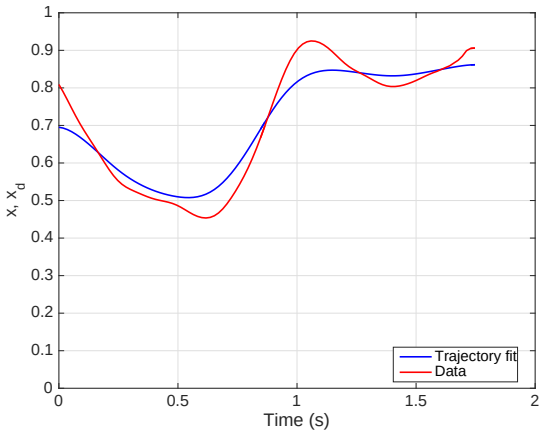

(b) Trajectory Fit

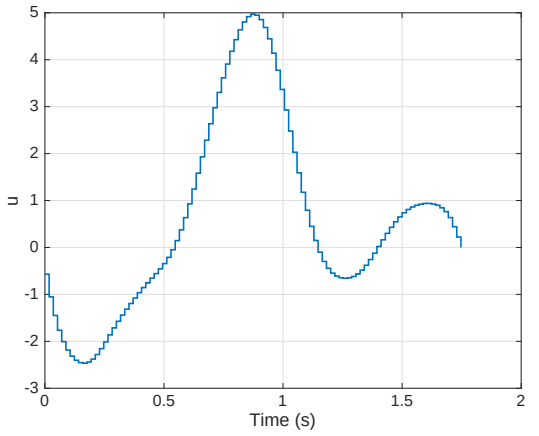

(c) Optimal Control

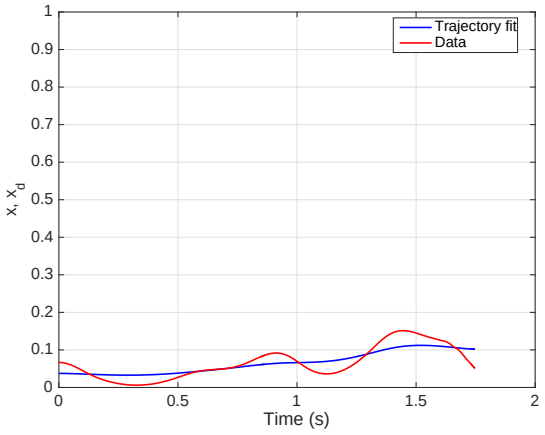

(d) Trajectory Fit

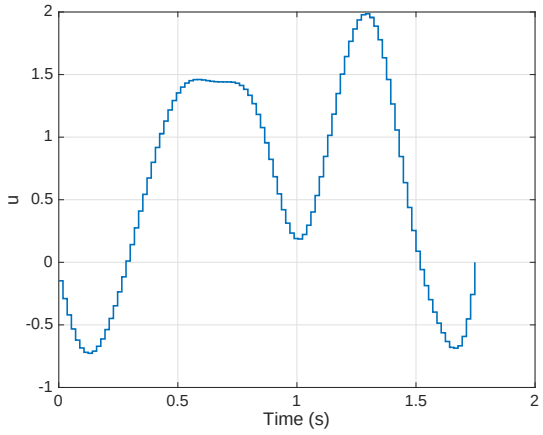

(e) Optimal Control

Figure 5.9: Event 8, $\lambda = 0.2$, Number of samples $= 100$, (b)-(c) $x = \frac{E_{\text{dem}}}{E_{\text{rel}}}$ (ENS-I), (d)-(e) $x = \frac{E_{\text{rot}}}{E_{\text{rel}}}$ (SHP-II)

Chapter 6

Conclusions and Directions for Future Research

We have made an attempt to explain collective behavior in natural flocks in this thesis. Possible robotic applications in this context are also presented. The thesis is distinctively divided into two parts depending on the underlying approach – either collective behavior is viewed as an emergence of interactions between small number of agents in a 'bottom-up' fashion or those interactions are inferred in a 'top-down' way. We summarize below the contributions of this dissertation along with directions in which this line of research can be continued.

In Chapter 2, we explored inter-agent interaction strategies from both theoretical and implementation perspectives. First, we consider a two-agent scenario in which one agent pursues the other using constant-bearing (CB) pursuit law. The pursued agent behaves like a moving beacon whose movement is independent to the other. It is then shown that under particular parameter setting of the CB law

and constant curvature paths of the beacon, the combined equations of motion of the system resemble to that of a couple of gravitating particles. Periodic orbits are shown to exist, each corresponding to a fixed energy. This result is used in a robotic application subsequently. We have effectively utilized the results of this problem in the problem of encircling a static beacon that is sensed visually by a mobile robot by means of a camera with limited field-of-view (FOV). Proper feedback law for the robot is advised to make a desired closed loop in the phase space asymptotically stable. This guarantees intermittent appearance of the beacon in the camera's FOV. Laboratory demonstration of this problem incorporates online estimation of the beacon's position when it falls out of the FOV. Secondly, laboratory implementations of two biologically plausible feedback laws are presented. These laws include another dual-agent law called Mutual Motion Camouflage and a multi-agent consensus type law called Topological Velocity Alignment. In this chapter we have shown how complex collective motion patterns can emerge from simple interactions among the agents in a flock.

We study the problem of optimal steering of a single agent in Chapter 3. The agent is driven from initial to final configuration on the plane while minimizing the control cost that penalizes both speed and curvature control. Optimal control solution is obtained by using Pontryagin's Maximum Principle (PMP) and Lie-Poisson reduction technique. Optimal trajectories are categorized by the values of the Hamiltonian and another conserved quantity called Casimir. This problem is then extended to capture the scenario of a flock of agents moving on the plane.

These agents interact with each other by a predefined graph. The individual control costs are coupled with mismatch in control with the neighbors. This chapter forms a bridge between the two parts of the thesis.

In Chapter 4, we take the problem of optimal steering of many agent case and consider its continuum limit. A goal of such an approach is to develop wave equations that may explain observed phenomenon of information transfer in natural flocks. We only consider the cyclic graph of interaction that enables us to present the results in a compact way. A general optimal control problem in the loop group case is stated. General controllability result in infinite dimensional setting is shown to be helpful to construct such optimal control problem. The necessary conditions for optimality, namely the Pontryagin's Maximum Principle (PMP) in Hilbert space setting is only valid under a condition of finite co-dimensionality of a reachable set. Two special cases of this problem are studied. The case in which the underlying group is the Heisenberg group H(3), i.e. a continuum of nonholonomic integrators is studied in detail. We have shown that the optimal control solutions possess traveling wave character. Moreover, a synchronization result is obtained in which the infinite coupling strength prohibits every agent in the flock to behave differently. The case of planar continuum, i.e. agents moving in the special Euclidean group SE(2) is also considered. Optimal control evolution equations are obtained by both calculus of variations and PMP approach. Similar to the H(3) case, synchronization result is obtained. Numerical simulations for both these cases are presented. However, we have not been able to perform a thorough

analytical study of the partial differential equations obtained in the SE(2) case. It is one of the directions in which future research could be conducted. A critical question will answer whether traveling wave solutions exist in this case. Furthermore, different interaction graphs can be considered to uncover more interesting details about this problem.

Chapter 5 presents a data-driven analysis of flight data of European Starling flocks, captured in Rome. This data gives rise to temporal signals of the flock's energy distribution in several energy modes. We use an optimal control based data-fitting technique to explain this data as the outcome of an evolutionary game on a simplex. We call the data-fitting cost functionals of the underlying optimal control problem as 'cognitive cost' that measures the cognitive effort of the flock to allocate its energy in different modes. In our work, we have only considered energy splitting into two modes so as to consider a simple game on the one-dimensional simplex. This can be extended to higher dimensions where multiple energy modes are considered.

Appendix A

An Optimal Control Problem in an Infinite Dimensional Setting

A.1 Introduction

After Pontryagin provided his method for solving optimal control problems in finite dimensional setting [Pontryagin et al., 1962], there have been many attempts to try and prove similar principles in infinite dimensions. However, the counterexample of Egorov [Egorov, 1963] posed a serious challenge to that process. This counterexample showed that the Pontryagin's maximum principle does not generally hold in infinite dimensions. In particular, the costate variable can become identically zero, making the maximum principle empty. The advancements in the following decades [Ekeland, 1979; Fattorini, 1987; Li and Yong, 2012; Krastanov et al., 2011] showed that it is possible to state PMP in some cases where some additional assumptions are made. In this work, we adopt a similar path to prove

the maximum principle set in a much friendlier setting.

We consider an abstract differential equation in a Hilbert space,

$$\frac{dx(t)}{dt} = f(t, x(t), u(t)), \quad \text{a.e. in } [0, T], \tag{A.1}$$

where $x(t) \in X$, $u(\cdot) \in \mathcal{U}$, and $T > 0$. Let X be a Hilbert space called the state space and $\mathcal{U}$ be the set of all measurable functions $u(\cdot) : [0, T] \to U$, where U is a separable metric space called the control space. With this setup, we formulate the following optimal control problem (P),

$$\text{(P)} \qquad \begin{aligned} &\min_{u \in \mathcal{U}} J(u) = \int_0^T L(t, x(t), u(t))dt \\ &\text{subject to:} \quad \dot{x} = f(t, x, u), \text{a.e. in } [0, T], \quad x(0) = x_0, x(T) = x_T. \end{aligned} \tag{A.2}$$

We assume that both the functions $f(\cdot, \cdot, \cdot)$ and $L(\cdot, \cdot, \cdot)$ are Bochner integrable in $t \in [0, T]$ and Lipschitz continuous in $x(t) \in X$, with constant K. Furthermore, we require the existence of the continuous Fréchet derivatives $f'_x(t, x, u)$ and $L'_x(t, x, u)$. We also assume the functions f, L and their derivatives f'_x, L'_x to be bounded, i.e. there exists an $M > 0$, such that

$$\begin{aligned} &\|f(t, x, u)\| \leq M, \;\; \|f'_x(t, x, u)\| \leq M, \\ &\|L(t, x, u)\| \leq M, \;\; \|L'_x(t, x, u)\| \leq M, \end{aligned} \tag{A.3}$$

for all $(t, x(t), u(t)) \in [0, T] \times X \times U$. Note that these hypotheses ensure a continuous and unique solution of (A.1) to exist [Avez, 1986]. Let the space $\mathcal{U}$ be endowed with the distance function,

$$d(u, v) = \text{meas}\{t \;:\; u(t) \neq v(t)\}, \tag{A.4}$$

where meas$\{\cdot\}$ denotes the usual Lebesgue measure in $[0, T]$. Then, according to Theorem 5.3 of [Fattorini, 1987], the space $\mathcal{U}$ is complete with respect to the distance d. A direct consequence of the assumptions stated above leads to an important result [Krastanov et al., 2011].

Lemma A.1.1. *Let $u_1(\cdot), u_2(\cdot)$ be any two arbitrary members of $\mathcal{U}$. Denote the state trajectories associated with these controls by, $x_i(\cdot) = x(\cdot, u_i(\cdot)), i = 1, 2$. Then there exist positive constants C_1, C_2 such that,*

$$\sup_{t\in[0,T]} \|x_1(t) - x_2(t)\| \leq C_1 d(u_1, u_2), \tag{A.5}$$

$$|J(u_1) - J(u_2)| \leq C_2 d(u_1, u_2). \tag{A.6}$$

Proof. Let $S \subset [0, T]$ be the set where the controls u_1 and u_2 differ, i.e. $d(u_1, u_2) =$ meas$\{S\}$. We know that (A.1) can also be written as,

$$x(t) = x_0 + \int_0^t f(s, x(s), u(s))ds.$$

Then,

$$\begin{aligned}
x_1(t) - x_2(t) &= \int_0^t \left(f(s, x_1(s), u_1(s)) - f(s, x_1(s), u_1(s))\right) ds \\
&= \int_0^t \left(f(s, x_1(s), u_1(s)) - f(s, x_2(s), u_1(s))\right) ds \\
&\quad + \int_0^t \left(f(s, x_2(s), u_1(s)) - f(s, x_2(s), u_2(s))\right) ds \\
&= \int_0^t \left(f(s, x_1(s), u_1(s)) - f(s, x_2(s), u_1(s))\right) ds \\
&\quad + \int_{[0,t]\cap S} \left(f(s, x_2(s), u_1(s)) - f(s, x_2(s), u_2(s))\right) ds.
\end{aligned}$$

Taking norm of both sides we get,

$$\|x_1(t) - x_2(t)\| \leq K \int_0^t \|x_1(s) - x_2(s)\| \, ds + 2Md(u_1, u_2),$$

where the Lipschitz property of f in x is used in the first term and the uniform boundedness is used in the second term. By the use of Gronwall-Bellman inequality, we arrive at (A.5). The result (A.6) can be derived analogously. ■

We now proceed to solve this problem by a maximum principle based approach. Before we state the maximum principle, let us give some additional technical details that are going to be essential for the proof of the maximum principle.

Definition A.1. (**Finite Codimensionality**) [Fattorini, 1987] A subset S of a Hilbert space Z is called to be *finite codimensional* in Z, if there exists a closed subspace $Z_c \subseteq Z$ of finite codimension such that $S_c = \Pi(\overline{\text{co}}(S))$, has nonempty interior in Z_c, where Π_c denotes the orthogonal projection from Z onto Z_c and $\overline{\text{co}}$ means closed convex hull.

We will now make a key assumption to derive a nontrivial maximum principle. Let a solution of problem (P) exist and that optimal control is denoted as $u^* \in \mathcal{U}$ and let the corresponding optimal trajectory be denoted as $x^*(t)$. Then define the 'reachable set' as,

$$\begin{aligned} \mathsf{R} := \Bigg\{ z(T) \in X \mid z(t) = &\int_0^t f_x'(s, x^*(s), u^*(s)) \cdot z(s) ds \\ &+ \int_0^t (f(s, x^*(s), v(s)) - f(s, x^*(s), u^*(s))) \, ds, \text{ for some } v(\cdot) \in \mathcal{U} \Bigg\} \end{aligned} \quad \text{(A.7)}$$

(A1) The set R is finite codimensional in X.

A.2 Maximum Principle

Using usual formalism, we invoke the *pre-Hamiltonian* function $H : \mathbb{R} \times X \times U \times \mathbb{R} \times X^* \to \mathbb{R}$ as,

$$H(t, x(t), u(t), p_0, p(t)) = p_0 L(t, x(t), u(t)) + \langle p(t), f(t, x(t), u(t)) \rangle , \tag{A.8}$$

where $p(t) \in X^*$ is called the costate variable. Intuitively, we want to make the following statement of the maximum principle that needs to be validated.

Theorem A.2.1. ***(Maximum Principle)*** *Let $u^* \in \mathcal{U}$ be an optimal control for problem (P) and $x^*(t)$ be the corresponding optimal trajectory. Then, there exist a pair $(p_0^*, p^*(t)) \in \mathbb{R} \times X^*, t \in [0, T]$, such that $(p_0^*, p^*) \not\equiv (0, 0)$, $p_0^* \leq 0$, $p^*(\cdot)$ satisfies the differential equation,*

$$\dot{p}^*(t) = -\left(f_x'(t, x^*(t), u^*(t))^\star \, p^*(t) - p_0^* L_x'(t, x^*(t), u^*(t)\right), \tag{A.9}$$

where by $\mathcal{A}^\star$ we denote the adjoint operator of the operator $\mathcal{A}$. The pointwise maximization of the pre-Hamiltonian holds,

$$H(t, x^*(t), u^*(t), p_0^*, p^*(t)) = \max_{v \in U} H(t, x^*(t), v, p_0^*, p^*(t)), \tag{A.10}$$

Moreover, x^* and p^* satisfy Hamilton's canonical equations, i.e.

$$\frac{dx^*}{dt} = \frac{\delta H}{\delta p^*}(t, x^*, u^*, p_0^*, p^*) \tag{A.11}$$

$$\frac{dp^*}{dt} = -\frac{\delta H}{\delta x^*}(t, x^*, u^*, p_0^*, p^*). \tag{A.12}$$

Proof. At the outset, we begin by introducing the variable, $x^0(t) \in \mathbb{R}$ that obeys the dynamics, $\dot{x}^0 = L(t, x, u)$, $x^0(0) = 0$. Define, $y(t) = \begin{pmatrix} x^0(t) \\ \\ x(t) \end{pmatrix} \in \mathbb{R} \times X$, so

that

$$\frac{dy(t)}{dt} = \begin{pmatrix} L(t,x,u) \\ \\ f(t,x,u) \end{pmatrix} =: g(t,y,u), \quad \text{a.e. in } [0,T]. \tag{A.13}$$

The core of the argument in proving the maximum principle will follow results of Ekeland [Ekeland, 1979], and techniques developed in [Fattorini, 1987; Krastanov et al., 2011; Li and Yong, 2012]. We will now state a result known as Ekeland variational principle [Ekeland, 1979].

Lemma A.2.1. *(**Ekeland Variational Principle**) Let V be a complete metric space with respect to the distance function $d(\cdot,\cdot)$ and let $F : V \to \mathbb{R} \cup \{+\infty\}$ be lower semicontinuous and bounded below with $F \not\equiv +\infty$. Let $\epsilon > 0$ and $u \in V$ be such that*

$$F(u) \leq \inf\{F(w) \ : \ w \in V\} + \epsilon. \tag{A.14}$$

Then there exists $v \in V$ such that

$$d(u,v) \leq \sqrt{\epsilon} \tag{A.15}$$

$$F(w) - F(v) \geq -\sqrt{\epsilon}\, d(w,v), \quad \forall w \in V. \tag{A.16}$$

Let us proceed by assuming that an optimal control to the problem (P) exists and is denoted by u^* and let $y^* = (x^{0,*}, x^*)$ be the corresponding optimal trajectory. We write the minimum cost by η_0, i.e. $\eta_0 = J(u^*)$. Now, for given $\epsilon > 0$, we consider the function $J_\epsilon : \mathcal{U} \to \mathbb{R}$,

$$J_\epsilon(u) = \sqrt{(J(u) - \eta_0 + \epsilon)^2 + \|x(T) - x_T\|_X^2}. \tag{A.17}$$

It is evident that $J_\epsilon(u) > 0$ for all $u \in \mathcal{U}$ and $\epsilon > 0$. Moreover,

$$J_\epsilon(u^*) = \epsilon \leq \inf_{u \in \mathcal{U}} J_\epsilon(u) + \epsilon,$$

which by the Ekeland variational principle yields the existence of $u^\epsilon \in \mathcal{U}$ such that

$$d(u^\epsilon, u^*) \leq \sqrt{\epsilon}, \tag{A.18}$$

$$J_\epsilon(w) - J_\epsilon(u^\epsilon) \geq -\sqrt{\epsilon}\, d(w, u^\epsilon), \quad \forall w \in \mathcal{U}. \tag{A.19}$$

Next, we introduce a variation in control u^ϵ what is known as "needle variations". For any $v(\cdot) \in \mathcal{U}$, let $h : [0, T] \to \mathbb{R} \times X$,

$$h(t) = (g(t, x^\epsilon(t), v(t)) - g(t, x^\epsilon(t), u^\epsilon(t))) = \begin{pmatrix} L(t, x^\epsilon(t), v(t)) - L(t, x^\epsilon(t), u^\epsilon(t)) \\ f(t, x^\epsilon(t), v(t)) - f(t, x^\epsilon(t), u^\epsilon(t)) \end{pmatrix}. \tag{A.20}$$

Then, according to Corollary 3.9 (p. 144) of [Li and Yong, 2012] , for any $\rho \in (0, 1]$, there is a measurable set $F_\rho \subset [0, T]$ such that $\text{meas}\{F_\rho\} = \rho T$ and

$$\rho \int_0^t h(s)ds = \int_{F_\rho \cap [0,t]} h(s)ds + o(\rho), \tag{A.21}$$

where $\frac{o(\rho)}{\rho} \to 0$ as $\rho \downarrow 0$, uniformly in $t \in [0, T]$. The perturbed control is then defined as,

$$u^\epsilon_\rho(t) = \begin{cases} u^\epsilon(t), & t \notin F_\rho, \\ v(t), & t \in F_\rho \end{cases}. \tag{A.22}$$

It is of interest to express the perturbation in trajectory when the control u^ϵ_ρ is applied, i.e. we want a Taylor like expansion of $y^\epsilon_\rho(t) = y(t, u^\epsilon_\rho)$ with respect to ρ

at $\rho = 0$, i.e. at $y^\epsilon(t) = y(t, u^\epsilon)$. Let us write,

$$y^\epsilon_\rho(t) = y^\epsilon(t) + \rho\psi^\epsilon(t) + o(\rho).$$

Then,

$$\begin{aligned}
\psi^\epsilon(t) &= \lim_{\rho\downarrow 0} \frac{y^\epsilon_\rho(t) - y^\epsilon(t)}{\rho} \\
&= \lim_{\rho\downarrow 0} \frac{1}{\rho}\left(\int_0^t g(s, y^\epsilon_\rho(s), u^\epsilon_\rho(s))ds - \int_0^t g(s, y^\epsilon(s), u^\epsilon(s))ds\right) \\
&= \lim_{\rho\downarrow 0} \int_0^t \frac{g(s, y^\epsilon_\rho(s), u^\epsilon_\rho(s)) - g(s, y^\epsilon, u^\epsilon_\rho(s))}{\rho} ds \\
&\quad + \lim_{\rho\downarrow 0} \int_{[0,t]\cap F_\rho} \frac{g(s, y^\epsilon(s), v(s)) - g(s, y^\epsilon, u^\epsilon(s))}{\rho} ds \\
&= \int_0^t g'_y(s, y^\epsilon(s), u^\epsilon(s)) \cdot \psi^\epsilon(s) ds + \int_0^t \left(g(s, y^\epsilon(s), v(s)) - g(s, y^\epsilon, u^\epsilon(s))\right) ds,
\end{aligned} \tag{A.23}$$

where the second term follows from (A.21). g'_y is the Fréchet derivative of g with respect to y and can be decomposed as,

$$g'_y(t, y^\epsilon(t), u^\epsilon(t)) \cdot \bar{q} = \begin{pmatrix} L'_x(t, x^\epsilon(t), u^\epsilon(t)) \cdot q \\ \\ f'_x(t, x^\epsilon(t), u^\epsilon(t)) \cdot q \end{pmatrix}, \quad \text{for any } \bar{q} = (q_0, q) \in \mathbb{R} \times X.$$

Let's write $\psi^\epsilon(t) = (z^\epsilon_0(t), z^\epsilon(t))$. In particular, we have $z^\epsilon_0(T) = \frac{d}{d\rho} J(u^\epsilon_\rho)\big|_{\rho=0}$ and $z^\epsilon(t) = \frac{d}{d\rho} x^\epsilon_\rho(t))\big|_{\rho=0}$, each of which can be spelled out separately from (A.23),

$$z^\epsilon_0(T) = \int_0^T L'_x(s, x^\epsilon(s), u^\epsilon(s)) \cdot z^\epsilon(s) ds + \int_0^T \left(L(s, x^\epsilon(s), v(s)) - L(s, x^\epsilon(s), u^\epsilon(s))\right) ds, \tag{A.24}$$

$$z^\epsilon(t) = \int_0^t f'_x(s, x^\epsilon(s), u^\epsilon(s)) \cdot z^\epsilon(s) ds + \int_0^t \left(f(s, x^\epsilon(s), v(s)) - f(s, x^\epsilon(s), u^\epsilon(s))\right) ds. \tag{A.25}$$

Now, as a next step, we derive necessary conditions for the pair $(y^\epsilon(t), u^\epsilon(t))$ to be suboptimal. We do this by using the Ekeland variational principle and letting ρ tend to zero. In (A.19), we set $w = u^\epsilon_\rho$. Note that the controls u^ϵ and u^ϵ_ρ differ only in the set F_ρ, which has a measure ρT. Then,

$$\begin{aligned} J_\epsilon(u^\epsilon_\rho) - J_\epsilon(u^\epsilon) &\geq -\sqrt{\epsilon} d(u^\epsilon_\rho, u^\epsilon) \\ &\geq -\sqrt{\epsilon}\rho T. \end{aligned}$$

i.e.

$$\frac{J_\epsilon(u^\epsilon_\rho) - J_\epsilon(u^\epsilon)}{\rho} \geq -T\sqrt{\epsilon}. \tag{A.26}$$

Now, note that,

$$\begin{aligned} \lim_{\rho \downarrow 0} \frac{J_\epsilon(u^\epsilon_\rho) - J_\epsilon(u^\epsilon)}{\rho} &= \left.\frac{dJ_\epsilon(u^\epsilon_\rho)}{d\rho}\right|_{\rho=0} \\ &= \frac{1}{2J_\epsilon(u^\epsilon_\rho)} \left[2(J(u^\epsilon_\rho) - \eta_0 + \epsilon) \frac{dJ(u^\epsilon_\rho)}{d\rho} \right. \\ &\quad \left. +2 \left\| x^\epsilon_\rho(T) - x_T \right\| \left(\left\| x^\epsilon_\rho(T) - x_T \right\| \cdot \frac{dx^\epsilon_\rho(T)}{d\rho} \right) \right] \Bigg|_{\rho=0} \\ &= \frac{(J(u^\epsilon) - \eta_0 + \epsilon)}{J_\epsilon(u^\epsilon)} z^\epsilon_0(T) + \left\langle \frac{x^\epsilon(T) - x_T}{J_\epsilon(u^\epsilon)}, z^\epsilon(T) \right\rangle. \end{aligned} \tag{A.27}$$

Thus, taking the limit in (A.26), we can write,

$$\xi^\epsilon_0 z^\epsilon_0(T) + \langle \xi^\epsilon, z^\epsilon(T) \rangle \geq -T\sqrt{\epsilon}, \tag{A.28}$$

where $\xi^\epsilon_0 = \frac{(J(u^\epsilon) - \eta_0 + \epsilon)}{J_\epsilon(u^\epsilon)}$ and $\xi^\epsilon = \frac{x^\epsilon(T) - x_T}{J_\epsilon(u^\epsilon)} \in X^*$. Note additionally that,

$$(\xi^\epsilon_0)^2 + \|\xi^\epsilon\|^2 = 1. \tag{A.29}$$

Equation (A.28) can be regarded as the necessary conditions for $(y^\epsilon(t), u^\epsilon(t))$. Finally, we will let ϵ tend to zero to obtain necessary conditions for $(y^*(t), u^*(t))$ to be optimal. Define,

$$z_0 := \int_0^T L'_x(s, x^*(s), u^*(s)) \cdot z(s) ds + \int_0^T \left(L(s, x^*(s), v(s)) - L(s, x^*(s), u^*(s))\right) ds, \tag{A.30}$$

$$z(t) := \int_0^t f'_x(s, x^*(s), u^*(s)) \cdot z(s) ds + \int_0^t \left(f(s, x^*(s), v(s)) - f(s, x^*(s), u^*(s))\right) ds. \tag{A.31}$$

Since $v(\cdot)$ is any arbitrary element in $\mathcal{U}$, $z(T) \in \mathcal{R}$, c.f. (A.7).

Lemma A.2.2. *The following results hold true.*

$$\begin{aligned} \lim_{\epsilon \downarrow 0} |z_0^\epsilon(T) - z_0| &= 0, \\ \lim_{\epsilon \downarrow 0} \sup_{t \in [0,T]} \|z^\epsilon(t) - z(t)\| &= 0, \end{aligned} \tag{A.32}$$

Proof. Let us denote $S_\epsilon = \{t \in [0,T] : u^\epsilon(t) \neq u^*(t)\}$. Then, $\text{meas}\{S_\epsilon\} = d(u^\epsilon, u^*) \leq \sqrt{\epsilon}$, by (A.18). From the definition of $z(t)$, we find,

$$\|z(t)\| \leq M \int_0^t \|z(s)\| \, ds + 2MT,$$

where boundedness of both f and f'_x have been used. Applying the Gronwall-Bellman inequality, we get $\|z(t)\| \leq 2MTe^{MT}$, for all $t \in [0,T]$. We now write,

$$\begin{aligned} z^\epsilon(t) - z(t) = &\int_0^t f'_x(s, x^\epsilon(s), u^\epsilon(s)) \cdot (z^\epsilon(s) - z(s)) ds \\ &+ \int_0^t \left(f'_x(s, x^\epsilon(s), u^\epsilon(s)) - f'_x(s, x^*(s), u^*(s))\right) \cdot z(s) ds \\ &+ \int_0^t \left(f(s, x^\epsilon(s), v(s)) - f(s, x^*(s), v(s))\right) ds \\ &+ \int_0^t \left(f(s, x^\epsilon(s), u^\epsilon(s)) - f(s, x^*(s), u^*(s))\right) ds. \end{aligned}$$

Taking norm on both sides and utilizing boundedness of f'_x and $z(t)$, we obtain,

$$\begin{aligned}\|z^\epsilon(t) - z(t)\| \leq M \int_0^t \|z^\epsilon(s) - z(s)\|\, ds \\ + 2MTe^{MT} \int_0^t \|f'_x(s, x^\epsilon(s), u^\epsilon(s)) - f'_x(s, x^*(s), u^*(s))\|\, ds \\ + \int_0^t \|f(s, x^\epsilon(s), v(s)) - f(s, x^*(s), v(s))\|\, ds \\ + \int_0^t \|f(s, x^\epsilon(s), u^\epsilon(s)) - f(s, x^*(s), u^*(s))\|\, ds. \qquad \text{(A.33)}\end{aligned}$$

The last term in (A.33) can be written as,

$$\begin{aligned}&\int_0^t \|f(s, x^\epsilon(s), u^\epsilon(s)) - f(s, x^*(s), u^*(s))\|\, ds \\ &= \int\limits_{[0,t]\setminus S_\epsilon} \|f(s, x^\epsilon(s), u^*(s)) - f(s, x^*(s), u^*(s))\|\, ds \\ &\quad + \int\limits_{[0,t]\cap S_\epsilon} \|f(s, x^\epsilon(s), u^\epsilon(s)) - f(s, x^*(s), u^*(s))\|\, ds \\ &\leq K \int\limits_{[0,t]\setminus S_\epsilon} \|x^\epsilon(s) - x^*(s)\|\, ds + 2Md(u^\epsilon, u^*) \\ &\leq (KC_1T + 2M)d(u^\epsilon, u^*) \leq (KC_1T + 2M)\sqrt{\epsilon} \xrightarrow{\epsilon\downarrow 0} 0.\end{aligned}$$

Note that we have used the Lipschitz property of f and result of Lemma A.1.1. The second and third term can be treated in a similar fashion to show they are of $o(1)$ which goes to 0 as ϵ tends to 0. Note that, instead of Lipschitz continuity, we would use continuity of f'_x in x in order to use appropriate upper bound. Hence, (A.33) can be written as,

$$\|z^\epsilon(t) - z(t)\| \leq M \int_0^t \|z^\epsilon(s) - z(s)\|\, ds + o(1),$$

which by Gronwall-Bellman inequality yields,

$$\|z^\epsilon(t) - z(t)\| \leq e^{MT} o(1) \xrightarrow{\epsilon \downarrow 0} 0,$$

uniformly in $t \in [0, T]$. The convergence of $z_0^\epsilon(T)$ can be shown analogously. ■

Using (A.28) and the Cauchy-Schwarz inequality, we may now write,

$$\begin{aligned}
\xi_0^\epsilon z_0 + \langle \xi^\epsilon, z(T) \rangle &= \xi_0^\epsilon z_0^\epsilon + \langle \xi^\epsilon, z^\epsilon(T) \rangle - \xi_0^\epsilon (z_0^\epsilon - z_0) - \langle \xi^\epsilon, z^\epsilon(T) - z(T) \rangle \\
&\geq -T\sqrt{\epsilon} - |\xi_0^\epsilon| \, |z_0^\epsilon - z_0| - \|\xi^\epsilon\| \, \|z^\epsilon(T) - z(T)\| \\
&\geq -T\sqrt{\epsilon} - |z_0^\epsilon - z_0| - \|z^\epsilon(T) - z(T)\| . \qquad \text{(A.34)}
\end{aligned}$$

The last inequality follows, since $(\xi_0^\epsilon)^2 + \|\xi^\epsilon\|^2 = 1$, both $|\xi_0^\epsilon| \leq 1$ and $\|\xi^\epsilon\| \leq 1$. Denote, $\kappa^\epsilon = -T\sqrt{\epsilon} - |z_0^\epsilon - z_0| - \|z^\epsilon(T) - z(T)\|$ and by the convergence results (A.32), we see that $\kappa^\epsilon \to 0$ as $\epsilon \downarrow 0$. Thus, (A.34) can be expressed as,

$$\xi_0^\epsilon z_0 + \langle \xi^\epsilon, z \rangle \geq -\kappa^\epsilon, \quad \forall z_0 \in \mathbb{R}, z \in \mathsf{R}, \qquad \text{(A.35)}$$

where, $\kappa^\epsilon \xrightarrow{\epsilon \downarrow 0} 0$. Now the assumption (A1) that the set R is finite codimensional in X is going to be useful in proving nontriviality of the limit of the pair $(\xi_0^\epsilon, \xi^\epsilon)$ as ϵ goes to 0. Here we state the following lemma from [Fattorini, 1987], as a consequence of finite codimensionality.

Lemma A.2.3. *Let Q be a set of finite codimension in a Hilbert space Z and let $\{z_n\}$ be a sequence of vectors in Z such that*

$$0 < c \leq \|z_n\| \leq C.$$

Assume additionally that,

$$\langle z_n, q\rangle \geq -\theta_n,$$

for $q \in Q$ *and* $\theta_n \to 0$ *as* $n \to \infty$. *Then there exists a subsequence of* $\{z_n\}$ *that converges weakly to* $z \in Z$, *and* $z \neq 0$.

Now choose a sequence $\{\epsilon(n)\}$ such that $\epsilon(n) \to 0$ as $n \to \infty$. Since both sequences $\{\xi_0^{\epsilon(n)}\}$ and $\{\xi^{\epsilon(n)}\}$ are bounded, there exist subsequences $\{\xi^{\epsilon(n_k)}\}$ and $\{\xi^{\epsilon(n_k)}\}$ that converge weakly to some $\bar{\xi}_0 \in \mathbb{R}$ and $\bar{\xi} \in X^*$. For simplicity, let the subsequences be denoted by themselves. Showing nontriviality of the pair $(\bar{\xi}_0, \bar{\xi})$ is a crucial step in proving maximum principle in infinite dimensional case. Recall that, $\xi_0^\epsilon = \frac{(J(u^\epsilon)-\eta_0+\epsilon)}{J_\epsilon(u^\epsilon)}$, so that $\xi_0^\epsilon > 0, \forall \epsilon > 0$. Hence, we may only have $\bar{\xi}_0 \geq 0$. If $\bar{\xi}_0 \neq 0$, we are done proving that $(\bar{\xi}_0, \bar{\xi}) \neq (0,0)$. Otherwise, let $\xi_0^\epsilon(n) \to 0$ as $n \to \infty$. Then from the relation (A.29), we get, $1 \geq \left\|\xi^{\epsilon(n)}\right\|^2 = 1 - \left(\xi_0^{\epsilon(n)}\right)^2 \geq 1 - \delta > 0$, for some $\delta > 0$, for n large enough. Finally, by the lemma A.2.3, we get $\bar{\xi} \neq 0$ in the case $\bar{\xi}_0 = 0$. Hence we conclude that,

$$(\xi_0^\epsilon, \xi^\epsilon) \overset{*}{\rightharpoonup} (\bar{\xi}_0, \bar{\xi}) \neq (0,0), \quad \bar{\xi}_0 \geq 0. \tag{A.36}$$

Then, finally taking the limit $\epsilon \downarrow 0$ in (A.35), we get for any $z \in \mathsf{R}$ and z_0 as specified in (A.30), there exists a pair $\mathbb{R} \times X^* \ni (\bar{\xi}_0, \bar{\xi}) \neq (0,0)$, $\bar{\xi}_0 \geq 0$, so that,

$$\bar{\xi}_0 z_0 + \left\langle \bar{\xi}, z \right\rangle \geq 0. \tag{A.37}$$

Now, let us introduce the costate variable $p^*(t) \in X^*$, that obeys the following differential equation,

$$\dot{p}^*(t) = -\left(f_x'(t, x^*(t), u^*(t))^\star p^*(t) - p_0^* L_x'(t, x^*(t), u^*(t)\right), \tag{A.38}$$

with $p^*(T) = -\bar{\xi}$ and $p_0^* = -\bar{\xi}_0 \leq 0$. Here by $\mathcal{A}^\star$ we denote the adjoint operator of the operator $\mathcal{A}$. Now since $z(0) = 0$, we have,

$$\begin{aligned}
&\langle p^*(T), z(T)\rangle \\
&= \langle p^*(T), z(T)\rangle - \langle p^*(0), z(0)\rangle \\
&= \int_0^T \frac{d}{dt}\langle p^*(t), z(t)\rangle \, dt \\
&= \int_0^T \big[\big\langle -\left(f_x'(t, x^*(t), u^*(t))^\star p^*(t) - p_0^* L_x'(t, x^*(t), u^*(t)\right), z(t)\big\rangle \\
&\qquad + \langle p^*(t), f_x'(t, x^*(t), u^*(t))z(t) + f(t, x^*(t), v(t)) - f(t, x^*(t), u^*(t))\rangle\big] \, dt \\
&= \int_0^T -p_0^* \langle L_x'(t, x^*(t), u^*(t)), z(t)\rangle \, dt \\
&\qquad + \int_0^T \left(\langle p^*(t), f(t, x^*(t), v(t)) - f(t, x^*(t), u^*(t))\rangle\right) dt
\end{aligned} \tag{A.39}$$

This, combined with the definition of z_0 (A.30) and equation (A.37) yields,

$$\begin{aligned}
&\langle p^*(T), z(T)\rangle + p_0^* z_0 \\
&= \int_0^T \left[H(t, x^*(t), v(t), p_0^*, p^*(t)) - H(t, x^*(t), u^*(t), p_0^*, p^*(t))\right] dt \leq 0.
\end{aligned} \tag{A.40}$$

Since the control set U is separable, the similar argument as in [Krastanov et al., 2011; Li and Yong, 2012] would give the pointwise maximization criterion of the pre-Hamiltonian,

$$H(t, x^*(t), v(t), p_0^*, p^*(t)) \leq H(t, x^*(t), u^*(t), p_0^*, p^*(t)), \text{ a.e. in } [0, T], \forall v \in \mathcal{U}. \tag{A.41}$$

From the definition of the Hamiltonian, we can finally compute its derivatives. In what follows, the appropriate arguments will be suppressed for simplicity and the notation $|_*$ will imply the function has been evaluated at optimal parameters. We

then find for any $(\tilde{x}, \tilde{p}) \in X \times X^*$,

$$\begin{aligned}
\left.\frac{\delta H}{\delta p^*}\right|_* \cdot \tilde{p} &= \left.\lim_{\sigma \to 0} \frac{H(p^* + \sigma\tilde{p}) - H(p^*)}{\sigma}\right|_* \\
&= \left.\frac{d}{d\sigma} H(p^* + \sigma\tilde{p})\right|_{\sigma=0,*} \\
&= \langle \tilde{p}, f|_* \rangle
\end{aligned}$$

and,

$$\begin{aligned}
\left.\frac{\delta H}{\delta x^*}\right|_* \cdot \tilde{x} &= \left.\lim_{\sigma \to 0} \frac{H(x^* + \sigma\tilde{x}) - H(x^*)}{\sigma}\right|_* \\
&= \left.\frac{d}{d\sigma} H(x^* + \sigma\tilde{x})\right|_{\sigma=0,*} \\
&= \left.\frac{d}{d\sigma} \left(\langle p^*, f(x^* + \sigma\tilde{x}) \rangle + p_0^* L(x^* + \sigma\tilde{x}) \right)\right|_{\sigma=0,*} \\
&= \langle p^*, f_x'|_* \cdot \tilde{x} \rangle + p_0^* \langle L_x'|_*, \tilde{x} \rangle \\
&= \left\langle (f_x'|_*)^\star \, p^* + p_0^* L_x'|_*, \tilde{x} \right\rangle .
\end{aligned}$$

Thus, we may write the canonical Hamilton's equations of motion,

$$\begin{aligned}
\frac{dx^*}{dt} &= \frac{\delta H}{\delta p^*}(t, x^*, u^*, p_0^*, p^*), \\
\frac{dp^*}{dt} &= -\frac{\delta H}{\delta x^*}(t, x^*, u^*, p_0^*, p^*).
\end{aligned} \tag{A.42}$$

This completes the proof of the maximum principle.

■

Bibliography

Agrachev, A. and Sachkov, Y. 2004. Control Theory from the Geometric Viewpoint. Springer, Berlin.

Attanasi, A., Cavagna, A., Del Castello, L., Giardina, I., Grigera, T. S., Jelić, A., Melillo, S., Parisi, L., Pohl, O., Shen, E., and Viale, M. 2014. Information transfer and behavioural inertia in starling flocks. *Nature physics* 10:691–696.

Austin, M. A., Krishnaprasad, P. S., and Wang, L.-S. 1993. Almost poisson integration of rigid body systems. *Journal of Computational Physics* 107:105–117.

Avez, A. 1986. Differential calculus. John Wiley & Sons Inc.

Ballerini, M., Cabibbo, N., Candelier, R., Cavagna, A., Cisbani, E., Giardina, I., Lecomte, V., Orlandi, A., Parisi, G., Procaccini, A., Viale, M., and Zdravkovic, V. 2008a. Interaction ruling animal collective behavior depends on topological rather than metric distance: Evidence from a field study. *Proceedings of the National Academy of Sciences* 105:1232–1237.

Ballerini, M., Cabibbo, N., Candelier, R., Cavagna, A., Cisbani, E., Giardina, I., Orlandi, A., Parisi, G., Procaccini, A., Viale, M., et al. 2008b. Empirical investigation of starling flocks: a benchmark study in collective animal behaviour. *Animal behaviour* 76:201–215.

Bellaïche, A., Jean, F., and Risler, J. J. 1998. Geometry of nonholonomic systems. *In* J.-P. Laumond (ed.), Robot Motion Planning and Control. Springer, London.

Bialek, W., Cavagna, A., Giardina, I., Mora, T., Silvestri, E., Viale, M., and Walczak, A. M. 2012. Statistical mechanics for natural flocks of birds. *Proceedings of the National Academy of Sciences* 109:4786–4791.

Birkhoff, G. D. 1915. The restricted problem of three bodies. *Rendiconti del Circolo Matematico di Palermo* 39:265–334.

Bishop, R. L. 1975. There is more than one way to frame a curve. *American Mathematical Monthly* pp. 246–251.

Bliss, G. A. 1946. Lectures on the calculus of variations, phoenix science series. *The University of Chicago Press, Chicago* 37:1–6.

Brockett, R. 1973. Lie theory and control systems defined on spheres. *SIAM Journal on Applied Mathematics* 25:213–225.

Byrd, P. F. and Friedman, M. D. 1971. Handbook of Elliptic Integrals for Engineers and Scientists. Springer Berlin Heidelberg.

Cavagna, A., Cimarelli, A., Giardina, I., Parisi, G., Santagati, R., Stefanini, F., and Viale, M. 2010. Scale-free correlations in starling flocks. *Proceedings of the National Academy of Sciences* 107:11865–11870.

Cavagna, A., Conti, D., Giardina, I., and Grigera, T. S. 2018. Propagating speed waves in flocks: a mathematical model. *Physical Review E* 98:052404.

Chiu, C., Reddy, P. V., Xian, W., Krishnaprasad, P. S., and Moss, C. F. 2010. Effects of competitive prey capture on flight behavior and sonar beam pattern in paired big brown bats, *Eptesicus Fuscus*. *Journal of Experimental Biology* 213:3348–3356.

Chorin, A. J., Marsden, J. E., and Marsden, J. E. 1990. A mathematical introduction to fluid mechanics, volume 3. Springer.

Corbet, P. S. 1999. Dragonflies: Behavior and Ecology of Odonata. Comstock Publishing Associates.

Cucker, F. and Smale, S. 2007. Emergent behavior in flocks. *IEEE Transactions on automatic control* 52:852–862.

Davis, H. T. 1962. Introduction to nonlinear differential and integral equations, volume 971.Dover Publication, Inc.

Dey, B. 2015. Reconstruction, Analysis and Synthesis of Collective Motion. PhD thesis, University of Maryland, College Park.

Dey, B. and Krishnaprasad, P. S. 2012. Trajectory smoothing as a linear optimal control problem. *In* Proceedings of Annual Allerton Conference on Communication, Control, and Computing, pp. 1490–1497, Urbana-Champaign, IL. IEEE.

Dey, B. and Krishnaprasad, P. S. 2014. Control-theoretic data smoothing. *In* Proceedings of 53rd IEEE Conference on Decision and Control, pp. 5064–5070. IEEE.

Dubins, L. E. 1957. On curves of minimal length with a constraint on average curvature, and with prescribed initial and terminal positions and tangents. *American Journal of Mathematics* 79:497–516.

Ebin, D. G. and Marsden, J. 1970. Groups of diffeomorphisms and the motion of an incompressible fluid. *Annals of Mathematics* pp. 102–163.

Eells Jr, J. 1966. A setting for global analysis. *Bulletin of the American Mathematical Society* 72:751–807.

Egorov, Y. V. 1963. The optimal control in banach space. *Dokl. Akad. Nauk SSSR* 150:241–244.

Ekeland, I. 1979. Nonconvex minimization problems. *Bulletin of the American Mathematical Society* 1:443–474.

Elsgolc, L. D. 2012. Calculus of variations. Courier Corporation.

Euler, L. 1744. Methodus inveniendi lineas curvas maximi minimive proprietate gaudentes sive solutio problematis isoperimetrici latissimo sensu accepti.

Fattorini, H. 1987. A unified theory of necessary conditions for nonlinear nonconvex control systems. *Applied Mathematics and Optimization* 15:141–185.

Fraichard, T. and Scheuer, A. 2004. From Reeds and Shepp's to continuous-curvature paths. *IEEE Transactions on Robotics* 20:1025–1035.

Galloway, K., Justh, E., and Krishnaprasad, P. 2009. Geometry of cyclic pursuit. *In* Proceedings of 48th IEEE Conference on Decision and Control, IEEE, pp. 3629–3643.

Galloway, K. S., Justh, E. W., and Krishnaprasad, P. S. 2013. Symmetry and reduction in collectives: cyclic pursuit strategies. *Proceedings of the Royal Society A* 469:20130264.

Gelfand, I. and Fomin, S. 1963. Calculus of variations. Revised English edition translated and edited by Richard A. Silverman. Prentice-Hall Inc., Englewood Cliffs, NJ.

Ghose, K., Horiuchi, T. K., Krishnaprasad, P. S., and Moss, C. F. 2006. Echolocating bats use a nearly time-optimal strategy to intercept prey. *PLoS Biology* 4:865–873.

Giaquinta, M. and Hildebrandt, S. 1996. Calculus of Variations: Calculus of Variation. I. Springer-Verlag.

Goldstein, H., Poole, C., and Safko, J. 2001. Classical mechanics.Addison-Wesley.

Halder, U. and Dey, B. 2015. Biomimetic algorithms for coordinated motion: theory and implementation. *In* Proceedings of International Conference on Robotics and Automation, pp. 5426–5432. IEEE.

Halder, U., Justh, E. W., and Krishnaprasad, P. S. 2019a. Continuum flocking and control. In preparation for submission.

Halder, U. and Kalabic, U. 2017. Time-optimal solution for a unicycle path on se2 with a penalty on curvature. *IFAC-PapersOnLine* 50:6320–6325.

Halder, U., Raju, V., Krishnaprasad, P. S., and et al. 2019b. Cognitive cost of flocking: A geometric and hamiltonian perspective. In preparation for submission.

Halder, U., Schlotfeldt, B., and Krishnaprasad, P. S. 2016. Steering for beacon pursuit under limited sensing. *In* Proceedings of 55th IEEE Conference on Decision and Control, pp. 3848–3855. IEEE.

Heintze, E. and Liu, X. 1999. Homogeneity of infinite dimensional isoparametric submanifolds. *Annals of mathematics* 149:149–181.

Inada, Y. and Kawachi, K. 2002. Order and flexibility in the motion of fish schools. *Journal of Theoretical Biology* 214:371 – 387.

Justh, E. W. and Krishnaprasad, P. S. 2003. Steering laws and continuum models for planar formations. *In* Proceedings of 42nd IEEE Conference on Decision and Control, pp. 3609–3615. IEEE.

Justh, E. W. and Krishnaprasad, P. S. 2004. Equilibria and steering laws for planar formations. *Systems & Control Letters* 52:25 – 38.

Justh, E. W. and Krishnaprasad, P. S. 2005. Natural frames and interacting particles in three dimensions. *In* Proceedings of 44th IEEE Conference on Decision and Control, pp. 2841–2846. IEEE.

Justh, E. W. and Krishnaprasad, P. S. 2006. Steering laws for motion camouflage. *Proceedings of Royal Society A* 462:3629–3643.

Justh, E. W. and Krishnaprasad, P. S. 2015a. Enlargement, geodesics, and collectives. *In* International Conference on Networked Geometric Science of Information, pp. 558–565. Springer.

Justh, E. W. and Krishnaprasad, P. S. 2015b. Optimality, reduction and collective motion. *Proceedings of Royal Society A* 471:20140606.

Justh, E. W. and Krishnaprasad, P. S. 2016. Subriemannian geodesics for coupled nonholonomic integrators. *In* Proceedings of American Control Conference, pp. 7281–7288. IEEE.

Kinect. Microsoft kinect. `http://www.xbox.com/en-US/xbox-one/accessories/kinect-for-xbox-one`. [Online].

Krastanov, M. I., Ribarska, N., and Tsachev, T. Y. 2011. A pontryagin maximum principle for infinite-dimensional problems. *SIAM Journal on Control and Optimization* 49:2155–2182.

Krishnaprasad, P., Marcus, S. I., and Hazewinkel, M. 1983. Current algebras and the identification problem. *Stochastics: An International Journal of Probability and Stochastic Processes* 11:65–101.

Krishnaprasad, P. S. 1993. Optimal control and Poisson reduction. Technical Report 93-87, Institute for Systems Research, University of Maryland.

Kudrolli, A., Lumay, G., Volfson, D., and Tsimring, L. S. 2008. Swarming and swirling in self-propelled polar granular rods. *Physical review letters* 100:058001.

LaValle, S. M. 2006. Planning Algorithms. Cambridge university press.

Li, X. and Yong, J. 2012. Optimal control theory for infinite dimensional systems. Springer Science & Business Media.

MATLAB. MATLAB Robotics Toolbox. `http://www.mathworks.com/products/robotics/`. [Online].

Mischiati, M. and Krishnaprasad, P. S. 2010. Motion camouflage for coverage. *In* Proceedings of American Control Conference, pp. 6429–6435. IEEE.

Mischiati, M. and Krishnaprasad, P. S. 2011. Mutual motion camouflage in 3D. *In* Proceedings of the 18th IFAC World Congress, pp. 4483–4488.

Mischiati, M. and Krishnaprasad, P. S. 2012. The dynamics of mutual motion camouflage. *Systems & Control Letters* 61:894–903.

Mischiati, M. and Krishnaprasad, P. S. 2017. Geometric decompositions of collective motion. *Proceedins of Royal Society A* 473:20160571.

Mizutani, A., Chahl, J. S., and Srinivasan, M. V. 2003. Insect behaviour: Motion camouflage in dragonflies. *Nature* 423:604–604.

Mora, T. and Bialek, W. 2011. Are biological systems poised at criticality? *Journal of Statistical Physics* 144:268–302.

Nagy, M., Akos, Z., Biro, D., and Vicsek, T. 2010. Hierarchical group dynamics in pigeon flocks. *Nature* 464:890–893.

Nghiem, A. T., Auvinet, E., and Meunier, J. 2012. Head detection using Kinect camera and its application to fall detection. *In* Proceedings of 11th International Conference on Information Science, Signal Processing and their Applications, pp. 164–169. IEEE.

Ohsawa, T. 2013. Symmetry reduction of optimal control systems and principal connections. *SIAM Journal on Control and Optimization* 51:96–120.

Olberg, R. M., Worthington, A. H., and Venator, K. R. 2000. Prey pursuit and interception in dragonflies. *Journal of Comparative Physiology A* 186:155–162.

Oliver, A., Kang, S., Wünsche, B. C., and MacDonald, B. 2012. Using the Kinect as a navigation sensor for mobile robotics. *In* Proceedings of the 27th Conference on Image and Vision Computing, pp. 509–514. ACM.

OpenCV. `http://opencv.org/`. [Online].

Pioneer. Pioneer P3-DX. `http://www.mobilerobots.com/researchrobots/pioneerp3dx.aspx`. [Online].

Pontryagin, L. S., Boltyanskiy, V. G., Gamkrelidze, R. V., and Mishchenko, E. F. 1962. Mathematical theory of optimal processes. Interscience.

Pressley, A. and Segal, G. B. 1986. Loop Groups. Clarendon Press.

Raju, V. and Krishnaprasad, P. S. 2018. A variational problem on the probability simplex. *In* Proceedings of 57th IEEE Conference on Decision and Control, pp. 3522–3528. IEEE.

Rashevsky, P. 1938. About connecting two points of a completely nonholonomic space by admissible curve. *Uch. Zapiski Ped. Inst. Libknechta* 2:83–94.

Reddy, P. V., Justh, E., and Krishnaprasad, P. S. 2006. Motion camouflage in three dimensions. *In* Proceedings of 45th IEEE Conference on Decision and Control, pp. 3327–3332. IEEE.

Reeds, J. and Shepp, L. 1990. Optimal paths for a car that goes both forwards and backwards. *Pacific Journal of Mathematics* 145:367–393.

ROS. Robot Operating System. `http://www.ros.org`. [Online].

ROS-ARIA. `http://wiki.ros.org/ROSARIA`. [Online].

Rund, H. 1966. The Hamilton-Jacobi theory in the calculus of variations: its role in mathematics and physics. Krieger Pub Co.

Salehani, M. K. and Markina, I. 2014. Controllability on infinite-dimensional manifolds: a chow–rashevsky theorem. *Acta Applicandae Mathematicae* 134:229–246.

Sussmann, H. J. and Tang, G. 1991. Shortest paths for the Reeds-Shepp car: A worked out example of the use of geometric techniques in nonlinear optimal control. Technical Report 91-10, Rutgers Center for Systems and Control.

Svirezhev, Y. M. 1972. Optimum principles in genetics. *Studies on theoretical genetics* pp. 86–102.

Thurrowgood, S., Moore, R. J., Soccol, D., Knight, M., and Srinivasan, M. V. 2014. A biologically inspired, vision-based guidance system for automatic landing of a fixed-wing aircraft. *Journal of Field Robotics* 31:699–727.

Topaz, C. M., Bertozzi, A. L., and Lewis, M. A. 2006. A nonlocal continuum model for biological aggregation. *Bulletin of mathematical biology* 68:1601.

Vásárhelyi, G., Virágh, C., Somorjai, G., Tarcai, N., Szörényi, T., Nepusz, T., and Vicsek, T. 2014. Outdoor flocking and formation flight with autonomous aerial robots. *In* Proceedings of IEEE/RSJ International Conference on Intelligent Robots and Systems, pp. 3866–3873. IEEE.

Vicon. Vicon motion capture system. `http://www.vicon.com`. [Online].

Vicsek, T., Czirók, A., Ben-Jacob, E., Cohen, I., and Shochet, O. 1995. Novel type of phase transition in a system of self-driven particles. *Physical Review Letters* 75:1226–1229.

Wei-Liang, C. 1939. Uber systeme von linearen partiellen differentialgleichungen erster ordnung. *Math. Ann* 117:98–105.

Young, G. F., Scardovi, L., Cavagna, A., Giardina, I., and Leonard, N. E. 2013. Starling flock networks manage uncertainty in consensus at low cost. *PLoS computational biology* 9:e1002894.

YouTube. Implementation videos. `http://ter.ps/ICRA2015`. [Online].

Zhang, H.-P., BeâĂŹer, A., Florin, E.-L., and Swinney, H. L. 2010. Collective motion and density fluctuations in bacterial colonies. *Proceedings of the National Academy of Sciences* 107:13626–13630.